Reconfigurable Phase-Change Metasurface Absorbers for Optoelectronic Device Applications

Submitted by

Santiago García-Cuevas Carrillo

to the

University of Exeter as a Thesis for the Degree of

Doctor of Philosophy in Engineering

in February 2019

I certify that all material in this thesis which is not my own work has been identified and that any material that has previously been submitted and approved for the award of a degree by this or any other University has been acknowledged.

Signature:…….

to my parents

List of Publications Resulting from this Thesis

- Santiago García-Cuevas Carrillo, Geoffrey R. Nash, Hasan Hayat, Maciej Klemm, Martin J. Cryan, Harish Bhaskaran and C. David Wright, "*Design of practicable phase-change metadevices for near-infrared absorber and modulator applications*", Optics Express, 24 **(12)**, 2016.
- Santiago García-Cuevas Carrillo, Arseny M. Alexeev Yat-Yin Au and C. David Wright, "*Reconfigurable phase-change meta-absorbers with on-demand quality factor control*", Optics Express, 26 **(20)**, 2018.
- Santiago García-Cuevas Carrillo, Liam Trimby, Yat-Yin Au, V. Karthik Nagareddy, Gerardo Rodriguez-Hernandez, Peiman Hosseini, Carlos Ríos, Harish Bhaskaran and C. David Wright, "*A Non-Volatile Phase-Change Metamaterial Color Display*", Advanced Optical Materials, pp. 1801782, 2019.
- Patent Application. *Title*: Display. *Application number*: GB1713586.4. *Lodged date*: 27 August 2017. *Applicant*: University of Exeter. *Inventors*: Santiago García-Cuevas Carrillo and C. David Wright. *Status*: Pending. Case details can be found at https://www.ipo.gov.uk/p-ipsum.
- Carlota Ruiz de Galarreta, Ivan Sinev, Arseny M. Alexeev, Pavel Trofimov, Konstantin Ladutenko, Santiago García-Cuevas Carrillo, Emanuele Gemo, Anna Baldycheva, V. Karthik Nagareddy, Jacopo Bertolotti and C. David Wright, "*All-Dielectric Silicon/Phase-Change Optical Metasurfaces with Independent and Reconfigurable Control of Resonant Modes*", https://arxiv.org/abs/1901.04955, submitted.

Conference Publications

- Glass Reflections, Glass in the Year of Light, University of Cambridge (United Kingdom), September 2015. Presentation title: "*Exploiting mixed-mode optical-electrical functionality in chalcogenide glasses*". Authors: C. David Wright, Santiago García-Cuevas Carrillo, Peiman Hoseini and Harish Bhaskaran. Presenter: Prof. C. David Wright.
- META'16, the 7th International Conference in Metamaterials, Photonic crystals and Plasmonics, Torremolinos (Spain), July 2016. Poster title: "*Non-Volatile Optoelectronic Phase-Change Meta-Displays*". Authors: Santiago García-Cuevas-Carrillo, Peiman Hosseini, Harish Bhaskaran and C. David Wright.
- European Phase-Change and Ovonic Symposium (E\PCOS) 2016, University of Cambridge (United Kingdom), September 2016. Presentation title: "*Phase-change meta-photonics*". Authors: C David Wright, Carlota Ruiz de Galarreta, Liam Trimby, Santiago García-Cuevas Carrillo, Jacopo Bertolotti, Daniel W Hewak, Martin Cryan, Macjek Klemm, Peimann Hosseini and Harish Bhaskaran. Presenter: Prof. C. David Wright.
- Materials Research Society (MRS) 2017, Phoenix (United States), April 2017. Presentation title: "*Tunable dielectric devices enabled by phase-change materials*". Authors: Arseny M. Alexeev, Carlota Ruiz de Galarreta, Santiago García-Cuevas Carrillo, Ivan S. Sinev, Anton K. Samusev, Emanuele Gemo, V. Karthik Nagareddy, Yat-Yin Au and C. David Wright. Presenter: Arseny M. Alexeev.
- European Phase-Change and Ovonic Symposium (E\PCOS) 2017, Aachen (Germany), September 2017. Poster title: "*Towards A Phase-Change Metamaterial CMY Subtractive Display*". Authors: Santiago García-Cuevas-Carrillo, Liam Trimby, Peiman Hosseini, Harish Bhaskaran and C. David Wright.
- European Phase-Change and Ovonic Symposium (E\PCOS) 2017, Aachen (Germany), September 2017. Presentation title: "*Tunable dielectric metadevices enabled by phase-change materials*". Authors: Arseny M. Alexeev, Carlota Ruiz de Galarreta, Santiago García-Cuevas Carrillo, Ivan S. Sinev, Anton K. Samusev, Emanuele Gemo, V. Karthik Nagareddy, Yat-Yin Au and C. David Wright. Presenter: Dr. Arseny M. Alexeev.

- European Phase-Change and Ovonic Symposium (E\PCOS) 2017, Aachen (Germany), September 2017. Poster title: "*Infrared Phase-Change Meta-Devices with In-Situ Switching*". Authors: Yat-Yin Au, Santiago García-Cuevas Carrillo, Carlota Ruiz de Galarreta and C. David Wright.
- EuroDisplay 2017, Berlin (Germany), October 2017. Poster title: "*Towards A Phase-Change Metamaterial CMY Subtractive Display*". Authors: Authors: Santiago García-Cuevas-Carrillo, Liam Trimby, Peiman Hosseini, Harish Bhaskaran and C. David Wright.
- Photonics and Optoelectronics Materials, University of Exeter (United Kingdom), April 2018. Poster title: "*Towards A Phase-Change Metamaterial CMY Subtractive Display*". Authors: Santiago García-Cuevas-Carrillo, Liam Trimby, Peiman Hosseini, Harish Bhaskaran and C. David Wright.

Events and Workshops

- Chalcogenide Advanced Manufacturing Partnership (ChAMP) meeting, University of Southampton (United Kingdom), March 2015.
- Wearable and Flexible Technologies (WAFT) meeting, University of Oxford (United Kingdom), November 2016. Poster title: "*Non-Volatile Optoelectronic Phase-Change Meta-Displays*". Authors: Santiago García-Cuevas-Carrillo, C. David Wright, Peiman Hosseini and Harish Bhaskaran.
- Industrial Application of Metamaterials - A UK Strategy, London, March 2017.
- Chalcogenide Advanced Manufacturing Partnership (ChAMP), University of Southampton (United Kingdom), September 2015. Presentation title: "*Near infrared phase-change metamaterial absorbers\amplitude modulators*". Authors: Santiago García-Cuevas Carrillo and C. David Wright.
- Wearable and Flexible Technologies (WAFT) meeting, University of Oxford (United Kingdom), November 2017. Poster title: "*Towards A Phase-Change Metamaterial CMY Subtractive Display*". Authors: Authors: Santiago García-Cuevas-Carrillo, Liam Trimby, Peiman Hosseini, Harish Bhaskaran and C. David Wright.
- Infrared Sensing and Imaging: Challenges for the next generation materials and devices, Exeter (United Kingdom), November 2017. Poster title: "*Phase-change meta-devices for near-infrared absorbers and modulators*". Authors: Santiago García-Cuevas Carrillo, Yat-Yin Au and C. David Wright.
- Joint UK Chalcogenide Workshop (ChAMP and WAFT project meeting), Lake District (United Kingdom), May 2018. Poster title: "*Towards A Phase-Change Metamaterial CMY Subtractive Display*". Authors: Santiago García-Cuevas-Carrillo, Liam Trimby, Peiman Hosseini, Harish Bhaskaran and C. David Wright.
- Wearable and Flexible Technologies (WAFT) meeting, Oxford (United Kingdom), February 2019.

Acknowledgements

I would like to acknowledge financial support from Engineering and Physical Sciences Research Council (EPSRC) of the United Kingdom and all people that contributes to its existence for the financial support during my studies. I thank also all people in the Centre for Doctoral Training in Metamaterials at University of Exeter for making possible this great experience.

My most sincere gratitude to my supervisor, Prof. C. David Wright, for depositing his confidence on me for this project. Thank you for your helpful advice, for your patience and the insight I gained during all these years of work. Thank you also to Prof. Geoffrey R. Nash for his help and support as second supervisor. I can say that I was truly fortunate having them as supervisors.

I would like to express also my gratitude to all members of the research group, to the ones that still are here and the ones that moved away, for all the discussions and help during the development of the thesis. I enjoyed a lot learning and working with all of you. Special thanks to Dr. Yat-Yin Au for his help with the optical and electro-optical measurements in Chapter 4 and Chapter 6, Dr. Hasan Hayat for the electrothermal and phase-change simulations in Section 4.3.2 and Dr. V. Karthik Nagareddy and Dr Arseny M. Alexeev for their help in the experimental and simulation work in this thesis. Thank you also to the IT technicians and the laboratory officers for their attention and dedicated work.

My deepest gratitude to the collaborators in the Department of Materials at University of Oxford and in the Metamaterials Laboratory at ITMO University (Saint Petersburg, Russia).

I thank also to all people at the university that could always find five minutes to discuss with a clueless student, especially to Dr. Ian Hooper, Dr. Mustafa Aziz and Prof. Euan Hendry.

Of course, I have to acknowledge the support of my friends here in Exeter. Having a drink with you helped to keep my head rational in the most stressful moments. I cannot name all of you, but at this moment I think you know who you are.

And last, and chiefly to my parents and sisters that have been always there backing me and giving me courage and strength in all ventures during my life.

Abstract

This thesis is concerned with the design and development of dynamically reconfigurable optical metasurfaces. This reconfigurability is achieved by integrating chalcogenide phase-change materials with plasmonic resonator structures of the metal-insulator-metal type. Switching the phase-change material between its amorphous and crystalline states results in dramatic changes in its optical properties, with consequent dramatic changes in the resonant behaviour of the plasmonic metasurface with which it is integrated. Moreover, such changes are non-volatile, reversible and potentially very fast, in the order of nanoseconds.

The first part of the thesis is dedicated to the design, fabrication and characterisation of metasurface devices working at telecommunications wavelengths, specifically at wavelengths corresponding to the C-band (1530 to 1565 nm), and that act as a form of perfect absorber when the phase-change layer (in this case $Ge_2Sb_2Te_5$) is amorphous but reflect strongly when switched to the crystalline state. Such behaviour can be used, for example, to provide a form of optical amplitude modulator. Fabricated devices not only showed very good performance, including a large modulation depth of ~77% and an extinction ratio of ~20 dB, but also incorporated a number of practicable design features often overlooked in the literature, including a means for protecting the phase-change layer from environmental oxidation and, importantly, an electrically-driven in-situ switching capability.

In the second part of the thesis a method, based on eigenmode analysis and critical coupling theory, is developed to allow for the design and fabrication of perfect absorber type devices in a simple and efficient way, while at the same time maintaining design control over the key performance characteristics of resonant frequency, reflection coefficient at resonance and quality factor. Validation of this new method was carried out via the design and fabrication of a family of absorbers with a range of ‘on-demand’ quality factors, all operating at the same resonant frequency and able to be fabricated simply and simultaneously on the same chip.

The final part of the thesis is concerned with the design and development of a switchable phase-change metamaterial type absorber working in the visible part of the spectrum and with non-volatile colour generating capability. With the phase-change layer, here GeTe, in the crystalline phase, the absorber can be tuned to selectively absorb the red, green and blue spectral bands, so generating vivid cyan, magenta and yellow pixels. When the phase-change layer is switched into the amorphous phase, the resonant absorption is suppressed and a flat, pseudo-white reflectance results. This potentially opens up a route to the development of non-volatile, phase-change metamaterial colour displays and colour electronic signage.

Contents

List of Figures

List of Tables

Chapter 1 Introduction

The ability to design devices capable of controlling the propagative characteristics of light at technologically important parts of the electromagnetic spectrum is essential to a number of important fields, such as telecommunications, sensing, imaging, spectroscopy, security and bio-sensing. Doing that in a reconfigurable fashion is of paramount importance, given that it allows the adaption of the response of the device according to the requirements of the application it is designed for.

Metamaterials – i.e. artificial 'materials' whose properties rely on the collective response of their engineered constitutive elements called meta-atoms – have raised a lot of interest among scientists and engineers from the beginning of the 20th century (and before) due to the unprecedented properties that these artificial structures possess to manipulate wave phenomena [1]. However, these properties are fixed by design and, although this can be enough in some areas, the full potential of metamaterial-based devices will only be harnessed when their response can be reconfigured. There exist several paths to achieve this purpose, one of the more popular ones due to the potential advantages that it would imply (one of the most important being non-volatile operation) is the combination of metamaterial concepts with chalcogenide phase-change materials.

This thesis is thus dedicated to the exploration and the study of the technological possibilities that metamaterial electromagnetic absorbers have in combination with phase-change materials. More specifically, devices for amplitude modulation in reflection will be considered with operation in the near-infrared and visible part of the electromagnetic spectrum. This study has also an engineering emphasis and the focus of it will be the search of new functionalities, design methods, compatible materials and fabrication and characterization of devices. Nevertheless, a significant part of the discussion will be concerned with the concepts behind the operation of the designed devices.

In this first chapter, a review of the most important historical milestones in phase-change material technology and metamaterial science are given. This will provide a general context before introducing the more specific and related theoretical background in Chapter 2. Moreover, reconfigurable metamaterials are also reviewed in general terms, and the concept of chalcogenide phase-change based metamaterial is presented along with other approaches to create metamaterial tuneable devices. Finally, at the end of this chapter, the objectives of the thesis are enunciated.

1.1. Historical background: phase-change materials and metamaterials

Chalcogenide phase-change materials undergo a reversible change in their structure from amorphous to a more energetically favourable crystalline phase, presenting an extraordinary contrast in their optical and electrical properties [2]. This change is very fast (on the order of nanoseconds) and driven by temperature. Such properties have made phase-change materials good candidates to be used in storage technology. Nowadays, it is possible to say that phase-change storage technology is a mature field.

To be considered a phase-change material there are some essential properties that a material must satisfy [3]:

- Fast phase transition optically or electrically induced.
- Thermal stability of the amorphous phase at room temperature, on the order of decades.
- Large refractive index and conductivity contrast between phases.
- Large number of cycles between amorphous and crystalline phases.

It is commonly accepted that the first person to propose phase-change materials for memory applications was Stanford R. Ovshinsky in 1968 [4]. However, some of the properties that characterise phase-change materials, in particular permanent resistance change, have been observed and reported since the beginning of the twentieth century in materials like MoS_2 (from high to low resistance) or later in 1962 in As-Te-Br or -I ternary glasses (reversible resistance change reported) [2]. As well as this, the first patents appeared in the 1960s (before published results in 1962), describing reversible resistance

switching phenomena in ternary semiconductor glasses (As-Te-I) and their application in electronic technology as a memory [5]. All this before the revolutionary work of Ovshinsky, who is often considered as the 'father' of phase-change materials [2,4].

In the 1970s, phase-change storage technology captured a lot of attention and made great progress [6,7]. However, the energy required to switch the memory cell at that time was very high compared to other technologies. This was due to the large amount of phase-change material that the memory cell contained (memory cell areas at that point were ~3×10^9 nm^2 [6] compared to the ~130 nm^2 [8] cells that can be fabricated today). From the late 1970s to the 1990s little progress was realised mainly due to this reason.

A twist of the events occurred with the advances in photolithography and the reduction of minimum feature size in semiconductor industry, predicted by Gordon Moore [9]. The attention was renewed in phase-change technology. A dramatic reduction of the consumed power was projected due to the excellent scalability properties that phase-change technology possesses. Another factor that boosted the development of this technology is military and aerospace investment since phase-change memories are very robust against radiation [10]. Te-based eutectic alloys were the first materials employed in phase-change technology such as $Te_{85}Ge_{15}$ doped with Sb, S and P [4]. The transition to the crystalline state in these materials was relatively slow at this point (in the order of microseconds). The first alloys that manifested fast crystallisation speeds as well as good electro-optical contrast were GeTe [11] and $Ge_{11}Te_{60}Sn_4Au_{25}$ [12]. After this, the pseudo–binary alloys along the GeTe-Sb_2Te_3 tie line were found [13], to which the archetypal phase-change material $Ge_2Sb_2Te_5$ belongs. A separate group of doped Sb_2Te compounds was discovered later, to which the well-known material $Ag_5In_5Sb_{60}Te_{30}$ (AIST, used in rewritable DVDs) belongs [3,14].

In the 1990s, phase-change optical disk memories became a reality and were massively commercialised. As well as this, companies like Panasonic, Ovonyx, BAE Systems, Intel, STMicroelectronics, Samsung, Hitachi, IBM, and many more helped in the development of optical and electronic phase-change memory through fundamental research and commercialisation of products [2,3].

The present and future landscape in phase-change material technology is defined by the latest commercialised products and the new applications for which phase-change

materials have been proposed. Two of the latest more relevant events in phase-change memory technology is the commercialisation of the memory 3D XPoint by Intel and Micron [15] and the presentation of reliable operation of a triple-level-cell developed by IBM Zurich [16], which forecast a very promising future for phase-change memory. As well as this, the potential of phase-change technology to overcome the so called Von-Neumann bottleneck[1] and their use as memristors[2] that operate as integrate-and-fire neurons [17] and synapses [18] in neuromorphic computing (spiking neural networks). Furthermore, the application of phase-change materials is not anymore solely restricted to conventional electrical and optical storage technology. Novel devices in the field of integrated photonics such as multilevel photonic memories [19–21] and photonic synapses for neuromorphic photonic circuits [22] are now gaining great attention. Finally, and very important for the work carried out in this thesis, is the use of phase-change materials for the provision of non-volatile reflective displays [23–25].

Turning now the attention to metamaterials, it is not easy to have a concise definition about the concept according to some authors [26]. This is due to the fact that the field has been constantly evolving and now extending beyond the realm of electromagnetism [27]. For instance, a very broad definition could be 'engineered material platforms for novel wave phenomena' [28]. Another definition slightly more specific is 'an arrangement of artificial structural elements designed to achieve advantageous and unusual electromagnetic properties' [29].

Metamaterials are in general composed of an arrangement of resonant elements (meta-atoms) separated by a distance smaller than the wavelength of the wave that is interacting with them. In electromagnetic applications, it is possible to engineer the electric and/or magnetic polarizabilities of the individual meta-atoms and, in this way, design the effective electric and magnetic permittivity of the metamaterial, so achieving effects of great technological importance or not present in nature (such as anomalous reflection [30] or perfect lensing [31]). If the meta-atoms are arranged in a surface instead of a volume, the name metasurface is usually used instead of metamaterial [32,33].

[1] The limitation in the performance of a computer with the Von-Neumann architecture arises from the fact that the operation of this architecture is based in the communication of a central processing unit and a separate memory [145].
[2] Device in which the value of the resistance is variable and dependent of the history of the current that has flown through it [197].

Interestingly, there are records from the 19th century in which scientists tried to control the propagation of light using devices that, in some cases, could have been explained from the metamaterial framework. This is the case for the work of Bose, for example, who tried changing the plane of polarisation of light passing through twisted jute structures [34]. In the case of metasurfaces, Lamb carried out the study of the properties of metal gratings when the distance between the elements of the array was subwavelength [35]. Both works, Bose's and Lamb's, were published in 1898 [36].

One of the most important early works related with metamaterial science (perhaps the most important one) is the paper that Victor Veselago published in 1969 [37], describing the propagation of light in a medium where the electric permittivity ε and the magnetic permeability μ were negative numbers (which does not occur in nature).

Artificial magnetic materials, which can be considered as metamaterials, also appeared in the middle of the 20th century [36,38]. As well as this, the 1980s saw the development of microwave absorbing materials that used chirality to transform the propagation characteristics of waves inside the material so that all radiation is absorbed by impedance matching [39] (a very important concept in this thesis). Chiral and bi-anisotropic media had a lot of attention in the 1990s [36]. Special mention should also be given to frequency selective surfaces, devices that served as an inspiration for many type of metasurfaces later on [40,41].

One leading event in the history of metamaterials occurred in the year 2000 when the paper published by John B. Pendry called "*Negative Refraction Makes a Perfect Lens*" [31] was published. In this work, the use of artificial materials with simultaneous negative values for the electric permittivity and the magnetic permeability for the provision of perfect lenses were proposed, and experimental proofs soon followed [42,43]. The work of Veselago now had an experimental framework that allowed it to be tested, and the word metamaterial began to be widely used. Numerous papers have since been published having metamaterial as the subject of interest, one of the most notable being the first demonstration of a cloak at microwave frequencies [44].

Before concluding this section, it is necessary to clarify that the focus of this discussion has primarily been the so-called plasmonic metamaterials [45]. However, other

approaches exist in the literature such as all-dielectric metamaterials and metasurfaces [46].

1.2. Reconfigurable metadevices

One of the current priorities in metamaterial research is finding an efficient way to transform conventional metamaterials into tunable or reconfigurable devices to serve a specific purpose. Among the areas[3] in which it would be interesting to have metamaterial devices it is possible to find telecommunication technology, spectroscopy, metrology, light detection, imaging and solar energy harvesting. Functionalities such as beam steering (e.g. for optical interconnects and LIDAR applications), wavelength selective absorption of light (e.g. for spectroscopy or detection), lensing (for imaging systems) or amplitude modulation (e.g. for telecommunications) are desired to become adaptable to the conditions in which the device is meant to be operated. To do this, many authors have proposed different routes to tune the response of metamaterials [47,48].

It is possible to find strategies based on the change of the optical response by modification of the geometry of the metasurface (relative position of the meta-atoms to each other or constitute the meta-atom itself) using micro-electro-mechanical systems (MEMS) [49], electrostatic forces [50], substrate stretching [51] or by thermal activation [52].

There is another set of strategies based in the modification of the refractive index of part of the materials that constitute the metamaterial. The response of an electromagnetic metamaterial has its origin in a resonance of electromagnetic foundation. If the optical constants of any of the material that form the metamaterials are modified, the resonant condition will change and thus change the response of the metamaterial. There are different materials that can experience a change in the refractive index and can be integrated in conjunction with metamaterials. Some materials base their refractive index change on modification of the carrier density of the active material [53,54]. In others however, the change in the optical constants of the active material is caused by a change in the material phase, like in the case of liquid crystals [55], vanadium dioxide [56], or,

[3] Excluding from this discussion RF and microwave metamaterials where different methods for tuning are used.

the central topic of this thesis, chalcogenide phase-change materials [57–62]. The main advantage of chalcogenide phase-change materials is their non-volatility and their fast (switching) operation. These properties, combined with metamaterial/metasurface concepts, have already been proposed to be exploited in a variety of fields such as thermal imaging [58] and optical telecommunications [57,59,60].

Of special interest to the work in this thesis is a type of metasurface called metal-insulator-metal electromagnetic absorber structures. These kinds of metasurfaces allow the absorption of the incident light when they are at resonance. When they are combined with a material that changes its refractive index, the resonance behaviour of the absorber metasurface changes and hence its response. The change in the response of phase-change metasurface absorbers results mainly in a displacement in frequency of the resonant peak, an attenuation of the response, or both. In that way it is possible to control the value of the reflected (absorbed) amount of light at a fixed frequency of operation. This will depend on the value of the optical constants for amorphous and crystalline states of the phase-change material, at the working wavelengths and the materials and geometry of the rest of the structure. Such phase-change 'metadevices' would be of non-volatile nature and could be switched optically or electrically, very fast. The durability of the devices will be determined by how many times the phase-change material can be switched, between amorphous and crystalline states. The potential number of cycles is rather high; there are authors that have reported the ability to undergo 10^{15} cycles in phase-change memories [63]. These characteristics provide insightful information on how the designed devices will fit in various technologically important photonics applications.

1.3. Objectives of the thesis

The main objective of this study is to unravel the potential of phase-change metasurface absorber structures for the generation of a platform for light absorption and amplitude modulation in the near infrared and visible part of the electromagnetic spectrum.

In particular, the following research challenges are addressed:

- The development of computational tools and techniques that allow for the proper design and simulation of the performance of reconfigurable phase-change

metasurfaces, in particular those based on the metal-insulator-metal resonant absorber configuration.

- The experimental realisation of promising device designs, paying particular attention to practical considerations such as protection of any phase-change layers from environmental oxidation, the suitability of designs to conventional fabrication techniques and manufacturing tolerances, and the ability to incorporate some form of electrically-driven in-situ switching (of the phase-change layer).
- The development of devices suited to operate in both the infrared and visible parts of the spectrum, for optical communications and optoelectronic display applications respectively.

1.4. Thesis Outline

Chapter 1: In the first chapter, the context of the thesis is given from a broad perspective. The two main topics studied in this thesis, namely phase-change materials and metamaterials, are introduced and reviewed from an historical perspective. The chapter finishes by giving a general overview on reconfigurable metadevices and enunciating the objectives of the thesis.

Chapter 2: The concepts and ideas explained in Chapter 2 serve as background to understand the results extracted in the thesis. These are selected topics from phase-change material and metamaterial science and technology, from where the developed ideas in the subsequent chapters are built upon. The discussion starts by explaining the phase-change process and the optical and electronic properties of phase-change materials. Then, the properties and principle of operation of metal-insulator-metal metamaterial absorber structures are explained and how the integration with phase-change materials has been carried out in the literature. Finally, plasmonic metasurfaces for colour generation and phase-change display technology are explained.

Chapter 3: The third chapter is dedicated to the computational and experimental techniques used in the thesis. The part concerning the computational techniques describes the different computational tools used and the mathematical formulation that corresponds to the different physical situations relevant to the thesis. The part dedicated to the

experimental techniques describes all fabrication and characterisation methods used in the development of the conceived devices in the different chapters.

Chapter 4: In the fourth chapter, the first preliminary study of a phase-change metasurface absorber/modulator operating at near-infrared frequencies is carried out. In this first study, various aspects of interest related to the performance of the designed device are evaluated. These aspects are quite diverse and not only are restricted to the operation of the devices as amplitude modulators. Topics such as fabrication tolerances and (light) incidence angle sensitivity as well as materials selection and polarisation effects are discussed. At the end of this chapter, the first experiments related with the validation of the experimental models and the switching of the devices by optical means (ex-situ switching) are reported.

Chapter 5: The operation principle of the basic phase-change metal-insulator-metal absorber device is discussed in the fifth chapter. Specifically, the framework of critical coupling theory is used to develop a method capable of targeting the factors that most fundamentally describe the response of a metamaterial absorber, namely operative resonant frequency, bandwidth and minimum reflectance at resonance. The method also allows one to relate aspects of the performance to the geometry of the device, providing in that way much simpler design guidelines. Moreover, various devices operating at near-infrared wavelengths are fabricated and tested, in order to confirm what was anticipated by the calculated results.

Chapter 6: In the sixth chapter, the operation of the device by electrical means (in-situ switching) is investigated. Different arrangements and strategies referred to the device design are presented in the chapter in order to illustrate this technological challenge. This investigation is also carried out in the near-infrared part of the electromagnetic spectrum. Furthermore, fabricated devices are also tested in an optoelectronic probe station to assess their operability and robustness.

Chapter 7: In Chapter 7, the metasurface and phase-change display concepts are combined. The purpose of this chapter is to design a platform for colour generation based on the subtraction and/or modulation of frequency bands in the visible part of the electromagnetic spectrum. The concept is proven by generating three kind of pixels that changes from an uncoloured state to a coloured state (cyan, magenta and yellow) when

the phase-change layer is switched. Devices are also fabricated and characterised in order to evaluate the correctness of the predictions in the visible part of the electromagnetic spectrum and demonstrate reconfigurable, non-volatile colour generation.

Chapter 8: In this chapter, the conclusions of the thesis and suggestions for further related work are discussed.

Chapter 2 Background

Following the general introduction in the previous chapter, a more detailed explanation of the essential ideas in metamaterial and phase-change material science related to the results in this thesis are given in this chapter.

Firstly, the behaviour of phase-change materials is explained. Specifically, the phase-change process as well as device-scale phase-change models are discussed. To end the discussion concerning phase-change materials, their electronic and optical properties in the amorphous and crystalline phases are presented.

After this, the discussion will be focused on metal-insulator-metal metasurface structures working at visible and near infrared wavelengths. Special focus is given to the principle of operation of these metasurfaces and the different ways various authors have explained it. This part will end with a general overview of the combination of metal-insulator-metal electromagnetic absorbers with phase-change materials.

Finally, a discussion on the different approaches present in the literature to produce colours with metasurfaces is given, followed by a short review of reflective phase-change based display concepts.

2.1. Chalcogenide phase-change materials

2.1.1. The phase-change process

The non-volatile phase-change process in chalcogenides, from amorphous phase to crystalline phase and vice-versa, is driven by the temperature in the material.

In the case of the material changing from amorphous to crystalline phase, the temperature in the material needs to have a value within a certain interval if this change is desired to be observed within sensible timescales (typically hundreds of nanoseconds to hours, rather than years or days) [2,64–66]. The lower bound of this temperature interval can be considered to be the glass temperature T_g of the material, above which the viscosity

experiences a sudden change [67]. The upper bound of this crystallisation interval can be considered to be the melting temperature of the material T_m. The maximum crystallisation rate is located at an intermediate temperature between T_g and T_m. That does not mean that the material will not crystallise below T_g. At room temperature the material can remain amorphous for decades (depending on the phase change material composition) but will eventually crystallise [3]. This is why the material in the amorphous phase said to be in a metastable state (non-equilibrium solid). Crystallisation and melting temperatures are different for different compositions of phase-change materials, and even sample preparation methods and geometry (thin films) can have an influence on these temperatures [2]. See **Figure 2.1** for a schematic representation of the relationship between the different phases of interest (glass, crystal and liquid) and the temperature through a time-temperature-transformation diagram of a typical phase-change material.

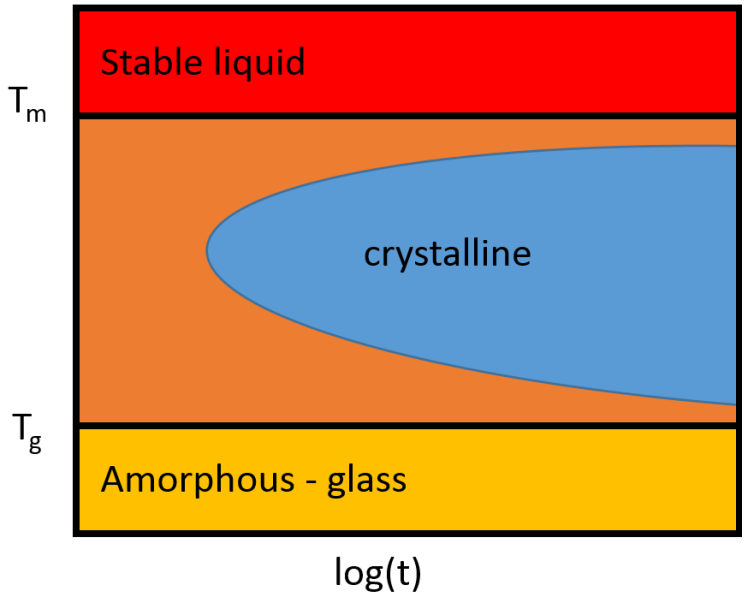

Figure 2.1. Time-temperature-transformation diagram for a phase-change material.

In the case of reamorphisation, the process consists of raising the temperature of the material above T_m and then cooling it very fast below T_g. This glass transition from molten state is a rather complicated process that has yet to be completely understood[4], as there are questions, such as making a quantitative and predictive picture of the behaviour of viscous liquids close to the glass transition temperature, that have yet to be resolved [68].

[4] "The deepest and most interesting unsolved problem in solid state theory is probably the theory of the nature of the glass transition; this could be the next breakthrough …." Anderson P.W. [198][2].

It is usually interpreted as an alternative path during cooling to avoid the entropy in the material being lower than that of the crystal state [2,68]. The cooling rates necessary to quench the material into the amorphous state depend on the composition, but they usually are approximately 10-100 K/ns [3,69]. See **Figure 2.2** for a schematic representation of the phase-change process.

In terms of speed, the amorphisation process is the fastest, since it only requires time to raise the temperature of the material above melting temperature and then to cool it very fast. The crystallisation process takes more time because the atoms need time to rearrange themselves into the crystalline phase. Indeed, improving crystallisation speeds has been one of the focuses of research in phase-change science and technology since the field's inception, due to the fact that the crystallisation process was the main obstacle for the fast operation of memory devices [3].

The endurance of phase-change based devices is often limited by two processes that are related to the phase-change material itself, namely material segregation and void formation (which lead to 'stuck closed' and 'stuck open' failure modes in phase-change memory terminology) [66]. The material segregation process is characterised by a change in stoichiometry (e.g. Sb enrichment) in parts of the volume of phase-change material. As a consequence, there will be a change of the material properties (such as change in crystallisation temperature) and subsequent deviation of the device performance from the designed behaviour. On the other hand, the formation of voids in the material is caused by a change in density when the material is switched between phases. Specifically, there is an increase in density when the material crystallises of 6% to 9% approximately (depending of the alloy type and stoichiometry) [70]. This situation cause stresses in the material and the formation of voids which lead to degradation of the properties and/or geometrical arrangement of the material in the device.

The described phase-change behaviour shapes the optical or electrical switching pulses applied to a device or film in terms of their amplitude, duration and rise/fall times. For instance, amorphisation pulses are generally more intense (high amplitude) and shorter duration, with sharp falling edges in order to melt the material and achieve a high cooling rate afterwards. On the other hand, crystallisation pulses are longer and less intense, elevating the temperature of the material to the interval of temperatures where

crystallisation occurs and holding it in this situation until the crystallisation of the material is completed, see Figure 2.2. Furthermore, the thermal properties (such as thermal conductivity, specific heat and density) and the geometry of the materials (e.g. thicknesses of the layers for the different materials) surrounding the phase change material will also determine how heat escapes from the device and hence its correct operation in terms of switchability and energy efficiency. This last relationship (having fast enough cooling rates vs. energy consumption in the device) is one of the most important ones when designing phase-change based devices, as high cooling rates are necessary to reamorphise the phase-change material in the device, but high cooling rates can also adversely affect power consumption (since more power will be needed for a given temperature increase).

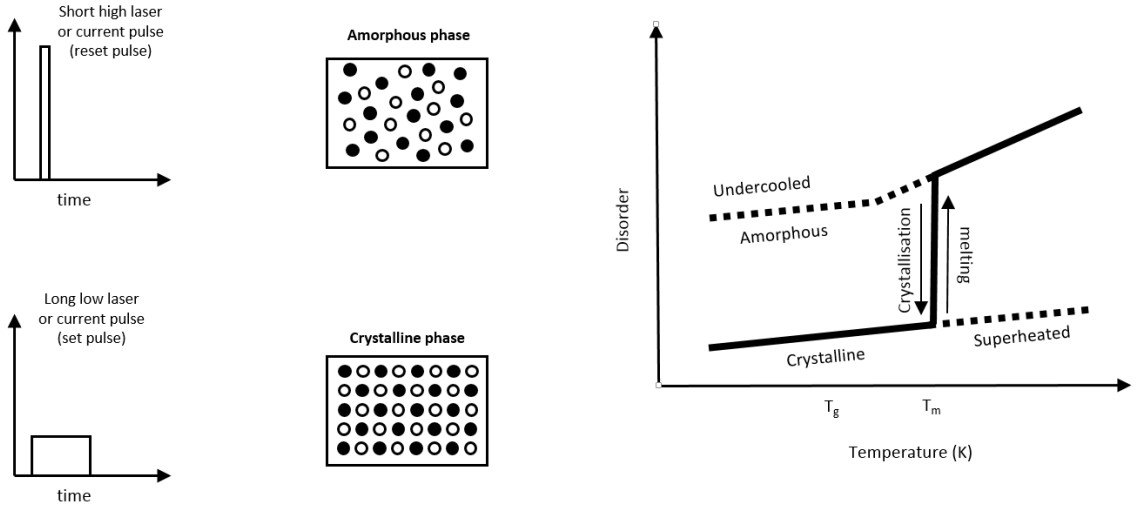

Figure 2.2. Figure illustrating the phase-change process. In the left part of the figure, a pictorial representation of the crystalline and amorphous phase is represented along with the kind of pulses necessary to obtain the referred phase. In the right part of the figure, a plot represents the different phases obtained depending of the temperature path followed. Note that there is an implicit dependence on the cooling rate in the different allowed paths.

2.1.2. Crystallisation thermodynamics and kinetics

In this section, the theory and parameters that allow us to understand the crystallisation process are discussed. It is convenient to start by considering classical nucleation and growth theory. This theory is the one that is most widely used to describe crystallisation in phase-change materials [64]. The classical nucleation and growth theory relies upon two main postulates. The first postulate states that crystallisation starts with a nucleation

process. The second postulate states that once the nuclei have a stable size, they will grow by aggregation of monomers (basic crystal units) into larger crystallites [2].

Historically, the description of the crystallisation process started by considering only thermodynamic aspects. More specifically, the necessary free energy $\Delta G_{cluster}$ for the formation of a crystal cluster depends on the temperature and size of the cluster *r* and is given by [2]

$$\Delta G_{cluster}(r) = -\Delta G_{lc,V} \cdot \frac{4}{3}\pi r^3 + \sigma \cdot 4\pi r^2 \qquad (2.1)$$

where $\Delta G_{lc,V}$ is the Gibbs free energy difference between the amorphous and the crystal phase per unit volume (temperature dependent term) and σ is the surface energy between the amorphous and crystalline phases per unit area. Note that the second term in Equation (2.1) is always of positive sign, indicating a contribution to revert the crystallisation in the material [64].

Using Equation (2.1) it is possible to determine the stability of the clusters in relation to the temperature of the material and the radius of the cluster. **Figure 2.3** contains a representation of $\Delta G_{cluster}$ as well as the volumetric and surface contributions for temperatures below the melting temperature. $\Delta G_{cluster}$ has a maximum for a value of *r* called the critical radius, r_c. For values of *r* below r_c, the surface contribution dominates and the values of $\Delta G_{cluster}$ monotonically increase with *r*, which indicates that the cluster is not stable and eventually will disappear. However, for values of *r* above r_c, the volumetric component dominates and the favourable process is that which makes the nucleus grow in size due to the reduction in $\Delta G_{cluster}$ as *r* increases. Therefore, the critical nucleus size represents an energy barrier that has to be overcome in order for the nucleus to become stable and grow, so the material will finally crystallise [2].

So far, the factors that will determine whether or not the reaction is favourable for crystallisation have been explained, that is, the thermodynamic part of the description. However, it is also equally important to know the factors that will give information about how fast the reaction will take place. For that, physical parameters have to be included in the theory that represents the kinetics of the reaction.

Crystallisation in phase-change materials is a diffusion-limited process. Meaning that the process involves a change of neighbours and/or coordination numbers. Therefore, there

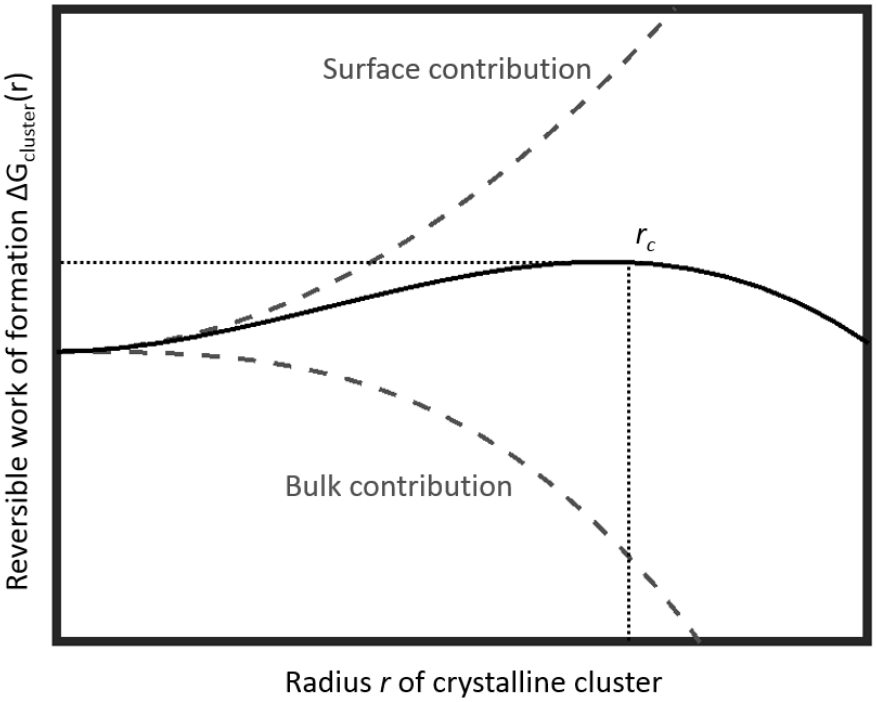

Figure 2.3. Free energy for cluster formation ($\Delta G_{cluster}(r)$) as a function of the cluster radius (r). It can be seen that for a nucleus with a radius smaller than the critical radius r_c, the direction of the process will be towards reducing the free energy and hence the dissolution of the nucleus. On the other hand, for a nucleus with a radius bigger than the critical size, the direction of the process will be towards increasing the nucleus size. The surface contribution and the bulk contribution of Equation 2.1 are represented by grey dashed lines.

will be a quantity called diffusivity *D* that describes how atoms jump across the interface between the crystalline and amorphous phases. *D* is expressed in terms of the viscosity due to the fact that it is easier to experimentally extract this value. Using the Stokes-Einstein equation [64] we obtain

$$\eta D = \frac{k_B T}{3\pi\lambda} \tag{2.2}$$

where η is the viscosity, k_B is the Boltzmann constant, T is temperature and λ is the interatomic distance. Therefore, it is the combination of these two factors, the driving force for nucleation (represented by the thermodynamic term) and the diffusivity of the atoms across the interface between the two phases (represented by the kinetic term, diffusivity-viscosity) that describes the crystallisation process. Both terms depend upon

temperature. At temperatures close to the crystallisation temperature the driving force for nucleation is very large but so is the viscosity, and the result is a very low change in crystallinity over time. A similar situation occurs close to melting temperature where the viscosity is very low but the driving force for nucleation is also very low, which also results in a very small change in crystallinity over time [3]. As said before, the highest rate for crystallisation is at some point in the middle of the crystallisation temperature and melting temperature.

2.1.3. Optical and electronic properties of phase-change materials[5]

As stated in Chapter 1, the devices in this thesis operate in the near-infrared and visible part of the electromagnetic spectrum. The optical constants of chalcogenide phase-change materials in the near-infrared part of the electromagnetic spectrum, specifically in the C-band for optical communications (1530-1565 nm wavelength, ~0.8 eV), display a low value for the extinction coefficient in general. For example, in the case of $Ge_2Sb_2Te_5$, an alloy extensively used in this thesis, the value of the extinction coefficient is $k_{am} \approx 0.098$ for the amorphous state while the value of the refractive index is moderately high for the same phase ($n_{am} \approx 3.71$). In the case of the crystalline phase in the C-band, the extinction coefficient is higher than in the amorphous phase ($k_{cr} \approx 0.90$) so is the refractive index ($n_{cr} \approx 5.98$). These values correspond to ellipsometry measurements (carried out by collaborators at University of Oxford) on films prepared in our laboratory. They are very similar to the values found in the literature [71,72] but not identical. As it has been said, it is a well-established fact that films prepared in different laboratories can present slightly different properties. See **Figure 2.4** for a comparison of our measured optical constants compared with a popular reference for the optical constants of $Ge_2Sb_2Te_5$.

On the other hand, the optical constants of many chalcogenide alloys in the visible part of the spectrum are very similar to each other [72]. They all possess a general trend

[5] Although the author is aware of the close link between electronic structure and optical constants and also other related effects such as optical nonlinearity, the discussion is going to adopt a merely descriptive character. That is, the physical origin and detailed explanation of light-matter interaction of chalcogenide phase-change materials and electromagnetic radiation at the wavelengths of interest is going to be substituted by the enunciation of their optical and electrical constants in both phases. This is done for the sake of brevity. A complete discussion on this topic can be found in Ref. [2].

towards reducing their relative contrast between amorphous and crystalline phases. The optical constants of chalcogenide phase-change materials in the amorphous phase are similar to those of a dielectric having a high value of their of extinction coefficient, while in the crystalline phase they are broadly similar to those of a metal [73].

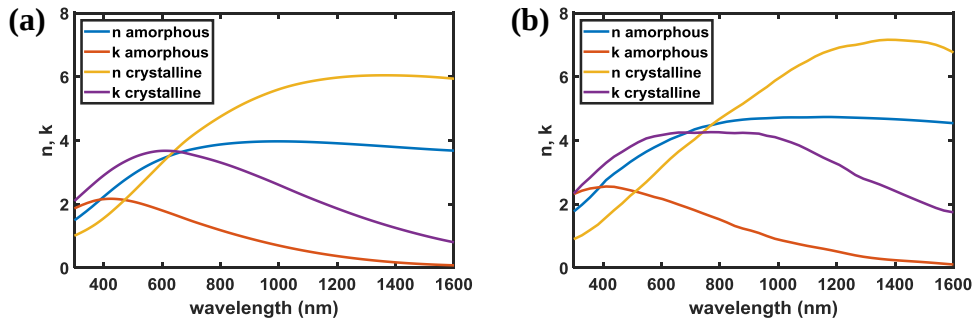

Figure 2.4. The refractive index and extinction coefficient of $Ge_2Sb_2Te_5$ for amorphous and crystalline phases in the near-infrared and the visible part of the electromagnetic spectra. **(a)** Refractive index measured from prepared films in our laboratories. **(b)** Refractive index measured from $Ge_2Sb_2Te_5$ in ref. [71].

The fact that the optical constants are fundamentally different in the visible and near-infrared part of the electromagnetic spectrum has a large impact on how devices are designed in these two spectral regions. This idea will be further elaborated later in this chapter (section 2.2.1.2), when the issue of combining metal-insulator-metal electromagnetic absorber structures with chalcogenide phase-change materials is addressed, and will become patent in the transition from Chapter 6 to Chapter 7.

GeTe was the phase-change material chosen to be used in the visible part of the electromagnetic spectrum, due to the strong contrast in its optical constants between amorphous and crystalline states at these wavelengths. As well as this, the metallic-like behaviour of the optical constants of in the visible part of the electromagnetic spectrum is slightly stronger in GeTe than in other phase-change materials, see [72]. In particular, the negative part of the relative permittivity is more negative and the imaginary part is bigger than in other phase-change alloys for the crystalline state. The relative permittivity of GeTe for their amorphous and crystalline phases is plotted in **Figure 2.5**.

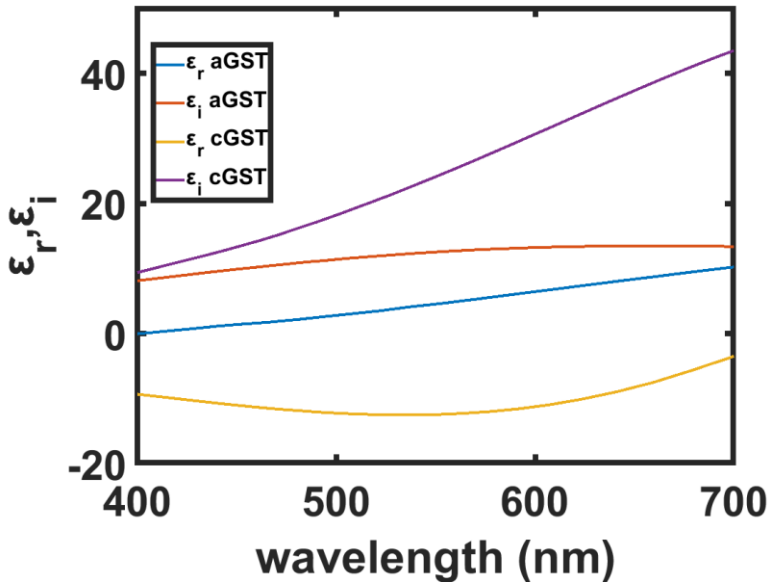

Figure 2.5. Relative permittivity for the amorphous and crystalline phases of GeTe used in this thesis. Data from ref [72].

Turning our attention to electronic properties, phase-change materials are characterised by a very strong contrast in electrical conductivity that can go, in the case of $Ge_2Sb_2Te_5$, from values of the order of 1 $(\Omega m)^{-1}$ in the amorphous state to values of the order of 10^3 $(\Omega m)^{-1}$ in the face centred cubic crystalline phase, both measured at room temperature [74]. The stable hexagonal phase of $Ge_2Sb_2Te_5$ displays an even higher conductivity that surpasses the electrical conductivity of the face centred cubic phase by approximately an order of magnitude, see **Figure 2.6**.

Along with this extraordinary change in the electrical conductivity, phase-change materials exhibit a remarkable conductivity behaviour in the amorphous phase. The amorphous phase does not present strong deviations of the electrical resistivity for relatively small values of the applied voltage up to a certain threshold [75–77]. When the threshold is surpassed the resistivity in the material drops abruptly, allowing a substantially higher current density and hence a raising of the temperature by Joule heating. In this way the material can be crystallised or melted. This phenomenon is called threshold switching, see **Figure 2.7**. From a physical point of view this process shares some similarities with dielectric breakdown in the sense that it is the value of the field across the material which determines the threshold for the sudden change in conductivity.

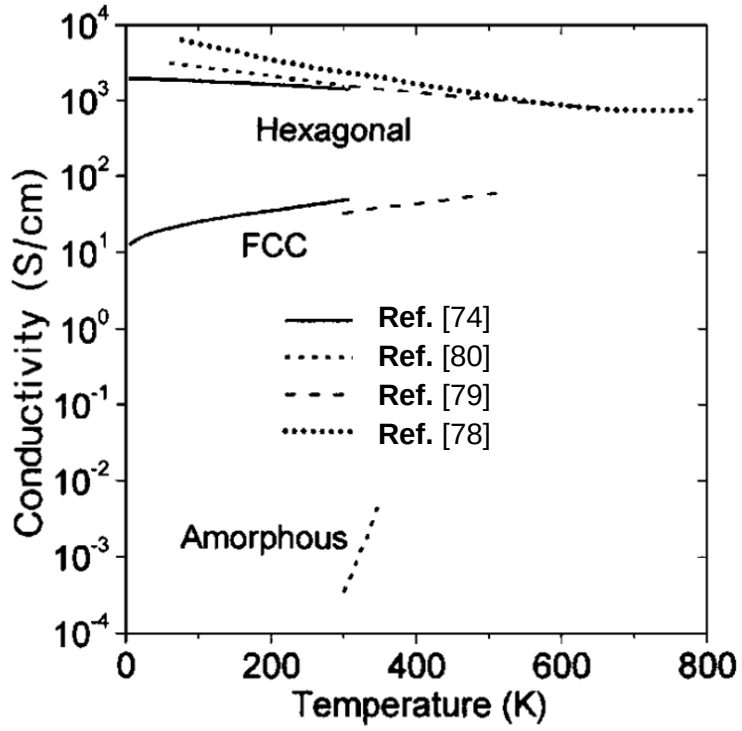

Figure 2.6. Conductivity of $Ge_2Sb_2Te_5$ as a function of temperature for the amorphous phase, the face centred cubic crystalline phase and the hexagonal crystalline phase, measured in references [74,78–80]. Figure adapted from ref. [74]. (Note 1 S/cm = 10^2 $(\Omega m)^{-1}$).

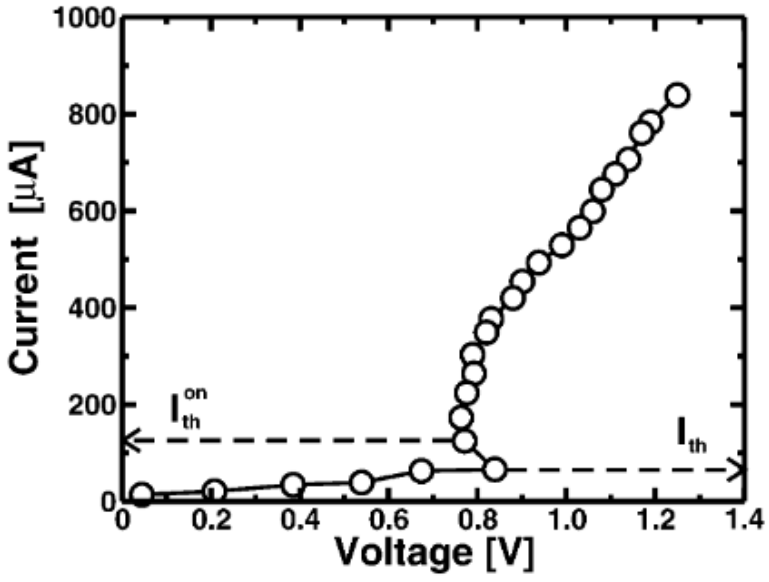

Figure 2.7. Threshold switching characteristic I-V curve in a phase-change memory cell. Figure from ref. [75].

2.2. Metasurface absorber structures

There exists a multitude of approaches in the literature to absorb electromagnetic radiation using an electromagnetically resonant structure. For instance, and speaking very broadly, it is possible to find metal-dielectric stacks that work as Fabry-Perot cavities [81], metallic gratings [82] and structures that take advantage of the excitation of localised surface plasmon polaritons [83], among others [84]. The structure that is the centre of attention in this thesis is a subtype of metasurfaces that uses the excitation of localised surface plasmons polaritons [85] as a mean of absorption, the so-called metal-insulator-metal metamaterial absorber. The basic characteristics and properties of these kind of structures are explained in the following subsections.

2.2.1. Metal-insulator-metal metasurface absorber structures

The structure of metal-insulator-metal metasurface absorber is composed of a bottom metal plane, a dielectric spacer and a top patterned metal layer [86]. See **Figure 2.8(a)** for a schematic representation of the metasurface. It is possible to find this structure in works ranging from microwaves [87], to the visible part of the spectrum [88] passing through the terahertz regime [89] and the whole infrared range [90–92].

The response of this kind of metasurface is characterised by a large value of the reflectance when the structure is out of resonance. When the structure enters into resonance, there is a drop in the value of the reflectance and part of the energy will be 'trapped' in the dielectric spacer and dissipated as heat, **Figure 2.8(b)** and **(c)**. The reason for this behaviour will be discussed more in detail in the next section and in Chapter 5.

The metal-insulator-metal structure is enormously popular in the literature due to the many interesting properties that it possesses. One of these properties is that it is relatively easy to fabricate using standard techniques, such as magnetron sputtering deposition or thermal evaporation to deposit the films and optical or electron beam lithography to create the top pattern. Moreover, it is possible to employ fabrication techniques that are more focussed on large scale production such as nanoimprint lithography [90] or displacement Talbot lithography [93].

Another interesting feature is the angle insensitivity that this structure is able to offer for any impinging polarisation [83,94,95]. This property is desirable in an absorber in general, and especially if moving parts are to be avoided. For instance, in the domain of solar energy harvesting or display technology, a low angle dependence of the designed response is a decisive feature.

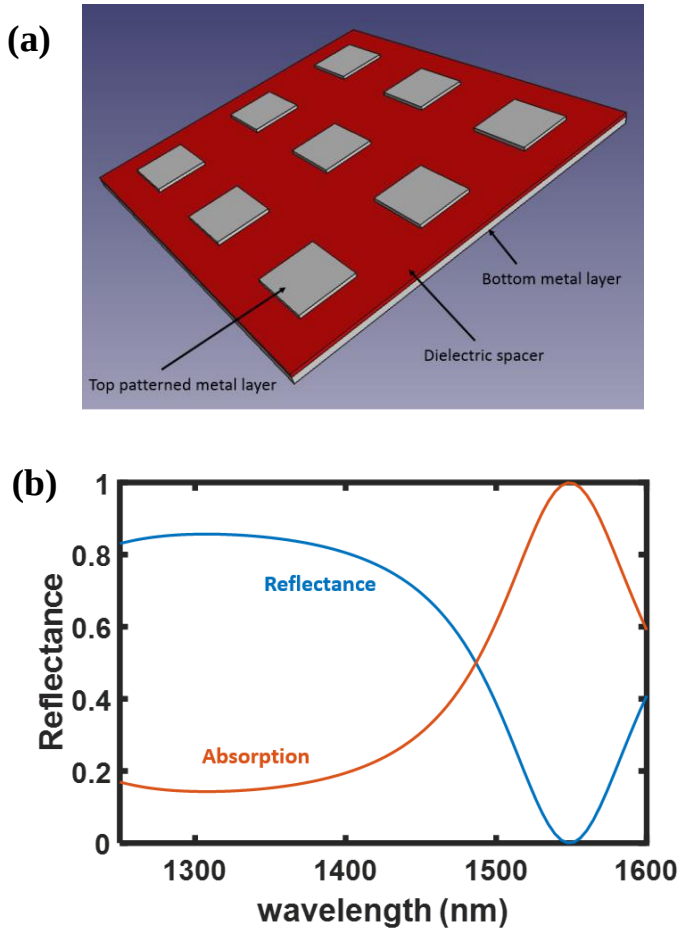

Figure 2.8. (a) Schematic representation of a metal-insulator-metal metamaterial absorber structure. **(b)** Calculated reflection absorption and transmission in a metal-insulator-metal metamaterial absorber structure of the type shown in (a).

2.2.1.1 Principle of operation of metal-insulator-metal metamaterial electromagnetic absorber structures

From the most general point of view, the occurrence of the absorption band in this kind of metasurface (as in many other structures) is caused by the destructive interference of

two outgoing waves, one coming from the reflection in the top part of the metasurface and the other is the wave that is radiated by the resonator when it is at resonance. Generally, this radiated energy comes from a transversal magnetic mode excited in the dielectric gap as a result of an electric dipole image coupling between the top and the bottom metallic parts, see **Figure 2.9**. There exists different regimes of operation that will depend on the strength of coupling (distance) between the bottom and top part metallic parts [83,90].

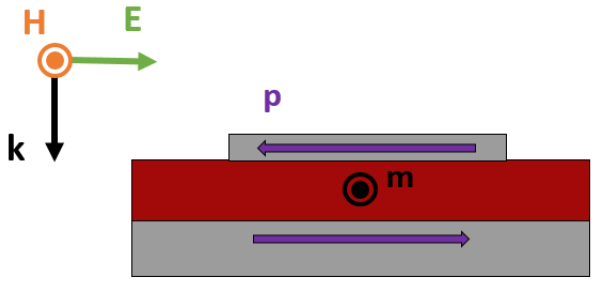

Figure 2.9. Representation of the fundamental resonant mode in the metal-insulator-metal meta-atom. It is possible to see an electric dipole on top and the image dipole in the bottom metal plane. As a result of the circulation of the electric field, a magnetic dipole appears in the interior of the cavities that is perpendicular to the electric dipoles and parallel to the metallic faces of the cavity. The polarisation of the incident field is indicated in the top left part of the figure.

If a more detailed description is required, what it is found in the literature is that there is no general way to describe the operation of metal-insulator-metal metamaterial absorber structures. Despite the fact that very frequently they share common points from the most fundamental point of view, such as the character of the resonant mode excited, the framework in which explanations of operation in the literature are formulated is often different at some level. Many descriptions differ in the language used or the emphasis put on some quantities to explain the operation, for example focusing on the effective refractive index of the cavity, the surface impedance or rate of energy dissipation.

Among the different approaches that exist to model the structures it is possible to find analogies with plasmon slot waveguides [88,96], impedance matching [83,97], application of the first Kerker condition [98], critical coupling theory [90,99] and

absorption cross-section considerations [100]. This discussion will be expanded in Chapter 5 where the design of this kind of metasurface and the operation will be described in more detail using relevant and related data.

2.2.1.2 Metal-insulator-metal metamaterial absorber structures combined with phase-change materials

As said in Chapter 1, phase-change materials offer very interesting possibilities when combined with metasurfaces, in particular the ability to provide a dynamic, tuneable, reconfigurable response. There are a number of publications in which the electromagnetic response of a metasurface is changed using a phase-change material, with applications explored including beam steering [60], chirality manipulation [101] and, the focus of this thesis, tunable absorption [58,102,103].

There have been some studies, most of them concentrated in the mid infrared [58,103,104], that give an idea of the spectral response that metal-insulator-metal metamaterial absorber structures in combination with phase-change materials can achieve. The strategy followed in the majority of such works was to place the phase-change material in the layer acting as the dielectric spacer. In that way, the resonant mode would be affected by the change in optical constants and shifted and/or attenuated, thereby changing the response of the metamaterial, **Figure 2.10**. The resulting spectral response has been demonstrated to be useful for applications such as microbolometers [58] or improving the absorption of the phase-change material to produce a more efficient optical switching [103]. However, very few (if any) studies have been focussed upon the challenges of designing and developing practicable tunable/reconfigurable devices, that is, to make a study of the different approaches and challenges that arise when trying to make devices that could, ultimately, be suited for commercial manufacture and real world operation. That is the reason why part of this thesis is dedicated to see what is possible to achieve in terms of optical response in the near infrared and visible part of the spectrum, but also there is a significant part of the effort dedicated to investigate what is possible to achieve in terms of switchability by optical and in-situ electrical means.

There has been also a small number of works combining phase-change materials with metamaterial absorber structures in the visible part of the spectrum [105,106]. The

achieved response did not attain a great level of tunability due to the reduced contrast in optical constants and the high extinction coefficient in both phases in the visible range, see Figure 2.4.

However, in Chapter 7 of this thesis, it is shown that by proper design metal-insulator-metal metasurfaces can be used to provide useful colour generation for display applications (see also next section).

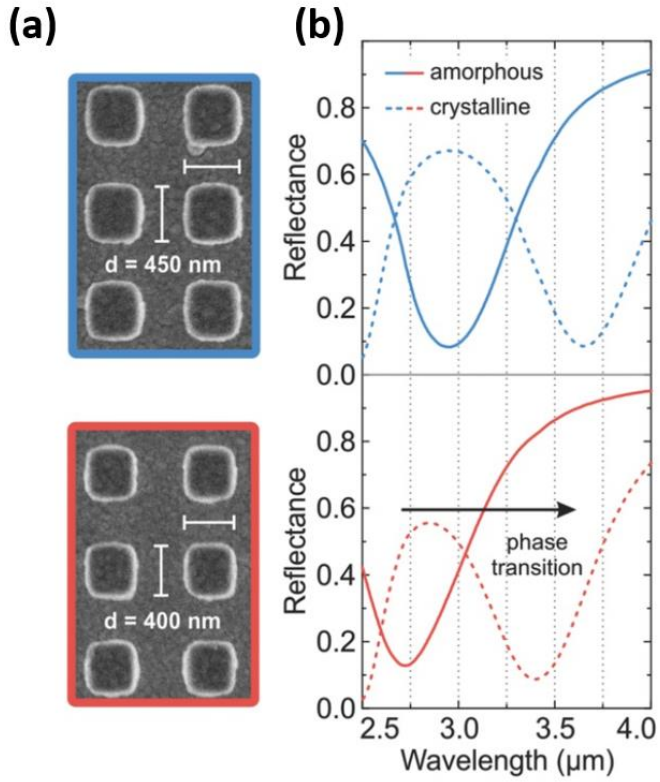

Figure 2.10. (a) SEM image from devices with different top metal pattern size. **(b)** Experimentally measured spectra from the devices in (a) for the phase change material in the amorphous and crystalline state**.** Figure from ref. [58].

2.3. Metasurfaces for colour generation

The use of metasurfaces working in the visible part of the electromagnetic spectrum has been proposed by several authors as a way to generate colours in reflection or transmission. Such an approach uses, in general, structural means to generate colours

(rather than pigmentation). Structural colour is also evident in nature, like in the case of some insects and the feathers of some birds [107]. Despite the fact that the origin of these structurally created colours present in nature is usually diffractive, many scientists, possibly inspired by this idea, started to use metasurfaces to create filters and reflectors to produce specifically designed colour responses.

Different approaches have thus been proposed to generate colours by means of metasurfaces [100,108–115]. One of the most common approaches is the use of arrays of metallic or metal-dielectric nanorods [100,111,112,115], similar to as displayed in **Figure 2.11(a)** and **(b)**.These structures are comprised in general of a back reflector on top of which there is an arrangement of pillars. The pillars are usually dielectric cylinders with a metal disk on top, although there are also publications in which the cylinders were entirely made of metal. The geometrical parameters usually used to shift the resonances, and hence produce a variation of the produced colour, are the diameter of the cylinder and the specific arrangement of the nanoresonators array [115].

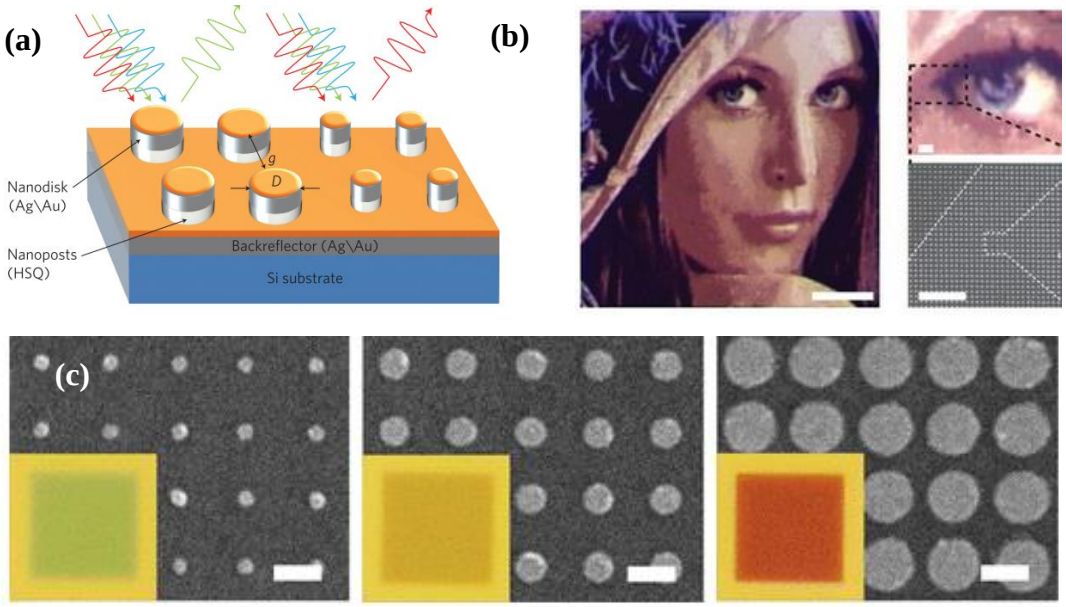

Figure 2.11. (a) Schematic of the structure and operation of metal-dielectric nanopillars (with back reflector) for colour generation [111] (scale bar 10 μm). **(b)** Image printed with the subwavelength structures in (a) (scale bar 1 μm). **(c)** SEM images of metal-insulator-metal absorber structures in ref. [114] and the colour they produce in the inset (scale bars 250 nm). Figures form ref. [111,114].

Another approach reported in the literature is the use of structures that rely on similar operation principles to those mentioned for metal-insulator-metal absorbers, **Figure 2.11(c)** [109,113,114]. They have in common that their operation is controlled by a resonant mode formed in the dielectric gap between the metallic (as in Figure 2.9) layers instead of relying on the combination of a plasmonic dipole resonance in combination with a metal back reflector as in the nanopillar approach (of Figure 2.11(a) and (b)).

Although metasurfaces of the type shown in Figure 2.11 can generate vivid colour palettes, their response is fixed (by the specific structure used) and so they cannot be used for display with changing or moving images. In Chapter 7, the possibility of combining phase-change materials with metamaterial absorber structures is explored with a view to dynamically manipulate the colour response, so potentially providing a new form of optoelectronic phase-change display.

2.4. Phase-change displays

The use of phase-change materials for display applications was first proposed in 2014 in the work of Hosseini et al. [23]. The proposed structure included a phase-change material as a switchable layer within a Fabry-Perot type cavity typically consisting of a (bottom) metal mirror layer, a bottom ITO electrode, the phase-change layer (typically $Ge_2Sb_2Te_5$) and a top ITO electrode, **Figure 2.12(a)** [23]. The display works in reflection, and interference effects in the cavity lead to the generation of colours that can be controlled by the thickness of the layers and, importantly, the phase-state of the chalcogenide layer (since the refractive index for the amorphous and crystalline phases differ greatly). By using a pixelated approach (in which different pixels have different layer thicknesses) combined with electrical or thermal switching of the phase-change layer between states [23] (or indeed to intermediate states [24]) bright, vividly-coloured and non-volatile reflective displays can be realized, **Figure 2.12(b)**. Non-volatility is a particularly attractive feature since no power is needed to retain an image once it is written into the phase-change layer/pixels.

Moreover, the displays can work using only ambient (natural or artificial) light, which can also significantly reduce power consumption; indeed, contrary to conventional

display technologies, the images generated in phase-change reflective displays are brighter the stronger the intensity of the incident light – another attractive feature. There are thus many exciting application possibilities for such phase-change displays, including mobiles, smart labelling, in-window displays, Internet of Things (IoT) devices, wearables, near-eye displays and even artificial retinas [23,116]. The range and uptake of such applications will, however, be undoubtedly extended and facilitated by approaches that improve and enhance colour control. In Chapter 7, this issue is addressed, and the use of metamaterial structures will be proposed to increase the versatility of phase-change based displays in terms of colour production.

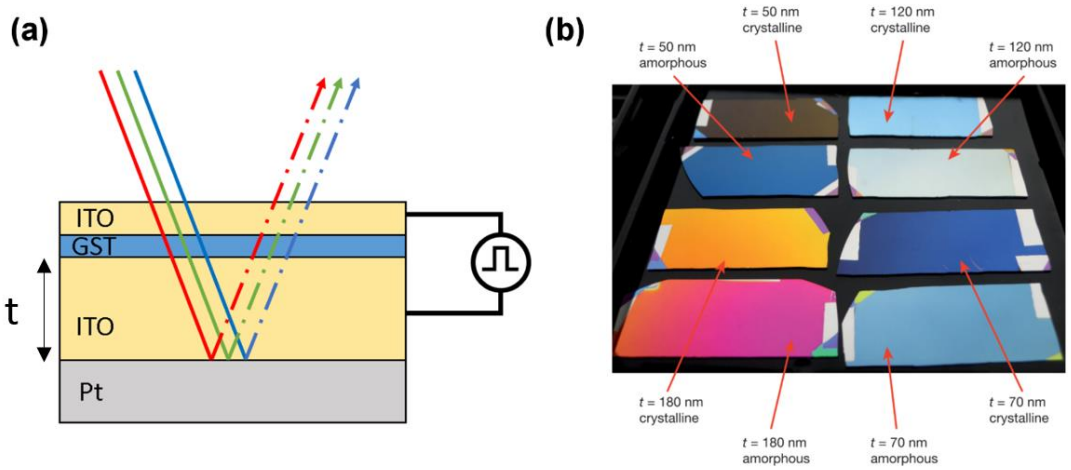

Figure 2.12. (a) Schematic representation of the operation and structure of the phase-change display in ref. [23]. White light (represented here by the red green and blue lines incident in the structure) is modified upon reflection in the different layers of the structure and subsequent interference. **(b)** Fabricated films where amorphous and crystalline phases results in different colours for the same geometry. Note that the varied parameter *t* between each pair of amorphous and crystalline devices corresponds to the bottom ITO layer over the Pt layer, all other parameters have the same value. The parameter t is used to control the produced colour in ref. [23]. Image from ref. [23].

Chapter 3 Computational and experimental techniques

The purpose of this chapter is to outline the methods and techniques used to carry out the different studies in the subsequent chapters. The techniques are categorised in two main groups, computational and experimental.

In the computational techniques part, the employed tools that have been used to perform the necessary calculations are outlined and discussed. These techniques include electromagnetic, electrical, thermal, and phase-change modelling, as well as optimisation methods.

The part covering experimental techniques comprises a compilation of the different fabrication and characterisation techniques employed, in particular magnetron sputtering, electron beam lithography and optical/electro-optical characterisation methods.

This discussion finishes with an overview of the process from the design to the characterisation of the devices, aiming for an integrated view of all steps involved in the process.

3.1. Computational techniques

3.1.1. Generalities

This section is written from the perspective of finding the best methods and tools to calculate the quantities that are needed in the studies carried out in this thesis.

The two most important factors to take into account when choosing a numerical technique to solve a problem of interest are, in general terms, the nature of the problem and the geometry of the problem. By nature of the problem, it is meant the equations that describe the physical process and its particularities. For example, whether the process is described by an ordinary differential equation or partial differential equation, or whether the equation is stiff or not. On the other hand, there are methods that can perform better

depending on the geometry, for example in the case of planar periodic structures or in the case of irregular shapes. The combination of these factors can help guide the researcher to the most appropriate strategy for solving a specific numerical problem associated to a physical situation.

The computations that are carried out in this thesis can be classified into five groups: electromagnetic, thermal, electrical, phase-change and optimisation calculations. In the case of the electromagnetic, thermal and electric simulations the computational tool COMSOL Multiphysics® has the capability of performing all the required analysis in the situations of interest, namely frequency studies in the electromagnetic case and time dependent studies in the thermal and electric simulation case (details of these studies to be explained in the next sections). As well as this, despite the fact that the geometry is quite regular in the devices developed in this thesis, the solution of the calculated quantities (electromagnetic fields, temperature…) in the structures can have regions where the mesh has to be very fine. This is due to abrupt change in space of the calculated quantities caused by situations such as penetration of electromagnetic fields in metals (which causes fields to decay exponentially as it enters in the metal) or regions with a very low thermal conductivity (which causes a very high gradient of temperature as the heat flows through them). The method that allows us to calculate the required quantities with superior versatility in terms of meshing is the finite element method that COMSOL Multiphysics® incorporates. The freedom and economy when building a mesh in using the finite element method can be much higher compared to other techniques, such as finite difference based algorithms where the use of complex meshing is more restricted.

In the case of the phase-change modelling, depending on the particular model implemented, an ordinary differential equation solver for stiff equations or a programmed cellular automata is used in this thesis. Both approaches can be implemented in Matlab®. Finally, for the case of the optimisation of the device structures in any aspect of their operation, an optimisation algorithm from the Global Optimisation toolbox from Maltlab® is linked via Livelink™ for Matlab® to a parametrised finite element model. The optimisation algorithm will then look for the optimal solution according to a properly specified fitness function and constraints. Optimisation approaches such as direct search and genetic algorithm are the main ones used in this thesis.

In the following subsections, the details regarding the modelling that has been carried out are presented.

3.1.2. Electromagnetic modelling

We are interested in designing devices with tailored (and tunable/reconfigurable) reflection/absorption spectra and (importantly) understanding and controlling the resonant conditions and properties of metasurfaces that combine phase-change materials and plasmonic structures. Hence, it is necessary to have a comprehensive understanding of the electromagnetic behaviour of the devices developed. In order to calculate the quantities of interest (e.g. reflection coefficient) a time-independent solution of the wave equation for the electric field is sufficient. To do this, the Helmholtz equation for the electric field[6] is solved:

$$\nabla \times (\nabla \times \mathbf{E}) - k_0^2 \left(\epsilon_r - \frac{j\sigma}{\omega \epsilon_0}\right) \mathbf{E} = 0 \tag{3.1}$$

where $\mathbf{E}$ denotes the electric field, k_0 is the free space wave vector, ϵ_r is the relative permittivity of the medium, σ is the electrical conductivity of the medium, ω is the angular frequency of the harmonic oscillation and ϵ_0 is the vacuum permittivity.

The boundary conditions employed in solving this equation are the following [117]:

- The *port boundary condition* allows one to specify the sources and defines the scattering matrix. The scattering parameters contained in the scattering matrix make a correspondence between the amplitude and phase of the excitation that impinges upon the structure through the different ports and the phase and amplitude of the scattered waves after interacting with the device. In the specific cases studied in the thesis, the structures have two ports, one will be an excitation port and another one will be a 'listening' port with no excitation. The excitation port is placed on top of the structure to send in the electromagnetic radiation and the listening port will be placed underneath the structure. It is possible to calculate

[6] Derivation of the Helmholtz equation can be found in ref. [199].

the amount of energy reflected and transmitted using the values of the fields at the chosen port boundary conditions.

- The *Floquet periodic boundary condition* allows the simulation of infinite periodic structures along a specified direction. This boundary condition has the following expression for the electric field:

$$\mathbf{E}_{\mathrm{dst}} = \mathbf{E}_{\mathrm{src}} e^{-i\mathbf{k}_{\mathbf{F}}\cdot(\mathbf{r}_{\mathrm{dst}}-\mathbf{r}_{\mathrm{src}})} \tag{3.2}$$

where $\mathbf{E}_{\mathrm{dst}}$ is the electric field at the destination boundary, $\mathbf{E}_{\mathrm{src}}$ is the electric field at the source boundary, $\mathbf{k}_{\mathrm{F}}$ is the Floquet wave-vector and the term $\mathbf{r}_{\mathrm{dst}}$-$\mathbf{r}_{\mathrm{src}}$ denotes a spatial vector that starts in the source boundary and ends at the destination boundary. Most of the time, the studied situation corresponds to normal incidence. In this case $\mathbf{k}_{\mathrm{F}}$ is equal to zero and the boundary condition is written as:

$$\mathbf{E}_{\mathrm{dst}} = \mathbf{E}_{\mathrm{src}} \tag{3.3}$$

- If **n** is a vector normal to the surface and **E** is the electric field then the *perfect electric conductor* boundary condition is defined as:

$$\mathbf{n} \times \mathbf{E} = \mathbf{0} \tag{3.4}$$

which means that the electric field is forced to be perpendicular to the boundary. This kind of boundary condition is very useful when a plane of symmetry exists in the solution of the fields, since it can be introduced in the plane of symmetry thereby halving the computational domain.

- The *perfect matched layer* allows the simulation of conditions of free space so the outgoing wave is absorbed in this domain and does not return back to the structure. Despite the fact it is not a true boundary condition, it is included in this part of the text as it represents an additional condition to the problem to extract a meaningful solution.

Figure 3.1 shows a pictorial representation on how the different boundary conditions are placed in the unit cell of a hypothetical device simulated in 2D.

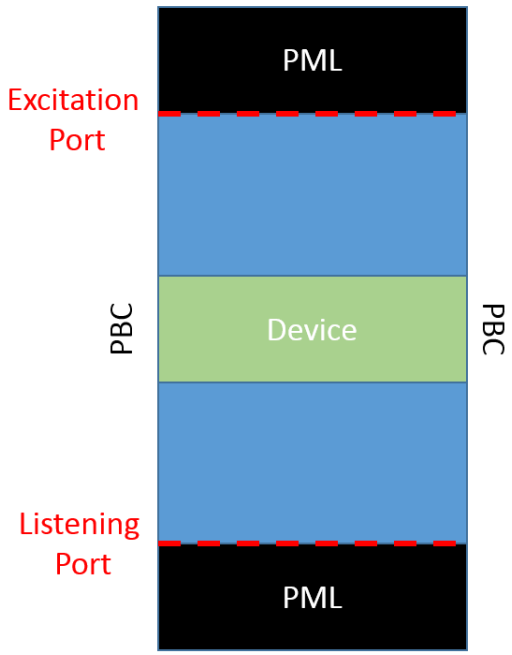

Figure 3.1. In this figure, the placement of the different boundary conditions explained in this section is shown for a 2D geometry. Periodic boundary conditions are placed on the sides of the device to simulate an infinitely large array in this direction. Port boundary conditions are placed on top and bottom of the unit cell. Finally, perfectly matched layers are placed behind each port to absorb the radiation that is reflected and transmitted from the device avoiding internal reflections. In the case that the produced solution has a plane of symmetry, the perfect electric conductor can be placed in such a plane to reduce the simulation domain to half.

3.1.3. Thermal modelling

The temperature evolution in the device structures developed in this thesis will be key to estimate quantities such as the power consumption, or the correct functioning of the structure in terms of switching the phase-change material embedded in the metasurface. The temperature evolution of the device is determined by the heat transfer equation, where only the conduction term needs to be considered[7]:

[7] Derivation of the heat transfer equation can be found in ref. [200].

$$DC_p \frac{\partial T}{\partial t} - \nabla \cdot (k \nabla T) = Q \tag{3.5}$$

where D represents the mass density, C_p represents the heat capacity at constant pressure, T is temperature and k is the thermal conductivity of the substance. Finally Q represents the volumetric heat source (provided by the particular optical, electrical or thermal excitation used).

The boundary conditions used in this case are [118]:

- The *periodic boundary condition* that enables the simulation of infinite periodic structures in a desired direction:

$$-\mathbf{n}_{\text{dst}} \cdot \mathbf{q}_{\text{dst}} = \mathbf{n}_{\text{src}} \cdot \mathbf{q}_{\text{src}} \quad \text{and} \quad T_{\text{dst}} = T_{\text{src}} \tag{3.6}$$

  where $\mathbf{n}_{\text{dst}}$ and $\mathbf{n}_{\text{src}}$ represent normal unitary vectors to the destination boundary and the source boundary respectively, $\mathbf{q}_{\text{dst}}$ and $\mathbf{q}_{\text{src}}$ represents the heat flux densities at the destination and the source boundaries respectively and T_{dst} and T_{src} represents the temperature at the destination and source boundary.

- The *temperature boundary condition*, is used to set parts of the computational domain (the ones that are deep and far away from the active regions of the device device) to room temperature.
- The *thermal insulation boundary* condition is used in parts of the structure where the heat flux is negligible, such as the case of device-air interfaces. The thermal insulation boundary condition is expressed as:

$$-\mathbf{n} \cdot \mathbf{q} = 0 \tag{3.7}$$

  where $\mathbf{n}$ is an unitary vector normal to the boundary and $\mathbf{q}$ is the vector that represents the heat flux density at the same point in the boundary.

3.1.4. Electrical modelling

The main purpose of electrical modelling of the device is to calculate the volumetric heat source described by a Joule heating process that can be used to switch the phase-change layer embedded in the metasurface. This volumetric heat source will be incorporated into the heat transfer model. To do this, it is necessary to know the value of the electrical current in the microheaters (used to switch the phase-change layer – see Chapter 6) when appropriate boundary conditions in terms of electric potential are applied.

Due to the regular geometry of the structures that are used here, the current and hence the dissipated power per unit volume is calculated using Ohm's Law. In other cases, the electric flux in the structure is obtained by solving the continuity equation for the charge:

$$\nabla \cdot \mathbf{J} = \frac{\partial \rho}{\partial t}, \quad \text{with} \quad \mathbf{J} = \sigma \mathbf{E} + \frac{\partial \mathbf{D}}{\partial t} \tag{3.8}$$

where **J** is the current density expressed as the sum of the conduction and displacement current density, ρ is the electric charge density, σ represents the electric conductivity, **E** is the electric field vector, **D** is the electric displacement [119]. In this case the only boundary conditions used are the values of the voltage in the outer boundaries of the model.

3.1.5. Device scale phase change models

The phase-change process can be simulated from two main frameworks. The first one is density functional theory where the material behaviour is extracted from first principle considerations. These kinds of simulations are very computationally intensive and the simulated region of material is very limited in size, therefore they are not suitable to simulate devices where the volumes of phase-change material are too big for this technique to handle. On the other hand, these techniques are ideal to study the fundamental properties of the material, such as electronic properties [2].

The other kind of phase-change simulation approach is what can be called device-scale phase-change models. These kinds of models can simulate large volumes of phase-change

material compared to density functional theory. As it has been said, most of the time, they have at their core concepts extracted from classical nucleation and growth theory. Some of the most important ones are the Johnson-Mehl-Avrami-Kohnogorov (JMAK) model [64,120], the Master Rate Equation model [121,122] and the Gillespie cellular automata model [123]. The Gillespie Cellular automata model has been used in this thesis in Chapter 4 and the Master Rate Equation model has been used in Chapter 6.

In the case of the Master Rate Equation, the model is formulated to find the concentration of crystal clusters formed by the agglomeration of *n* monomers (i.e. basic units of the crystal) at time *t*; this quantity is represented by *Z(n,t)*. Under the premise that a cluster of a size *n* can only grow or reduce its volume by attachment and detachment of monomers to the clusters immediately contiguous in size, the equation is written as [122]:

$$\frac{\partial Z(n,t)}{\partial t} = f(n-1,t)Z(n-1,t) + d(n+1,t)Z(n+1,t) - f(n,t)Z(n,t) - d(n,t)Z(n,t) \quad (3.9)$$

for n ≥ 2

where *f(n,t)* and *d(n,t)* are the rates of attachment and detachment respectively. All the parameters used to define these rates are, in this thesis, taken from ref. [124].

The implementation of the model results in a set of coupled differential equations that are solved in this thesis using Matlab®. Due to the stiff character of the equations in (3.9), the ordinary differential equation solver *ode15s* of Matlab® is used.

Once the model was implemented, validation was done by reproduction of the results in the supplementary information of [124]. **Figure 3.2** shows the comparison between the provided results shown in [124] and the data obtained from the implemented model in this thesis (and used in Chapter 6). Although a good degree of agreement can be observed, small differences between the two implementations can be possibly attributed to differences in the configuration of the solver (e.g. different tolerances used in each implementation). Furthermore, the way the terms of the model are implemented (i.e. mathematical expression of the terms in the model, or different order of the operations in each implementation) are well known sources of numerical errors that have some impact

on the precision of the calculations, especially when the quantities in the model varies over a large range of orders of magnitude such as in this case [125].

The Gillespie Cellular Automata model, on the other hand, produces simulation results in a slightly different way to the Master Equation model. The main difference between these two models is that the Master Equation returns information about the crystallinity only in terms of concentrations and relative populations of different cluster sizes, whereas the Gillespie Cellular Automata can give information about the actual spatial distribution of the crystallinity the material. This fact makes the Gillespie Cellular Automata very suitable for situations where the precise distribution of crystal/amorphous regions plays a key role in device performance. See **Figure 3.3**, for an example of the calculated crystallinity distribution inside a phase-change memory cell using the Gillespie Cellular Automata model [126].

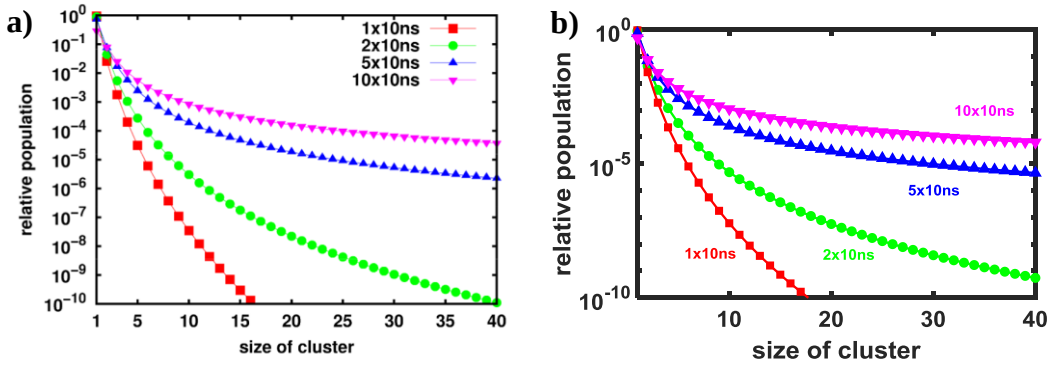

Figure 3.2. (a) Calculated relative population according to the cluster size for the phase change material at T = 700 K for 10 ns, 20 ns, 50 ns and 100 ns that corresponds to the model implemented in ref. [124]. **(b)** Same simulation as in (a) using the model implemented in this thesis. Both figures are compared in order to validate the implemented model. Image (a) from ref. [124].

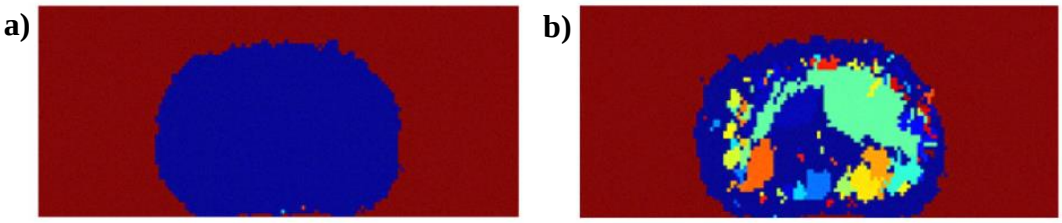

Figure 3.3. a) Phase-distribution in a phase-change memory cell calculated using the Gillespie Cellular Automata model. The region in red represents crystalline phase and the blue region represents material that has been melt-quenched in the amorphous state using an amorphisation pulse. **b)** Crystalline distribution in a) after the application of a crystallisation pulse. Part of the amorphous material has been crystallised. The new crystalline domains are represented in a variety of colours that represents different orientations of the crystals formed. Image from ref. [126].

3.1.6. Optimisation algorithms

The optimisation algorithms most prominently used in this thesis were the genetic algorithm and the direct search algorithm. The genetic algorithm is especially good in situations where there are a significantly high number of parameters to take into account for the optimisation, or where a first approach to the optimisation of a new structure is done. This is because the genetic algorithm can search more efficiently for a global minimum when the number of optimisation parameters is high or when the search space for the optimisation parameters is large. However, it is much slower to converge compared with direct search algorithm. Therefore, it is advisable to start using the genetic algorithm with a new structure with a wide search space for the parameters used in the optimisation, due to the unfamiliarity with the response of the device. Then, as soon as the global minimum is located, the search space is reduced and the optimisation algorithm is changed to direct search for a faster convergence. From that point, whenever some modifications are necessary in the structure it is enough to continue using direct search to optimise the structure [127].

The optimisation algorithms not only have been used to optimise selected figures of merit but also they have been used for other calculation purposes, such as the search for eigenmodes of a structure, as is reported in Chapter 5.

The algorithms used belong to the Global Optimisation toolbox from Matlab® and are linked to the COMSOL Multiphysics® model via Livelink™ for Matlab®.

3.2. Experimental Techniques

In this second part of the chapter the different experimental techniques for the fabrication and characterisation of the various structures and devices developed in this thesis are explained.

3.2.1. Thin film magnetron sputtering deposition

Sputtering deposition is classified inside the methods known as physical vapour deposition (PVD). The method consists of the vaporisation of a material (called "target") inside a vacuum chamber and the subsequent condensation in the solid phase on a substrate. The vaporisation of the substance to be deposited is caused by high energy collisions of the accelerated ions of a plasma. Once in the vapour phase, the atoms of the target material travel towards the substrate and they are deposited there. Usually, the plasma is formed by a noble gas, such as xenon or argon, under the action of an appropriate electric potential where the target is the cathode and the substrate and the wall chamber are the anode, **Figure 3.4**.

There are different modalities of this technique. For instance, in the *DC magnetron sputtering deposition* technique the use of magnetrons to confine the plasma in the target leads to higher deposition rates. Furthermore, DC magnetron sputtering is not suitable to deposit electrical insulating materials such as most oxides. However, the use of RF generators allows the generation of an alternating current in the insulating target (the target acts similarly to a capacitive load in the RF circuit), so allowing the plasma to spark and vapourise material from the target. This technique is known as *RF magnetron sputtering deposition*.

There are a number of parameters involved in the sputtering process, such as the pressure of the inert gas used to form the plasma, the electrical power used for the deposition or the temperature of the substrate. All these parameters will have an impact on the morphology of the layer in terms of roughness, compactness, stresses, average grain size

[128] or even purity [129], which in turn will impact physical properties such as electrical and thermal conductivity or refractive index.

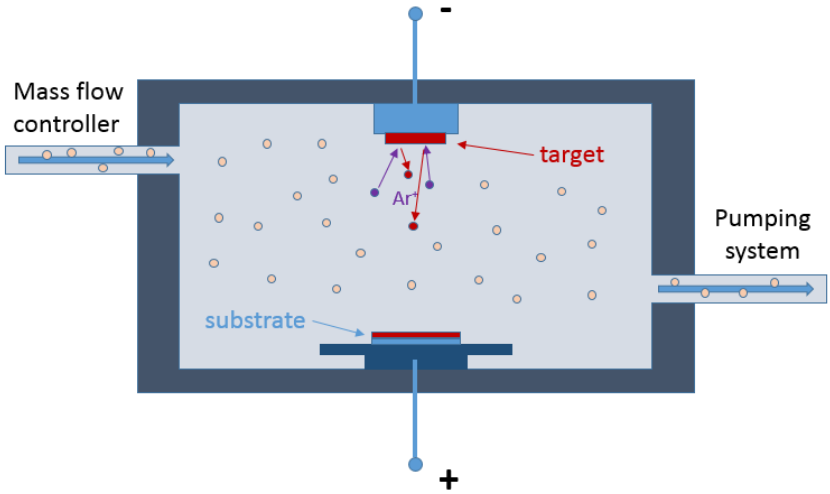

Figure 3.4. a) Schematic representation of the operation of a standard DC sputtering system. In this case the argon ions in the plasma are accelerated towards the target and, as a result of the impact, atoms are torn out of the target and end up being deposited on the substrate and on the wall of the chamber.

The thin films in the different devices developed in this thesis were deposited in three different machines at the University of Exeter:

- *Nordiko 2000:* This machine can be considered an industrial machine due to the size of the target materials (four spaces for targets of six inches in diameter, ideal for wafer-scale manufacture and optical disc memories deposition) and the quality of the base pressure achieved (~10^{-8} Torr). The machine comes with a rotary pump as primary pump and a cryo-pump as secondary pump. As well as this, it also has RF and DC capabilities, and therefore it is possible to deposit dielectrics as well as conductive materials.
- *Custom-built sputtering machine:* This machine is a purpose built sputtering machine with three spaces for targets of two inches in diameter. It has several advantages such as very good reliability and the fact that it is easy to repair. This machine has a rotary pump as a primary vacuum pump and a turbomolecular pump as a secondary pump. The usual base pressures achieved in this machine are not as good as in Nordiko 2000, however they are good enough to have good quality

films in the materials deposited in it (~10^{-6} Torr). The machine only comes with DC capabilities.

- *Moorfield nanoPVD model T10A:* The machine has three spaces for targets of two inches in diameter. In this system a scroll pump is the primary pump and a turbomolecular pump is the secondary pump. The base pressure achieved with this pump setup is on the order of 10^{-7} Torr. The machine comes with DC as well as RF capabilities.

In the appendix of this thesis there is a table with all the materials employed in the fabrication of the developed devices as well as the parameters for deposition and the machine used in the process.

3.2.2. Electron beam lithography

As said in the introduction, the devices that are developed in this thesis operate in the visible and near-infrared regions of the electromagnetic spectrum. This will cause their dimensions, and in particular the dimensions of the metallic patterns, to be sub-micron length. A suitable patterning technique that provides these kinds of resolution for the patterning of the structures is electron beam lithography.

The electron beam lithography process generally starts with the preparation of a thin film of resist on the substrate where the pattern is going to be written. The selection of the resist is important to control aspects such as the contrast of the mask or the exposure time. The resist is then baked at a temperature that depends on the resist composition or the kind of materials present in the substrate. The sample is then exposed to the beam of electrons in the selected areas that will (for a positive resist) break bonds of the resist polymer chain molecules. Once the exposure is complete, there will be a strong contrast in solubility between the exposed and unexposed parts of the resist to the substance that is used as a developer. The sample is then submerged in the developer for enough time to remove the parts exposed to the electron beam whilst minimally affecting the unexposed parts (and especially borders of the pattern). Finally, the material to be patterned is deposited followed by the removal of the remaining unexposed resist layer (lift-off). The complete process is schematically depicted in **Figure 3.5**.

Electron beam lithography is a complex process. This complexity mainly resides in the fact that there is high number of (interconnected) steps and considerations involved. The control over parameters such as thickness, type, temperature and time of baking for the resist; current, voltage and dose for the exposure; and time, temperature and mixture for the development process are key for the creation the resist mask. Therefore, usually it is necessary to adopt a systematic approach of calibrations and tests to make sure that the final result is suitable for the fabrication process.

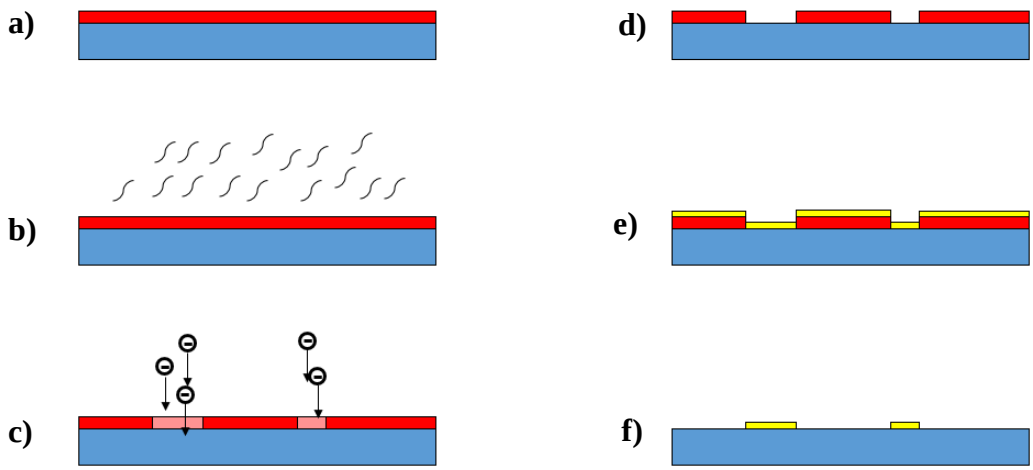

Figure 3.5. Steps in the lithography process. **a)** Spin coat resist (red) over substrate (blue). **b)** Pre-bake the spun substrate. **c)** Exposure of selected areas to the electron beam. **d)** Remove exposed part (in the case of a positive photoresist) in the development process. **e)** Deposit material to be patterned. **f)** Lift-off the remaining resist with the remover solution to finalise the patterning.

The system used in the fabrication of the devices in this thesis is a 30 kV to 100 kV *Nanobeam NB4 electron beam system*. The machine can deliver currents as small as ~1 nA that, along with the voltages used in the fabrication (80 kV), are ideal to get extremely high resolution patterns [130]. The system writes square fields of 250 μm that are stitched together using a 195 mm × 195 mm precision stage controlled by an interferometer with a position resolution 0.31 nm (λ/2048).

3.2.3. Scanning electron microscopy

Scanning electron microscopy was predominantly used in order to certify that the dimensions of the patterned structures fabricated by electron beam lithography were indeed correspondent to the ones in the models (i.e. to the design targets).

This technique is based on the exposure of the sample to an electron beam. The different processes that takes place after the interaction of the primary (sent) electrons with the surface of the specimen (mainly backscattered electrons, secondary electrons, auger electrons and X-ray emission) as well as appropriate detection and analysis of the collected data, allows the reconstruction of a very high resolution image of the surface of the sample. Also, it is possible to extract additional information such as the sample elemental composition.

The basic components of the system are [131]:

1. Electron emitter.
2. Column containing condenser electromagnetic lenses, deflection coils and apertures to focus and condition the exposure of the specimen to the electron beam.
3. Electron and X-ray detectors.
4. Input and output devices to control the exposure and display the image reconstructed by the system.

See **Figure 3.7**, for a schematic representation of a scanning electron microscope.

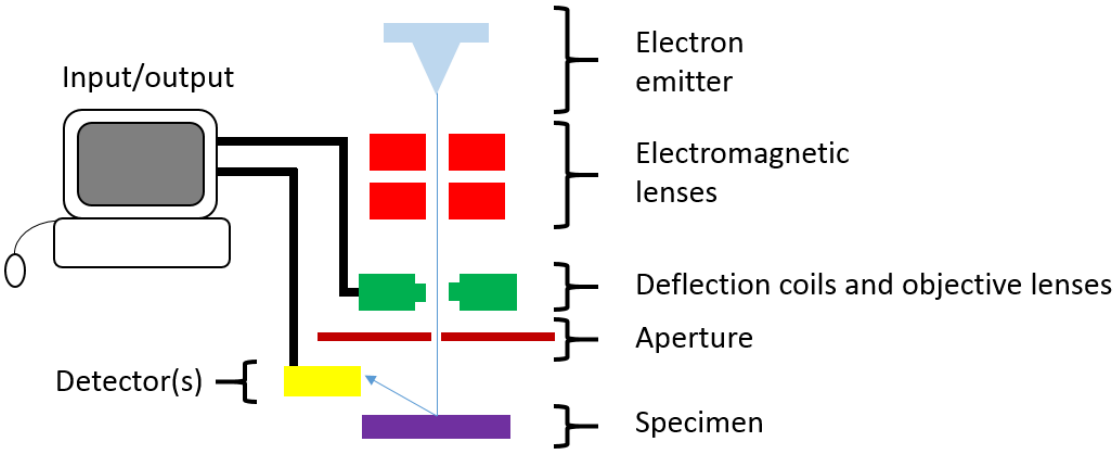

Figure 3.6. Basic structure and components of a scanning electron microscope.

The sample exposure in the devices measured in this thesis was usually done at a range of 30 to 10 kV and 0.13 nA. The maximum resolution that can be achieved with the scanning electron microscope used in this thesis is between 1 and 2 nm. A scanning electron microscope model *xT Nova Nanolab 600* was used to take the images of the fabricated devices in this thesis.

3.2.4. Spectroscopic measurements

Standalone spectroscopic measurements (not combined with electrical measurements) were carried out using a commercial *Jasco MSV-5300 UV-Visible/near-infrared Microspectrophotometer*. The range of measurement of the microspectrometer goes from 200 nm to 1600 nm wavelength. This spectrometer has three different objectives of different magnification and numerical apertures, plus other accessories such as internal polarisers that will be used in the measurement of the fabricated devices.

The measurement procedure starts by taking a measurement of the dark spectrum (S_{dark}) in the frequency band in which the measurement is going to be performed. This is done in a dark environment and with the objective out of focus with respect the surface underneath. This signal has to be subtracted from the reference mirror and sample acquired signals (S_{mirror} and S_{sample} respectively), to obtain the 'real' signal coming from the measured object, that is, excluding any contribution of the detector without illumination.

Once the dark signal has been removed from both the signal obtained from the reference mirror and from the signal obtained from the sample, both reference and sample signals are divided to get the reflectance spectrum of the sample. Finally, the obtained reflectance spectrum is corrected multiplying by the provided reflectance of the calibrated reference mirror (R_{mirror}). Thus, the reflectance of the samples is obtained with the following formula:

$$R = \frac{S_{sample} - S_{dark}}{S_{mirror} - S_{dark}} \times R_{mirror} \tag{3.10}$$

The system has three objectives, one Cassegrain reflective objective and two reflective objectives. The Cassegrain objective has 0.5 NA and x32 magnification. The other objectives have 0.3 NA, x20 magnification and 0.25 NA, x10 magnification.

In **Figure 3.7**, a schematic showing the components of a typical visible spectrometer is shown along with a schematic representation of a Cassegrain objective.

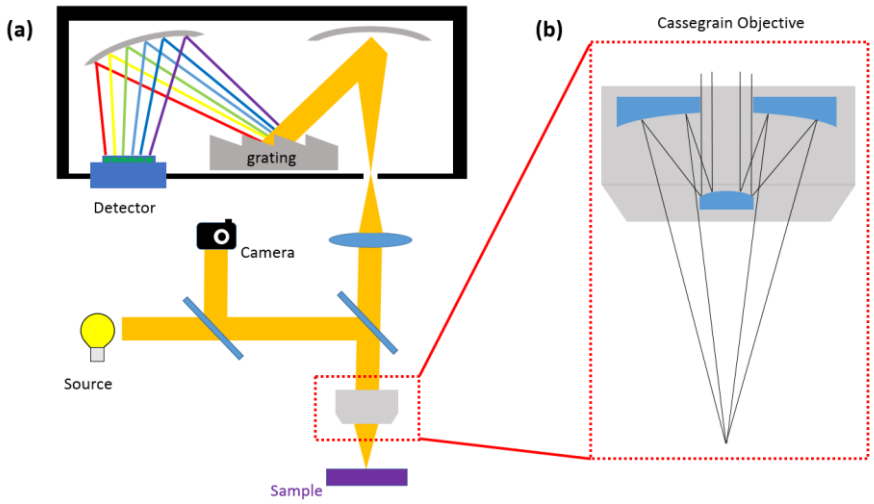

Figure 3.7. (a) Schematic representation of a visible spectrophotometer and Cassegrain objective. Light from the source travels to the sample passing through two beam splitters. After interacting with the sample, light is collected by the objective and travels back through the black box that represents the spectrometer (passing before through a beam splitter and a convergent lens). Light is then reflected in a parabolic mirror and impinges on a grating that separates light into different wavelengths. After that, another mirror reflects the different rays (wavelengths) to an array of photodiodes that will capture the spectral information. In addition to the path to the spectrometer from the sample there is an additional returning path to a camera to observe the sample and allow focussing prior to the measurement. **(b)** Schematic representation of a Cassegrain objective. Cassegrain objectives are useful to measure over large wavelength ranges (e.g. ultraviolet to near-infrared) due to the lack of chromatic aberration. Also, since they do not have refractive elements, additional absorption in the objective in spectral regions such as the ultraviolet and the near-infrared are non-existent which lead to a maximum signal collected from the apparatus.

3.2.5. Electro-optical measurements

The experiments that combine electrical and optical measurements were carried out in a purpose built optoelectronic probe station (built by Dr. Yat-Yin Au from our laboratory).

The system comes with several optical sources, namely a white and near-infrared source for spectroscopic measurements and a laser source for optical excitation of the samples. The system also comes with electrical pulse generators, oscilloscopes and probes to apply and monitor the electrical pulses sent to the devices. The two operations, optical and electrical, can be combined to perform mixed-mode measurements such as applying electric stimuli whilst measuring the optical response of the device, or vice-versa. The kinds of measurements relevant to this thesis and carried out in this system are optical excitation followed by optical measurement (Chapter 4) and electrical excitation followed by optical measurement (Chapter 6). A schematic of the optoelectronic probe station set up can be seen in **Figure 3.8**.

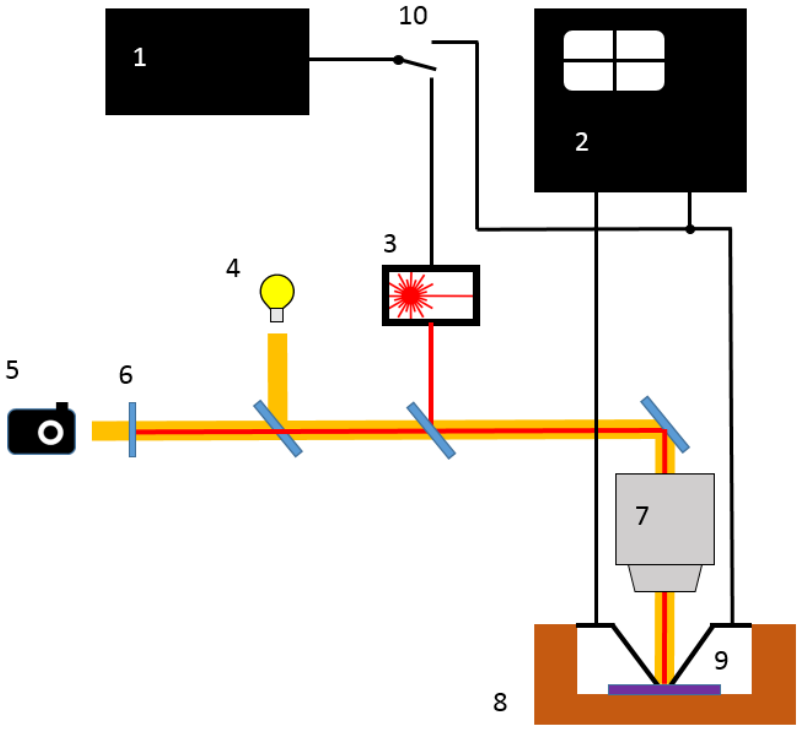

Figure 3.8. Optoelectronic probe station schematic (Only visible sources and detector represented). (1) Electrical pulse generator, (2) oscilloscope, (3) laser source, (4) visible source, (5) CMOS camera, (6) laser filter, (7) objective (8) piezoelectric stage, (9) sample and (10) switch to select optical or electrical pulsing.

In the measurements in which the devices are excited optically and measured optically, the sample is placed on the piezoelectric stage and the laser source sends pulses of

different powers and durations to induce switching cycles in the device. In this case, after each scan the spectrum of the exposed surface is acquired.

On the other hand, in the experiments in which electrical pulses were sent to the sample followed by an optical measurement, the sample is placed on the piezoelectric stage and a pair of low profile microprobes are placed onto the electrical contacts of the device. The electrical pulses are delivered to the device and the change in reflectance at selected wavelengths can be monitored in real time (see Chapter 6).

3.3. Process flow for design, fabrication and characterisation of devices

In this section the general procedure followed from the design of the devices to the final characterisation and measurement is outlined. The objective will be to capture a view on how all the different processes described in this chapter integrate with each other. The general procedure is explained here, any particularity on the fabrication of the devices will be reflected in the corresponding chapter.

Recall that the structure to be designed and fabricated is a metal-insulator-metal absorber such as the one shown in Figure 2.8(a) of Chapter 2. The design flow starts with the creation of the computational model that calculates the quantities of interest. An optimisation is then carried out in the case it is necessary. What is obtained from this step in general are the geometrical parameters that define the structure of the device.

Once the geometry of the device is known, the fabrication of the device starts with the deposition of the first set of layers via magnetron sputtering. The two first sets of layers are usually the bottom metal plane and the dielectric spacer that contains the phase-change material layer and the capping layer, typically ITO.

Following the deposition of the films, the sample is prepared for electron beam lithography to pattern the top metal layer. Firstly, 950K A4 PMMA layer is spun onto the stack of layers. After that, a soft bake of the substrate is carried out using 100 ^{o}C for 10 minutes (a low enough temperature to prevent crystallisation of the phase-change layer). The optimal electron dose using these parameters for the resist layer was found to be

between 6.5 and 9.5 C/m^2 for approximately 200 nm thickness of PMMA 950K. The difference in dose is mostly related with the size (area) of different exposed regions of the pattern and distance between them (it is advisable to use proximity effect correction for small and closely packed parts of the pattern to account for this issue). The dose is a parameter that usually is consistent if the same pattern is prepared under the same conditions in experiments not largely separated in time (days or weeks). Over long periods of time (months), the dose will be affected by ageing of the PMMA. To write sub-micron structures, the current of the electron beam should always be the lowest one that the machine can provide in order to have the maximum resolution and contrast in the resist pattern. Values ranging from 1nA to 2.5nA at 80kV were usually used to write small features, producing high contrast PMMA masks. Once the pattern is exposed, it is developed using a mixture 15:5:1 IPA:MIBK:MEK for 35 seconds and 45 in a pure IPA bath to stop the development process. The final step to get the PMMA mask consists in drying the sample using N_2 gas.[8]

The substrate with the deposited layers and the PMMA mask is then once again loaded into the sputtering system for the final metallisation step. The sample will then be ready for lift-off which is performed in a 60 ^oC acetone bath for two hours, followed by a mild sonication if necessary. The final step is removing any acetone residue in an IPA bath and drying with N_2. The device will be then ready to be measured in the microspectrometer or the optoelectronic probe station.

[8] The process to create the PMMA mask is applicable to all devices in the thesis, since the dimensions and the thickness of the patterning layer are similar in all of them.

Chapter 4 Phase-change Metamaterial Absorbers and Modulators

4.1. Introduction

Most previous work on GST-metamaterial structures has concentrated on the mid-infrared part of the spectrum, with applications such as improved energy absorption in optical memories [103], multispectral microbolometers [58] or tunable photonic crystals [132], but the near-infrared region has remained largely under-explored, due perhaps to the fact that the optical losses in GST start to rise appreciably in that region. However, operation in the near-infrared region is important since the most commonly used wavelengths for optical communications and optical signal processing lie in this region, specifically between 1530 nm to 1565 nm for the conventional C-band.

The purpose of this chapter is to look at the operation of phase-change based metal-insulator-metal electromagnetic absorbers as amplitude modulators from a general point of view. As a result of this, a clearer picture of the factors involved in the development of first prototypes and their suitability for near-infrared applications will be obtained.

Firstly, the performance of the conceived device is broadly and preliminarily assessed. A number of electromagnetic, electrothermal and phase-change simulations are carried out to infer the suitability for operation at near-infrared wavelengths. These calculations unravel information about several important figures of merit that allow us to determine the overall device performance. Such figures of merit are optimised according to an appropriate materials selection and structure design process.

In addition, various aspects concerning the practicability of the devices are also evaluated, such as estimation, via sensitivity analysis, of the impact of the tolerances during the fabrication process in the optimum calculated response of the device. As well as this, an investigation of compatible materials and non-normal incidence of the electromagnetic radiation onto the device is performed.

In the final part of this chapter, experimental results are included to test the optical performance of the as-designed devices, the phase-change layer in both the amorphous

and crystalline state. Furthermore, preliminary experiments are presented showing ex-situ switching of the device, carried out using a blue (405 nm) scanning diode laser.

To reiterate, the main outcomes of this chapter are:

- Presentation of a proto-structure for a phase-change based electro-optical amplitude modulator.
- Evaluation of important figures of merit and operation of the device via FEM simulations.
- Evaluation of the impact of the fabrication tolerances on the final response of the device.
- Exploration of compatible materials and non-normal incidence operation.
- Presentation of preliminary experimental results concerning the optical operation of the as-designed devices and ex-situ optical switching.

4.2. Device structure and materials

The proposed device structure is based on one suggested for operation at mid-infrared frequencies [58,103], **Figure 4.1(a)**. The structure consists of a 4-layer arrangement comprising a bottom metal layer, the chalcogenide phase-change layer, an ITO layer and a patterned top metal layer (here patterned into strips).

The choice and place in the structure of constituent materials will potentially have an impact on the performance and robustness of the device. One of the major concerns was the encapsulation of the active material (i.e. the chalcogenide phase-change layer) to protect it from environmental degradation. In previous studies [104,133], the requirement to protect the active chalcogenide alloy layer from the effects of oxidation appears to have been largely ignored. The properties of chalcogenide alloy thin films are known [134] to deteriorate rapidly on exposure to air and so for practicable absorber or modulator designs the chalcogenide phase-change layer should be encapsulated by a protective layer that, to maintain optical access and to allow for the possibility for electrical switching, should ideally be both optically transparent and electrically conductive [81]. Indium tin oxide (ITO) is used here to provide such a layer.

In addition, in terms of the choice of the composition of the (top and bottom) metal layers, gold and silver are usually the metals of choice in the literature, since they have excellent plasmonic behaviour. However, Ag is particularly diffusive, especially at the high temperatures experienced during the switching of the phase-change layer, and is thus best avoided. Aluminium has also been suggested as an alternative for the metal layers [58]. But, the melting point of aluminium (at ~660 °C) is relatively low, and in particular is very close to that (~620 °C) of the $Ge_2Sb_2Te_5$ (GST) alloy used here. Since to amorphise the GST layer it is necessary to heat it to above its melting temperature (and then cool it quickly), there is a danger that the top Al metal layer in particular would also melt (and, without any encapsulation, distort), a concern that should be kept in mind.

In cases where electrical switching of the phase-change layer is the intended approach, the choice for the metal layers should also be guided by electrical as well as optical considerations. Thus, for effective electrical switching of GST-based structures we might draw on the experience of phase-change memory developments, where tungsten (W) and titanium nitride (TiN) are the electrode materials of choice [135]. In this work therefore, and in a contrast to the usual practice, an exploration of the use of various materials (including Au, Al, W, Ti, TiN, Pt) for both the top and bottom metal layers has been carried out.

The plasmonic resonator structure proposed for operation in the C-band is, as said at the beginning of this section, of the form shown in **Figure 4.1(a)** and comprises a top metal layer (shown as Au in the figure) patterned into strips (or squares for a polarization insensitive design – see section 4.4.2), a 'dielectric' spacer, consisting of both the indium tin oxide (ITO) layer (for environmental protection) and the phase-switchable GST layer, and a (thick) metallic bottom layer. The interaction of the incident light with the structure (explained more in detail in section 2.2.1.1) is characterised by the excitation of a plasmonic resonance in the structure. This is possible due to the low extinction coefficient of amorphous GST at the targeted wavelength for operation. However, with the GST in the crystalline (high extinction coefficient) state, the resonant mode is significantly damped and displaced towards longer wavelengths. Under these conditions the structure is unable to resonate at the same frequency as in the amorphous state and the incident light is, as a result, mostly reflected.

4.3. Modelling the response of the device

4.3.1. Electromagnetic modelling and optimisation

The spectral reflectance properties of the phase-change metamaterial absorber/modulator were calculated by solving the wave equation for the electric field over the entire unit cell shown in **Figure 4.1(b)**. The employed approach is similar to the one explained in the section 3.1.2 of this thesis.

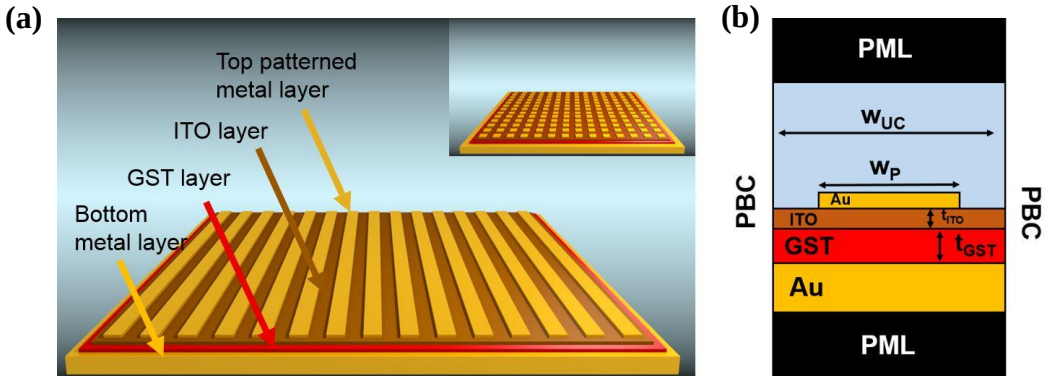

Figure 4.1. (a) Schematic of a thin-film phase-change metamaterial absorber/modulator (inset shows the top metal layer patterned into squares for a polarization insensitive design). **(b)** 2D cross section of the phase-change near-infrared absorber/modulator studied here and having a bottom metal layer (here shown as Au) of fixed thickness 80 nm, a top metal layer (again here shown as Au) of fixed thickness 30 nm (both gold layers have a 5 nm Ti adhesion layer not included in the figure for clarity) patterned into strips of variable width w_p, and GST and ITO layers with variable thicknesses t_{GST} and t_{ITO} respectively. For the design simulations a unit cell of width w_{uc} is used, with periodic boundary conditions (PBC) of Bloch-Floquet type assumed and a perfect matching layer (PML) placed at the top and bottom of the structure.

Input parameters to the simulation include the thicknesses and optical constants of each layer (electric permittivity/complex refractive index), along with the width of the strips (or size of squares) in the top metal layer and the size of the unit cell. For the case of the top metal layer patterned into strips, a 2D solution is sufficient, whereas for the top layer patterned into squares, a full 3D solution is required. There is a large difference in computational time between the 2D simulation (strips) and the 3D simulation (squares), here the top patterned layer is chosen to be formed by strips due to the reduced computational time required to calculate the required quantities of interest, resulting in

faster optimisation of the structures. Normal incidence is initially assumed and for the 2D case the incident polarization is assumed to be in the plane of the film and perpendicular to the direction of the patterned metal strips. For the case of the top metal layer patterned into squares, the polarization can be in any direction, but is assumed to be still in the plane of the film.

The values for the refractive index of the various metals explored were taken from the literature, specifically values for gold are taken from Johnson and Christy [136]; values for Al, W and Ti from [137]; and for TiN from [138]. The optical and electrical constants of ITO depend on several factors, in particular on the process conditions during deposition, as well as on any annealing regime used post-deposition. While post-deposition annealing generally increases the electrical conductivity of ITO, it also increases the extinction coefficient in the near-infrared region and therefore the optical losses, potentially leading to a deterioration of the optical performance of absorber/modulator designs investigated here. However, according to [139,140], the optical losses of ITO remain low in the near-infrared as long as there is no annealing after deposition; thus, here we assume ITO has the properties of un-annealed material and the relevant optical constants have been taken from published ellipsometry measurements in [53]. The optical constants of GST in both the amorphous and crystalline phase were taken from commonly-used values, as detailed in [141].

An optimization was also carried out, for which a pattern search algorithm [142] in the Matlab® optimization toolbox and LiveLink™ for Matlab® was used. In order to optimise the structure to work as an amplitude modulator, it is necessary to consider appropriate figures of merit with which to measure the performance of a particular modulator design. The modulation depth (MD) is used here which is defined [143] as the difference between the maximum reflected power P_{max} (which here will occur when the GST layer is in the crystalline phase) and the minimum reflected power P_{min} (here when the GST will be in the amorphous phase), normalized by the incident power (P_{inc}), i.e.

$$MD = \frac{P_{max} - P_{min}}{P_{inc}} = R_{cr} - R_{am} \tag{4.1}$$

where R_{cr} and R_{am} are the reflectance of the modulator when the GST layer is in the crystalline and amorphous phases respectively. Another commonly used figure of merit is the extinction ratio (ER), which is usually defined (for reflection modulators) in terms of the logarithm of the ratio of the maximum to the minimum reflected power, i.e.

$$ER = -10\log_{10}\frac{P_{max}}{P_{min}} = -10\log_{10}\frac{R_{cr}}{R_{am}} \tag{4.2}$$

A large modulation depth and high extinction ratio are always desirable, with ER values better than −7 dB being a typical design target for practicable modulators [144], although for some applications, such as short-reach optical interconnects, an ER around of −5 dB is often considered to be sufficient [57].

Using the Matlab® pattern search algorithm, the structure in Figure 4.1 was optimized in terms of the maximum modulation depth. For these simulations, the top and bottom metal layers were assumed to be made of gold. The dimensions of the unit cell (w_{uc}), the top Au layer strip width (w_p), the thickness of the ITO layer (t_{ITO}) and the thickness of the GST layer itself (t_{GST}) were all allowed to vary, while the thicknesses of the top and bottom Au layers were fixed at 30 nm and 80 nm respectively (with an additional 5 nm Ti adhesion layer). The dimensions that give an optimized (maximum) *MD* at 1550 nm were found to be w_{uc} = 493.3 nm, w_p = 333.8 nm, t_{GST} = 64.1 nm and t_{ITO} = 5.0 nm. Note that the optimum thickness of the ITO layer, t_{ITO}, returned by the optimization algorithm is coincident with the lowest bound set for the search in the parameter space (this lower limit having been chosen to ensure reliable deposition of the continuous layer of ITO needed for the desired environmental protection of the GST layer). The simulated reflectance spectrum of this optimized modulator, with the GST layer in both the crystalline and the amorphous states, is shown in **Figure 4.2(a)**, while the extinction ratio is shown in **Figure 4.2(b)**.

It is clear from Figure 4.2 that the optimally designed modulator should provide excellent performance, with optimum values for *MD* and *ER* being very high, at 0.767 and -19.8 dB respectively for the target wavelength of 1550 nm.

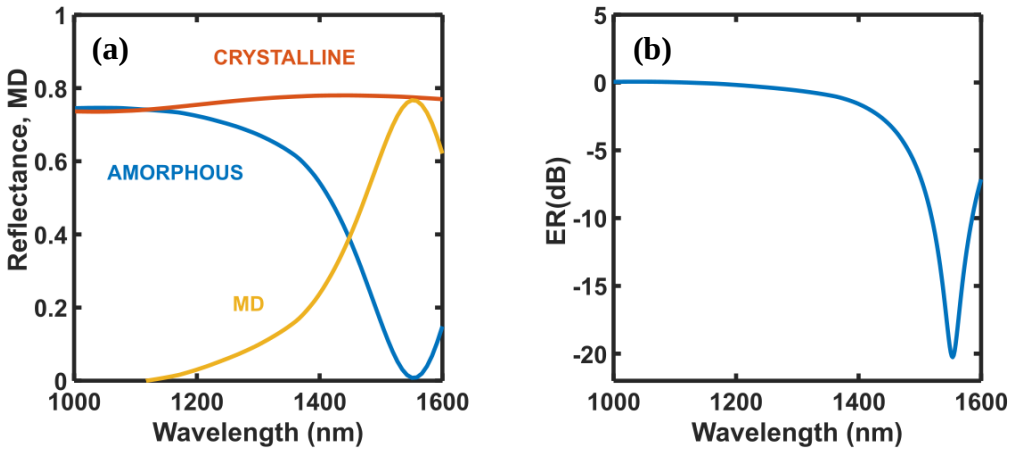

Figure 4.2. (a) Simulated reflectance spectrum for the design in Figure 4.1 with Au top and bottom metal layers and with the phase-change layer in both the crystalline and amorphous states. The chalcogenide phase-change layer here is $Ge_2Sb_2Te_5$ (GST) and the design was optimized for maximum modulation depth (MD) at 1550 nm. Also shown **(b)** is the extinction ratio.

4.3.2. Electrothermal and phase-change modelling

With regard to the modelling of the electrical phase-switching behaviour of GST, a combined electro-thermal simulation tool that simultaneously solves the Laplace and heat-diffusion equation was used in order to determine the temperature distribution throughout the structure at each simulation time step. This temperature distribution feeds into a Gillespie cellular automata (GCA) model that solves for the phase (i.e. determines if each cell in the simulation is in the melted, amorphous or crystalline state) using a rate-equation approach. This electro-thermal-GCA model (developed by colleagues at Exeter) has proved to be capable of realistic simulations of both blanket thin-film behaviour and phase-change device operation, and has been described in detail in previous works [123,145,146].

A key feature of phase-change metadevices is of course the ability to dynamically change/tune/reconfigure the device response by switching the phase-change layer between the amorphous and crystalline states (or indeed to some intermediate mixed phase). It is crucial therefore that devices be designed from the outset to enable such switching to occur, either by electrical or optical means. Any device structure needs

therefore to be designed to enable the phase-change layer to be heated, by appropriate excitations, to the requisite temperatures and also to allow sufficiently fast cooling for the amorphous phase to form.

Phase-change metadevices so far reported in the literature have generally been switched ex-situ using fast, high-power external lasers, or simply by carrying out thermal annealing in an oven to induce a one-way transition from the amorphous to crystalline phase (due to the fast cooling requirements, oven annealing cannot be used to form the amorphous phase) [69]. For real-world applications however, some form of in-situ switching of the phase-change layer would be most attractive. In our case, this might be achieved by dividing the absorber/modulator structure of the form shown in Figure 4.1 into an arrangement of pixels, each of which could be separately excited electrically in order to switch the phase-change layer (for example, in the case of a modulator with the topmost metal layer patterned into strips, one might also pattern the bottom metal layer into (orthogonal) strips, yielding a structure electrically similar to the commonly used cross-bar memory devices in which individual 'cells' are addressed by appropriate excitations being placed on the relevant intersecting strips - the so-called 'bit' and 'word' lines in memory device terminology [81,135]). This is an interesting approach to be considered, however it is not the only one, as will become apparent in Chapter 6.

Thus, electrical switching was simulated by assuming each pixel is represented by the unit-cell of the form shown in Figure 4.1(b) (with dimensions optimized for maximum modulation depth as in Figure 4.2) and applying appropriate electrical pulses between the top and bottom metal layers of the structure in order to determine whether amorphisation and crystallization of the phase-change layer can indeed by achieved using in-situ electrical switching. Typical results are shown in **Figure 4.3**, here for the case of Au top and bottom metal layers (though similar results were obtained for Al, W and TiN) using a 2.4 V, 50ns (15/5 ns rise/fall time) amorphisation, or so-called RESET, pulse and a 1.4 V, 100 ns (30 ns rise/fall time) crystallization, or so-called SET, pulse. In **Figure 4.3(a)** the temperature distributions throughout the unit-cell at the time (during the excitation pulse) at which the maximum temperature occurs for both RESET and SET pulses are shown. During the RESET pulse the maximum temperature does indeed exceed the melting point of GST (620 °C or 893 K), and the temperature distribution is relatively uniform throughout the GST layer. It is worth noticing that the temperature experienced

by the top metal layer is also relatively high in this case (~980 K), precluding the use of aluminium (melting point ~933 K) for the top layer, as discussed in section 4.2 (replacing the top Au layer with Al in the simulations shown in Figure 4.3(a) did not significantly affect the maximum temperature reached). During the SET pulse, the maximum temperature experienced by the GST layer is in the region of 720 K or 447 °C, a typical value required to ensure rapid (on the order of tens of nanoseconds) crystallization of GST [146]. In **Figure 4.3(b)** it is possible to see the starting and finishing phase states of the GST layer (calculated using our Gillespie Cellular Automata approach –see [123]) after a sequence of RESET/SET/RESET pulses: the GST layer starts in the fully crystalline state (shown brown in Figure 4.3(b)); after the application of a first RESET pulse the GST layer is fully amorphised (shown blue in Figure 4.3(b)); after the application of the SET pulse the GST layer is fully re-crystallized (into a number of crystallites, as shown by the different colours in Figure 4.3(b)); finally, after the receipt of a second RESET pulse the GST layer is fully re-amorphised.

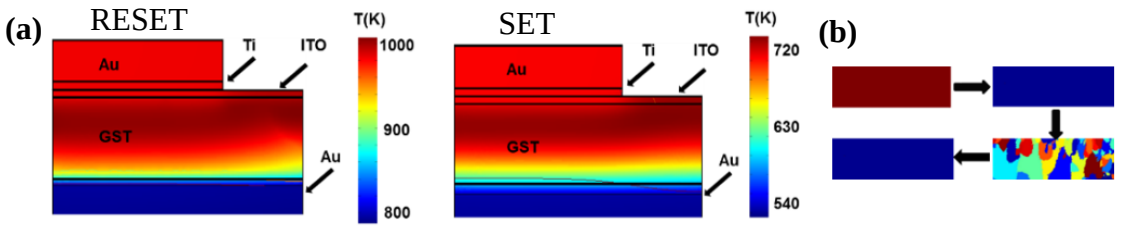

Figure 4.3. (a) Simulated temperature distributions in the structure of Figure 1(b) for the case of electrical excitation (assuming an electrically pixelated structure with pixel size equal to the unit-cell size) for (left) a RESET (amorphisation) pulse of 2.4V/50 ns and (right) a SET (crystallisation) pulse of 1.4V/100ns respectively. **(b)** The starting and finishing phase-states of the GST layer after a sequence of RESET/SET/RESET electrical excitations: the GST layer starts in the fully crystalline state (shown brown); after the application of a first RESET pulse the GST layer is fully amorphised (shown blue); after the application of a SET pulse the GST layer is fully re-crystallized (into a number of crystallites, as shown by the different colours); finally, after the receipt of a second RESET pulse the GST layer is fully re-amorphised.

Thus it would appear, at least from a simulation perspective (and for the material properties shown in **Table 4.1**), that phase-change metadevices of the form described above would indeed be suited to in-situ electrical switching of the phase-change layer, so

providing a readily active/tunable/reconfigurable photonic response. (It is worth also to highlight that, to avoid any possible concerns of gold diffusion from the bottom metal layer into the GST layer [57], an additional ITO layer can be inserted on top of the bottom Au layer without any detrimental effects, in an appropriately optimized structure, on the overall electrical or optical performance).

Table 4.1. Materials parameters used in phase-switching simulations of Figure 4.3.

Material	Thermal Conductivity ($Wm^{-1}K^{-1}$)	Heat Capacity ($Jkg^{-1}K^{-1}$)	Electrical Conductivity ($\Omega^{-1}m^{-1}$)
Au	310	129	44×10^{6}
ITO	11	340	8.3×10^{3}
Ti	7.5	710	7.4×10^{5}
GST (Amorphous)	0.2	210	See (A)
GST (Crystalline)	0.58	210	See (A)
Si (Substrate)	149	720	100

(A) C D Wright et al., IEEE Transactions on Nanotechnology 5, 1 (2006)

4.3.3. Alternative materials for the electrode/resonator

As discussed above, the effect on modulator optical performance of the choice of different materials for the top and bottom metal layers was also investigated, rather than simply using the de facto choice, from a plasmonic perspective, of gold. Specifically we compared the use of Au against that of Al, W and TiN. It was found that one could obtain excellent absorber/modulator optical performance when Al was used for the top and bottom layers, as shown in **Figure 4.4(b)** and as also reported, for the MIR range, in the literature [58] (but note previous comments regarding the possible unsuitability of Al due to its low melting point). An excellent absorber/modulator performance could be obtained if W and TiN (typical electrode materials in phase-change memory devices) were used for the top metal layer only, but not if used for the top and bottom layers, as shown in **Figure 4.4(c)** and **Figure 4.4(d)** (note that **Figure 4.4(a)** corresponds to the results of **Figure 4.2(a)** and they are placed here for comparison purposes). This issue will become clearer in the next chapter where a detailed explanation on the relation of

coupling of light to the structure (in particular critical coupling) is discussed. The results of Figure 4.4 certainly show that, at least from an optical perspective, the choice of metals available for use in these phase-change metadevice structures is much wider than the usual plasmonic favourites of Au or Ag.

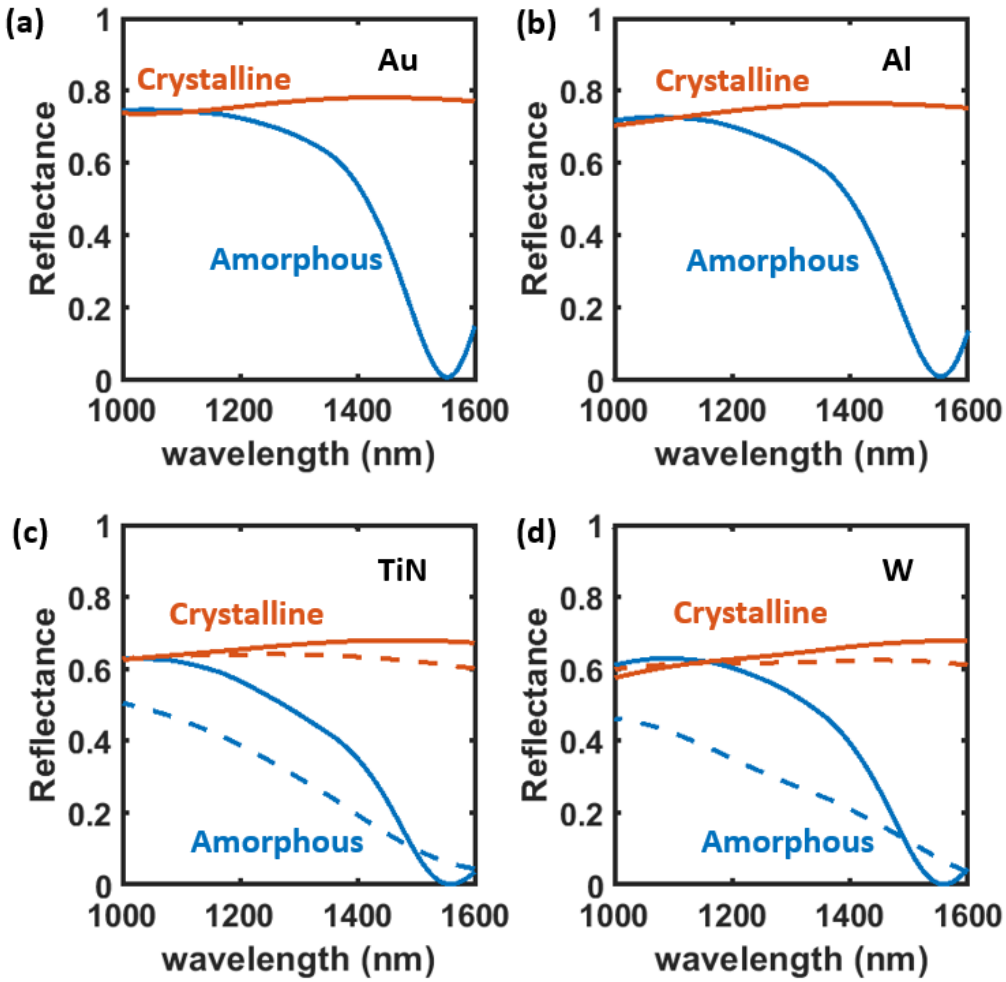

Figure 4.4. The reflectance spectrum for optimized (in terms of MD at 1550 nm) phase-change modulators of the form of Figure 4.1 but with **(a)** Au top and bottom layer, (b) Al top and bottom layer**, (c)** (i) TiN top and bottom layers (dotted lines) and (ii) TiN top and Au bottom metal layers (solid lines) and **(d)** (i) W top and bottom layers (dotted lines) and (ii) W top and Au bottom metal layers (solid lines). In all cases red lines show results for the GST layer in the crystalline phase and blue the amorphous phase.

The achievement of less restrictive conditions regarding the choice of the top electrode will be important in Chapter 6 when the subject of in-situ switching using a microheater approach is addressed.

4.4. Modelling additional aspects of interest

4.4.1. Sensitivity analysis

A potential drawback of the optimization methods used in the previous section is that the optimal solution returns very precise values of the key design parameters for the modulator, i.e. the ITO and GST layer thicknesses, the width of the strips in the top metal layer and the unit cell dimensions. Achieving such precise values using a practicable manufacturing method is very unlikely, at least with any degree of cost effectiveness. Indeed, using common deposition methods, such as magnetron sputtering, for the various layers in the stack one might expect a thickness tolerance of perhaps ± 1 nm at best. Standard lithography techniques for the patterning of the top layer, such as electron beam lithography, would also be expected to have similar, if not even larger, tolerances. It is therefore important, from a fabrication and manufacturing perspective, to understand how the performance of the optimally designed modulator is affected (deteriorated) by such fabrication tolerances.

This problem is addressed via a sensitivity analysis, simulating the performance of the modulator over a region of parameter space defined by the realistic tolerances in the thicknesses of the GST and ITO layers and in the size (width) of the strips in the top metal layer. Normally-distributed layer thicknesses (t_{GST} and t_{ITO}) with (standard deviation) σ = 0.5 nm were assumed, along with normally-distributed strip width and unit-cell dimensions (w_p and w_{uc}) with σ=7.5 nm, and the modulation depth, MD, was calculated for a total of over 2000 points randomly distributed in the parameter space encompassed by these variations. Results, for the absorber/modulator of Figure 4.1 (and with Au top and bottom metal layers) are given in the scatter plots of **Figure 4.5** where the MD for all points in the parameter space lying within ± 2σ of the mean values of t_{GST}, t_{ITO}, w_p and w_{uc} is shown. It can be seen that the parameters having most effect on modulator performance (at least on the modulation depth) are the thickness of the ITO layer and the

width of the strips in the top metal layer (in particular the former). From all the produced solutions, the mean and the standard deviation can be calculated to give an idea of how these solutions (for the modulation depth) are distributed with respect the optimum value which, as said before, was MD = 0.767 (as in Figure 4.2(a)). Thus, for the solutions shown in Figure 4.5, the mean value of the modulation depth is 0.760 with a standard deviation of σ_{MD} = 0.008. The fact that the mean is so close to the optimal value and the standard deviation is relatively small tells us that our design is indeed stable to the tolerances in layer thicknesses and lithographic patterning expected to arise as a result of typical fabrication/manufacturing processes.

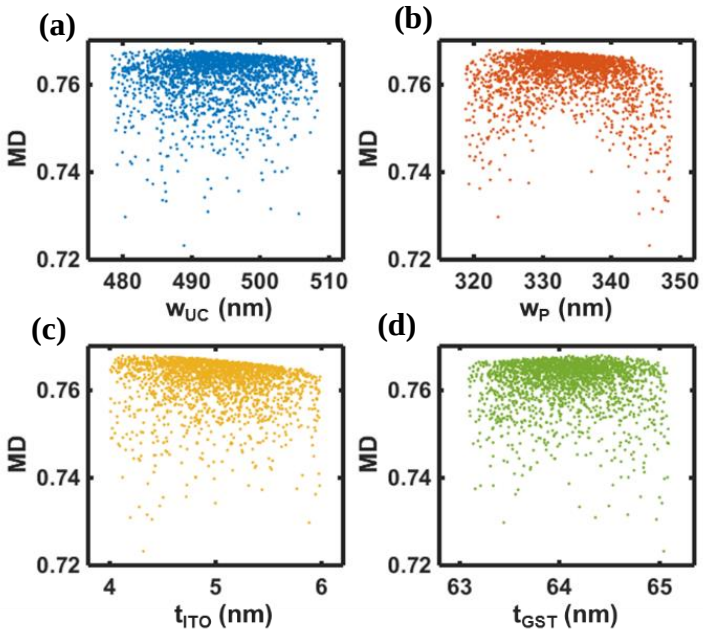

Figure 4.5. Scatter plot showing the variation of the phase-change metadevice modulation depth (MD) when typical manufacturing tolerances are included in the design and for the key parameters of **(a)** unit cell width w_{uc}, **(b)** width of top metal strips w_p, **(c)** thickness of the ITO layer, t_{ITO} and **(d)** thickness of the GST layer, t_{GST}.

4.4.2. Polarisation response and 3D modelling

In terms of the polarisation of the incident radiation, as pointed out at the beginning of the chapter, the patterning of the top metal layer into strips or squares will result in, respectively, a polarization dependent or independent operation (assuming normal

incidence). This is confirmed in **Figure 4.6**, where the performance of both types of modulators is compared, i.e. top layer patterned into (a) strips and (b) squares, for various incident polarizations.

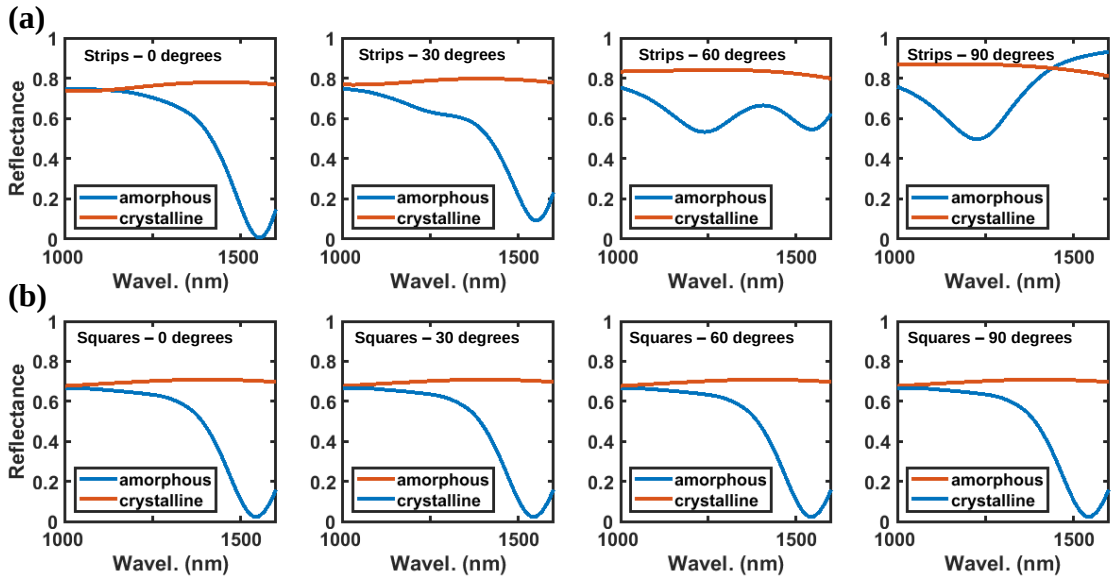

Figure 4.6. The reflectance spectrum of the modulator for different incident polarizations and with the top layer patterned into **(a)** strips (of the same width and spacing as in Figure 4.2) and **(b)** squares (with sides of length equal to the width of the strips in Figure 4.2). The polarization angles in each case are, going from left to right, 0 degrees (electric field perpendicular to the strips), 30 degrees, 60 degrees and 90 degrees (electric field parallel to strips). It is clear that in the case of the top metal layer patterned into squares the design is polarization independent (for normal incidence). In all cases red lines show results for the GST layer in the crystalline phase and blue the amorphous phase.

4.4.3. Non-normal incidence

In previous studies, devices similar to those of the previous section showed a very low sensitivity of the reflectance spectrum when the angle of incidence was changed [83,90,97,106]. Here we explore if this applies to our devices. Simulations were run for angles of incidence varying from 0 to 30 degrees in the 2D structure for TM polarisation, corresponding results are depicted in **Figure 4.7**. As it is expected the position of the minimum reflectance for the amorphous state remained unchanged with little distortion at 30 degrees incident angle. For the device containing crystalline phase-change material the level of reflection remains very high at the frequencies of interests with very little

deviation (mostly around the wavelengths around the resonance) when compared with the normal incidence case.

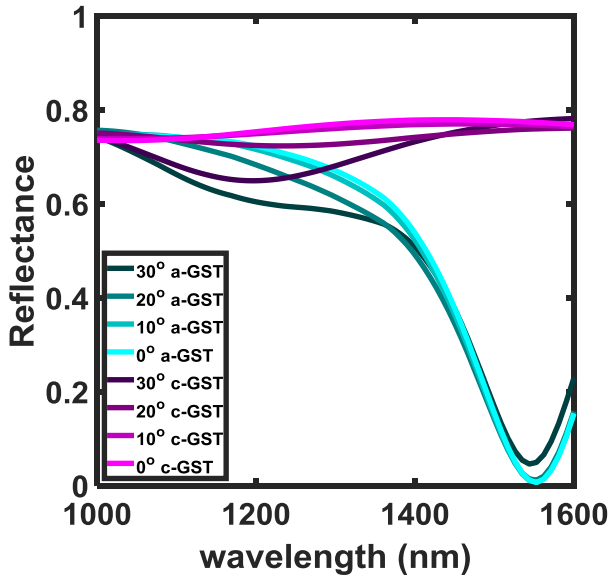

Figure 4.7. Calculated reflectance for different angles of incidence (0^o corresponds to normal incidence). Calculations are carried out for the same device as in Figure 4.2(a).

4.5. Experimental Results

4.5.1. Device fabrication

The fabrication of devices of the type discussed in previous sections can be considered to be divided in two parts. One part corresponding to the deposition of the bottom metal layer, and the dielectric spacer (GST and ITO) using magnetron sputtering, and the other part corresponding to the patterning of the top metal layer using electron beam lithography. Deeper details regarding the fabrication process can be found in section 3.2.

The first prototypes were here fabricated using aluminium for both top and bottom metal layers. These prototypes were fabricated with the main purpose of validating the optical performance predicted by the FEM models. Although it has been said that aluminium may not always be the best metal of choice in the phase-change based metamaterial devices, it is used here for three reasons: 1) it is a cheap material and available in our facilities; 2) it provides excellent optical performance; 3) there is no intention at this stage

to produce a 'final' device, the objective instead at this point being the checking of the reliability of the electromagnetic models to make accurate predictions. Therefore, a separate set of simulations were carried out to have the geometry to provide the optimum modulation depth (Equation (4.1)) using aluminium for both metal layers. Results of these simulations are plotted in **Figure 4.8(a)**.

4.5.2. Experimental validation of optical performance

The experimentally measured (using the purpose built optoelectronic probe station – see section 3.2.5) reflectance spectrum of the as-fabricated devices is shown in **Figure 4.8(b)**. It is possible to see how the reflectance measurements match very well with those obtained in the simulation.

The sample was annealed in a hot plate to crystallise the phase-change material. The temperature of the hot plate was set to 250 ^{o}C and the sample was annealed for 15 minutes.

Looking at the results of Figure 4.8, it is possible to conclude that the electromagnetic models produce predictions which can be relied upon. Any observed deviation from the modelled results can be attributed to not having exact optical constants for all materials used in the device or imperfections during fabrication such as roughness of the devices (this last issue will be further elaborated in the next chapter).

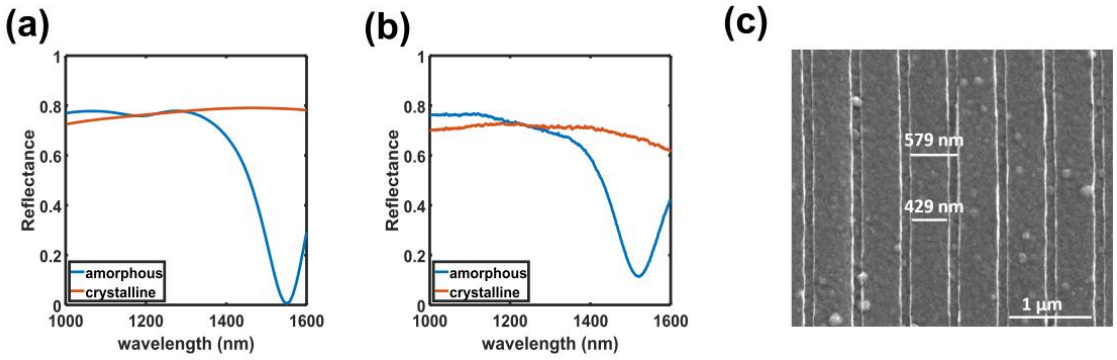

Figure 4.8. (a) Simulated response of the device to be fabricated. **(b)** Measured response of the fabricated device. **(c)** SEM image of the measured device. (Note that the refractive index and the extinction coefficient data for GST used to calculate the reflectance spectra in (a) is the same as the one used in ref. [60]).

SEM images were taken from the fabricated samples to check the correctness of the geometry of the top patterned metal layer. It is possible to observe a fair agreement between the target geometry and that actually obtained in fabricated devices, see **Figure 4.8(c)**.

4.5.3. Ex-situ optically induced switching

In this section, a preliminary study of the switchability of the (phase-change layer in the) device is presented. More specifically, the change of the device's response from as-deposited amorphous material to crystalline and back to amorphous is demonstrated. To do so, a scanning blue (405 nm wavelength) laser is focused on the surface of the device to raise the temperature and induce reversible changes in phase.

Reversible optically induced changes in phase-change films and metadevices have been previously demonstrated extensively in the literature (see e.g . [57,61,147,148]). In [57], for example, the switching of phase-change material that forms part of a meta-switch was carried out using laser spot size of 50 μm in diameter and nanosecond pulses. In [61] femtosecond laser pulses with sub-micron spot sizes were used to control the phase state of phase-change films for the provision of reconfigurable lenses. In [147] femtosecond laser pulses with 230-270 μm full half width maximum were employed to switch phase-change materials in nano-antenna structures. In [148], reversible optical switching of micron-sized regions of phase-change films was carried out using single nanosecond pulses (and revealed interesting phonon-polariton coupling effects).

In this thesis, a diode laser with a small spot (approximately 0.5 micrometres spot size) is used to scan the surface of the device, sending pulses with the required amplitude and duration to crystallise and reamorphise. Details of the parameters used in the experiment are compiled in **Table 4.2**. The employment of this simpler and cheap procedure to switch large areas (several micron in diameter) to optically induce cycles in the device is not, in general, reported elsewhere in the literature for plasmonic phase-change metasurface devices (that is metasurfaces formed by a metallic plasmonic structure combined with phase-change materials). After each scan (to crystallise or reamorphise) the reflectance of the device was measured, with results shown in **Figure 4.9(a)**. Optical microscope images were also taken after each scan to capture any visually perceivable changes

produced in the device, **Figure 4.9(b)**. Finally, SEM images were taken from the scanned area. Interestingly the SEM images revealed very little or non-existent damage in the area corresponding to the switched area of the device (covered by strips), but a moderate amount of damage on the area corresponding to the stack of layers (outside the device) was observed, see **Figure 4.9(c)**.

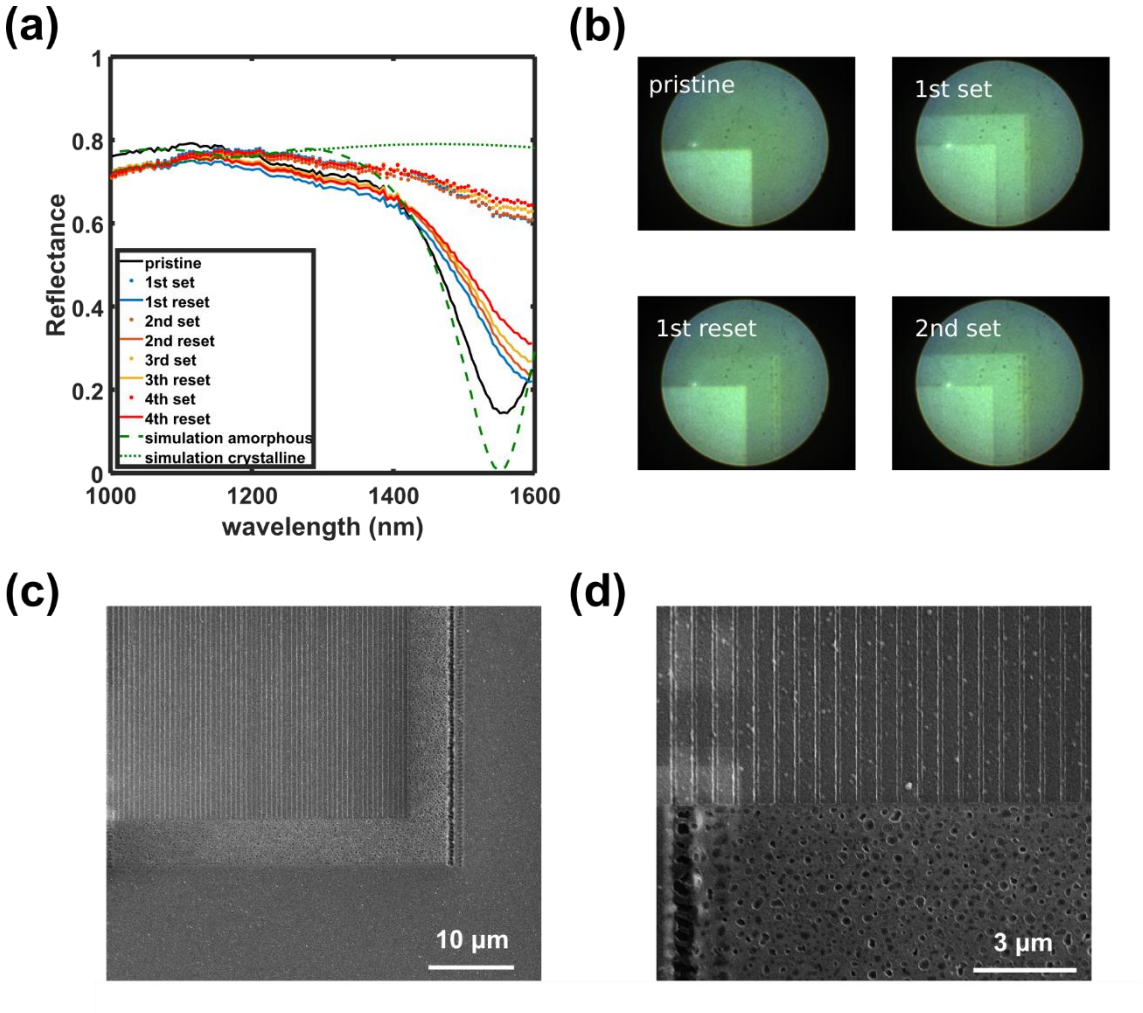

Figure 4.9. (a) Reflectance of the absorber device in the pristine state as well as after several cycles. **(b)** Optical microscope images taking after the crystallisation and reamorphisation laser scans. **(c)** and **(d)** SEM images of the switched device after the fourth reset.

The reflectance spectra (Figure 4.9(a)) indicate good re-crystallisation after cycling, but incomplete re-amorphisation on successive cycling. Incomplete re-amorphisation is not

unexpected when using a scanning laser since, as the laser scans, the periphery of the laser spot can heat previously amorphised regions of the phase-change layer up to temperature conducive to crystallisation. Other causes of the non-complete re-amorphisation could be not fast enough cooling rates after melting that lead to re-crystallisation. The difference in the reflectance between the reflectance spectrum correspondent to as-deposited amorphous phase and the rest of the reflectance spectra after a reset pulse may also be partially a result of differences in refractive index between the as-deposited amorphous GST and the melt-quenched amorphous phase [2].

Table 4.2. Parameters for re-crystallization and reamorphisation scans.

Parameter	**Crystallization**	**Reamorphization**
Rise and fall time (ns)	50	1
Pulse width (ns)	200	15
Time between pulses (s)	$1x10^{-5}$	0.01
Velocity of the scan (m s^{-1})	$5x10^{-5}$	$5x10^{-5}$
Power at the sample (W)	$3.6x10^{-3}$	$1.2x10^{-2}$
Fluence (mJ cm^{-2})	$4.2x10^{5}$	93

4.6. Summary

In this chapter, an exploration of the operation of phase-change metasurface devices specifically designed for absorber/modulation applications in the near-infrared part of the spectrum has been carried out. The performance of the device design in terms of selected relevant figures of merit (modulation depth and extinction ratio) has been optimised for the operation in the technologically important near-infrared regime of the electromagnetic spectrum. Furthermore, it has also been shown (from a design and simulation perspective) that a capping layer of ITO can be used to protect the phase-change material from oxidation while at the same time providing an electrical path for current, which is a very versatile arrangement to take into account for in-situ switching designs.

Phase-change and electro-thermal simulations were carried out in order to determine the suitability of the device for in-situ switchable operation. As well as this, the temperature

distributions that appeared in the device pointed to the top part of the device as the part that reaches the highest temperature. Therefore, metals with relatively high melting point are desirable for the metallic parts of the structure, especially for the top patterned metal layer.

Accounting for the fact that the top part of the device is the one that reaches the highest temperature, it was found that there exists a reasonable degree of freedom when choosing the material that comprises the top metal layer of the structure without compromising the optical performance. This fact allows us to choose typical electrode materials (such as W or TiN) for the top metallic part of the structure, as long as a metal with good plasmonic behaviour is placed in the bottom metal plane. This will greatly reduce the complexity of the design in Chapter 6 when the matter of in-situ switchability is addressed more in depth.

Other aspects of the performance of the phase-change metasurface device design have been explored, namely polarisation response, non-normal incidence and sensitivity to fabrication tolerances. For the polarisation response analysis, the effect that different polarisations have on the response of the device has been studied, finding (as in previous works [62]) that, for a polarisation independent device, a 2D grating is needed. The calculations using non-normal incidence also corroborates well with previous findings [83,90,97,106] about the extremely angle insensitive operation of the device. Finally, the sensitivity analysis has shown the relatively low perturbation that tolerances in the fabrication process causes over the optimised figures of merit.

Experimentally, first prototypes of the proposed device design have been fabricated with the objective of validating the electromagnetic models. A reasonably good agreement has been found between the response predicted by the FEM simulations and the measured response of the devices. Additionally, the switchability of the structure has been preliminary assessed by using a laser diode to deliver optical pulses and induce a number of reversible cycles in the structure.

All the studies contained in this chapter provide important and foundational information over the structure, materials and aspects of the performance that will be used in the rest of the thesis.

Chapter 5 Quality Factor Engineering

5.1. Introduction

As explained in Chapter 2, perfect absorbers can be utilized in a number of infrared device applications, for instance, radiation detectors [58,149,150], solar cells [151], spatial light modulators [56,152,153] and bio-sensing [154–157]. Various approaches have been used in the literature to design and explain the operation of perfect metamaterial absorbers, including analogies with plasmon slot waveguides [88,96], optical impedance matching [83,97], application of the first Kerker condition [98], critical coupling mechanisms [90,99] and considerations of the absorption cross-section of the resonators that comprise the metasurfaces [100]. All of these methods succeed in giving an explanation of the operation of perfect absorbers, however they differ significantly in terms of complexity and, importantly, their ability for quantitative design of the device response. Indeed, since the performance of metamaterial perfect absorbers can be broadly described by a few key parameters, namely the resonant frequency, bandwidth, quality factor and reflection coefficient (at resonance), a quantitative design methodology that predicts performance in these terms, in a simple and economical manner, is vital when trying to engineer device specifications that a certain application demands. For instance, in the field of infrared spectroscopy, perfect absorbers have been used to enhance the interaction of infrared radiation with biological analytes [154–156]. Here, by controlling the quality factor of the device, one can achieve a better analyte selectivity. Moreover, for increased sensitivity of detection, accurate control of the absorber's coupling to the incoming radiation is crucial [157]. To give another example, in the field of plasmonic colour printing, figures of merit such as the colour saturation are directly related to the quality factor of the resonant absorption spectra [100]. Finally, as a last example, of the importance of a quantitative methodology for designing the quality factor in optical devices, for instance in metal-insulator-metal structures used to create (optical) phase gradient metasurfaces with beam steering capabilities [60], control of the quality factor is important since it determines how sharply the optical phase varies around resonance. (The

requirement of a full 2π phase coverage is present only in overcoupled resonators) [99,158].

In this chapter, therefore, a design methodology is derived, based on eigenmode calculations together with the concept of critical coupling [90], that is not only relatively simple but which is also inherently well-suited to the quantitative design/selection of key absorber parameters including the resonant frequency, bandwidth and degree of coupling (minimum reflection at resonance). Moreover, the validity of the proposed methodology is demonstrated via the experimental fabrication and characterization of PCM-based reconfigurable absorbers working in the near infrared waveband (λ = 1550 nm) and with a purposely engineered quality factor. The fabricated devices have the same basic structure and materials as those shown in section 4.2. To reiterate, they are made with a nanostrip Al metasurface placed on top of a layered structure comprising a thin ITO film, a chalcogenide phase-change material $Ge_2Sb_2Te_5$ (GST) and a bottom Al mirror (see **Figure 5.1**) [102]. The ITO is used to prevent environmental oxidation of the GST layer, while it can be also utilized as a top electrode for electrical switching of the GST, see Chapter 4, Section 4.2.

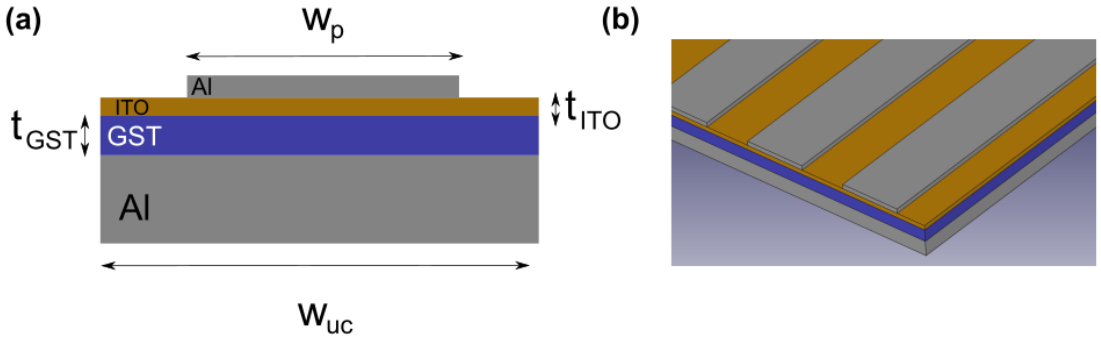

Figure 5.1. (a) 2D cross section of the unit cell of the reconfigurable phase-change absorber device. Dimensions that define the optical response of the device are shown, as well as the different material layers used. **(b)** 3D schematic of (part of) the device.

By transforming the GST between the amorphous and crystalline states our device can be operated in two distinctly different regimes. When the GST is in the amorphous state, the resonant gap plasmon [159,160] of the metal-dielectric-metal structure is excited and the

incoming radiation is absorbed (with the amount of absorption dependent on the degree of coupling). However, when the GST layer is switched into the crystalline state the resonance condition is lifted due to the change of the refractive index, resulting in specular reflection of the incoming radiation.

It is shown in this chapter how the absorber's resonance frequency can be accurately calculated for a structure composed of materials that present optical losses, using the result to obtain external and internal decay rates of the device [161]. These decay rates define the two most important parameters of a practical absorber - i.e. the quality factor and the reflection coefficient at resonance [158]. It is shown that the quality factor of our devices can be controlled, for a fixed operating frequency, by changing only one design parameter - the periodicity of the nanostrips comprising the optical metasurface - while leaving other design parameters intact. This allows us to produce simple guidelines for engineering absorbers with desired characteristics, without the need to run time-consuming finite element (FEM) simulations. The practicability of our modelling results is tested by fabricating several representative devices and measuring their optical reflectance spectra in amorphous and crystalline states.

Thus, the main outcomes of this chapter are:

- The creation of a design methodology that tackles the main aspects of the device performance: operative resonant frequency, bandwidth and minimum reflectance at resonance.
- Quality factor and geometrical parameters are quantitatively related using the developed method, resulting in simple guidelines for design and fabrication.
- Device fabrication and characterisation is successfully carried out in order to prove the validity of the method.

5.2. Theoretical preamble

In this section, some concepts and procedures are introduced in order to set the basis of the study carried out in this chapter.

It is convenient to start the discussion by stating that structures containing materials with a non-zero extinction coefficient do not have real eigenfrequencies (eigenfrequency $\notin \mathbb{R}$). Instead, the eigenfrequencies of the structure in this case are complex numbers. The imaginary part of the eigenfrequency is related to the dissipation of energy in the structure as it oscillates.

In the next subsections, a definition of the quality factor is given. Through relevant formulae, the relationship of the quality factor with the imaginary part of the complex eigenfrequency is revealed. Furthermore, a numerical technique that enables the finding of eigenmodes in structures with optically lossy materials is presented.

5.2.1. The quality factor: definition and generalities

In a resonator, the relationship of the dissipated power *P* and the energy of the system *U* is approximately linear [158], i.e.

$$P = -\frac{dU}{dt} = \alpha U \tag{5.1}$$

where α is a constant.

The rate of energy dissipation in the resonator α is proportional to the amount of the stored energy. Solving the above equation we obtain

$$U = U_0 e^{-\alpha t} \tag{5.2}$$

and by combining both of these equations we get

$$P = \alpha U_0 e^{-\alpha t} = P_0 e^{-t/\tau_{eng}} \tag{5.3}$$

where $\alpha = 1/\tau_{eng}$ with τ_{eng} being the time constant for the energy decay. The quality factor is defined as $Q = \omega_0 \tau_{eng}$. It thus follows that

$$P = \frac{U}{\tau_{eng}} = \frac{\omega_0 U}{Q} \tag{5.4}$$

The time constant for the amplitude decay is related to the time constant for the energy decay as $\tau = 2\tau_{eng}$ [158]. This means that the energy in the system decays twice as fast as the amplitude of the oscillation.

The quality factor Q can be related to the complex eigenfrequency of the system, $\omega_0 + i/\tau$, in the following way: $Q = \omega_0\tau/2$. The time constant for the decay rate is equal to the time necessary for the amplitude to decay by a factor of e^{-1}. The bigger the time constant of the amplitude decay, the lower the rate at which the energy is dissipated in the system and the higher the quality factor.

5.2.2. Eigenmode calculations

As pointed out by Bai et al. [161], it is possible to calculate the complex eigenfrequency of a resonant nanostructure (such as those examined here) in the presence of losses by searching for the complex frequency of excitation that makes the near-field diverge. Alternatively, one can search for a structure geometry that makes the electric field diverge at a specific complex frequency. The latter approach was adopted in this thesis, since it allowed the design of structures that resonate at a particular chosen (designed-in) frequency and which possess a given quality factor (since the complex eigenfrequency ω_0+i/τ of a resonating structure is related with the quality factor as $Q = \omega_0\tau/2$) [158]. Thus, a numerical implementation (carried out in COMSOL Multiphysics®) as described by Bai et. al. [161] is used for the eigenmode calculations, coupling this to optimization routines, built into the Global Optimisation Toolbox of Matlab®, to search for the device geometries (values of w_{uc}, w_p and t_{gst} in this case) required to deliver the desired quality factors.

In more detail, the model is excited with a complex frequency, but doing this in COMSOL Multiphysics® is not possible unless Faraday's and Amperes's Laws are transformed. Faraday's and Amperes's Laws in the differential form are recalled as

$$\nabla \times \mathbf{E} = -i\omega\mu(\omega, \mathbf{r})\mathbf{H} \tag{5.5}$$

$$\nabla \times \mathbf{H} = i\omega\varepsilon(\omega, \mathbf{r})\mathbf{E} + \mathbf{J} \tag{5.6}$$

Here, $\mathbf{E}$ and $\mathbf{H}$ are the electric and magnetic fields, $\mu(\omega, \mathbf{r})$ and $\varepsilon(\omega, \mathbf{r})$ are the magnetic permeability and electric permittivity respectively, ω is the wave frequency, $\mathbf{r}$ is the position vector, $\mathbf{J}$ is the induced conduction current density. By introducing the following

effective permittivities $\varepsilon_{eff} = \omega\varepsilon(\omega, \mathbf{r})/\omega_L$ and $\mu_{eff} = \omega\mu(\omega, \mathbf{r})/\omega_L$ with ω_L being a real number, Faraday's and Ampere's Laws can transformed into the following [161]

$$\nabla \times \mathbf{E} = -i\omega_L \mu_{eff}(\omega, \mathbf{r})\mathbf{H} \tag{5.7}$$

$$\nabla \times \mathbf{H} = i\omega_L \varepsilon_{eff}(\omega, \mathbf{r})\mathbf{E} + \mathbf{J} \tag{5.8}$$

The complex frequency ω that is used to excite the system is now hidden in the new effective optical constants (ε_{eff} and μ_{eff}). The frequency ω_L occupies the place of the usual frequency in the solver and it can be fixed to any value. To avoid computational errors it is advisable that ω_L is of same order of magnitude as the original frequency ω. Please, note that the described method is only a way to make COMSOL Multiphysics® accept complex eigenfrequencies as input for a frequency study. A more detailed discussion of the of the theory behind the interaction of light with leaky or dissipative resonators can be found in ref. [162].

Using the above described transformation one can calculate the complex eigenfrequency of a structure in the presence of losses by searching for the frequency that makes the near-field diverge. Alternatively, one can search for a structure that makes the electric field diverge for a desired complex frequency and hence possesses a given quality factor.

5.3. Quality factor engineering

Eigenmode calculations were used to optimize a number of device geometrical parameters so that phase-change absorbers, of the type shown in Figure 5.1, could be realized with various quality factors at the resonant wavelength of λ = 1550 nm. More specifically, the following device parameters - nanostrip resonator width, w_p, thickness of the GST layer, t_{gst}, and metasurface period, w_{uc}, - were swept using an optimization routine to achieve the required optical performance. The numerical technique introduced in the previous section 5.2.2 was used to excite the structure with a complex eigenfrequency. In essence, the method allows us to design a structure with a desired quality factor using the following steps:

1. Excite the device structure with a complex frequency, $\omega+i/\tau$, where $1/\tau$ is the decay rate associated with the amplitude of the oscillation for the loaded resonator (henceforth referred to as total decay rate). The real part of the excitation frequency ω is fixed while the imaginary part $1/\tau$ is varied in each simulation to achieve devices with desired quality factors.

2. Search for a device geometry (i.e. in this case, search for values of layer thicknesses, metasurface strip widths and periodicity) that causes the modulus of the electric field evaluated close to the resonator to diverge when excited with the chosen complex (resonance) frequency. This search is done using a global optimization algorithm.

3. Once the optimal structure is found, it is possible to relate the value of τ to the value of the quality factor as $Q = \omega_0\tau/2$ [158]. This means that in Step 1 the desired quality factor of the structure has been chosen, provided that it is possible to find an appropriate device geometry in Step 2 (see section 5.2.2 for further details about the quality factor and calculation of eigenmodes).

This results in significant gains in computational efficiency in the design of devices (as compared to conventional FEM simulations), since the model is essentially 'told' at which frequency the resonance is required using the real part of the desired eigenfrequency, and information about the bandwidth (quality factor) will be introduced in the imaginary part of the eigenfrequency. So, it is possible to directly target the resonant position and bandwidth of the device with far fewer calculations than in the case of a conventional design approach.

The method described in the previous paragraph is now applied to explore and extract conclusions of interest regarding the quality factor and the geometrical parameters of the device. Ten different absorber device designs (each design being a vector in the parametric space w_{uc}, w_p and t_{gst}) were obtained for values of the quality factor Q = 4, 4.5, 5, 5.5, 6. In **Figure 5.2(a)**, the resulting width of the nanostrip resonators w_p is plotted versus the thickness of the GST layer t_{gst} for all cases. It can be seen that all curves cross in a very small region of the graph around w_p = 451 nm and t_{gst} = 79.5 nm. This implies that for fixed values of w_p and t_{gst} (the crossing point in the plot) one can obtain any desired value of Q (within the range examined here) by varying only the width of the unit cell w_{uc}. To verify this, another set of simulations was carried out to again find structures

with Q = 4, 4.5, 5, 5.5, 6, but this time the values of w_p and t_{gst} were restricted to be within the narrow region where all the curves in Figure 5.2(a) cross (more specifically, for convergence purposes, this region was set to be 2 nm wide in the w_p direction and 1 nm wide in the t_{gst} direction). The results are shown in **Figure 5.2(b)** and confirm that the quality factor of the devices can be linked to only one geometrical parameter, namely the periodicity of the top plasmonic metasurface, w_{uc}. This is a key finding of the current work, showing how a "family" of absorbers having the same resonant frequency but different Q factors can be readily designed, and subsequently fabricated, using essentially the same device structure (apart from the value of w_{uc}).

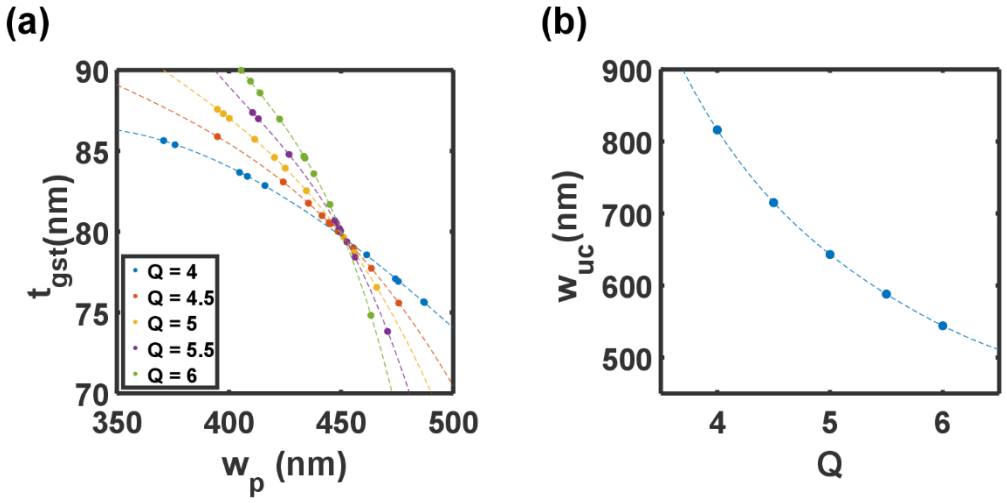

Figure 5.2. (a) Perfect phase-change absorbers of various geometries (w_{uc}, w_p and t_{gst}) optimized to possess desired quality factors (each colour indicates devices with equal values of Q). **(b)** Width of the unit cell w_{uc} plotted against the corresponding value of Q (the data in this plot corresponds to the optimized devices in the region where curves cross in (a) (w_p = 451 ± 1 nm and t_{GST} = 79.5 ± 0.5 nm)).

The maximum and minimum attainable values for the quality factor for the device structure of Figure 5.1 (with the restriction of fixed width of the nanostrips and thickness of GST) were found to be Q = 3.55 and Q = 6.26. For values of the quality factor smaller than 3.55 the periods in the structures start to be large enough (>1000 nm) to have higher diffractive orders within the range of measurement. For values of the quality factor bigger than 6.26 the width of the unit cell is too close to the width of the nanostrip, making the fabrication of these structures too difficult. Other kinds of restrictions not related to the geometry but to the optical constants of the materials used may also determine the limits of the range for the achievable quality factors. In particular, the internal losses will be

determined by the interaction of the excited resonant fields and the materials that comprise the device.

5.4. Reflectance calculations and experiments

A number of phase-change absorbers resonant at 1550 nm with a range of quality factors have been designed in the previous section using the presented eigenmode calculation approach. It is next shown, using 'conventional' FEM techniques [102] (see section 3.1.2 for details related to the reflectance calculations), what the expected reflectance spectra of the devices should be, over the wavelength range from 1000 to 1600 nm (note that 1600 nm is the longest wavelength examined since this corresponds to the maximum operating wavelength of the spectrophotometer used for experimental characterisation, see section 3.2.4 for details about the measurement of the reflectance of the devices). This will enable the observation of the change in the bandwidth and in the reflection coefficient at resonance for different quality factors.

Thus, in **Figure 5.3(a)-(c)** the simulated reflectance spectra are plotted for devices with Q = 4.5 (w_{uc} = 715 nm), Q = 5 (w_{uc} = 643 nm), and Q = 5.5 (w_{uc} = 588 nm). The optical constants for aluminium (Al) are extracted from the work of Rakic *et al.*[137] where the experimental data is fitted using the Brendel-Bormann model. The optical constants for indium tin oxide (ITO) were obtained by ellipsometry measurements. Finally, optical constants of GST are the same as in the work by Ruiz de Galarreta *et al.* [60].

Devices were also fabricated having the same (nominal) nanostrip periodicities, w_{uc}, as those in Figure 5.3(a)-(c), and their experimental reflectance spectra measured. The results are shown in **Figure 5.3(d)-(f)**. There is in general a very good agreement between the modelling and the experimental results. In the experimental reflectance spectra for the amorphous state, it is possible to observe a large absorption peak centred at 1550 nm, as expected from the calculated results. The simulation results also show an additional feature located between 1200 and 1400 nm wavelength. This additional weaker absorption feature is due to an additional resonant mode located at these frequencies and which is sensitive to the period as w_{uc} changes. This feature is also observable in the

experimental results, but more attenuated (due perhaps to additional optical losses in the experimental devices).

Finally, the reconfigurability of our phase-change absorbers is experimentally shown by switching the GST layer from the amorphous to crystalline state, here using controllable thermal heating on the hot plate. After switching, the resonant condition of the device is lifted, resulting in mirror-like specular reflection with efficiency here of above 60% (see Figure 5.3(d)-(f)). Therefore, the devices are indeed reconfigurable and could be used, for example as light modulators, here working in reflection and at 1550 nm wavelength.

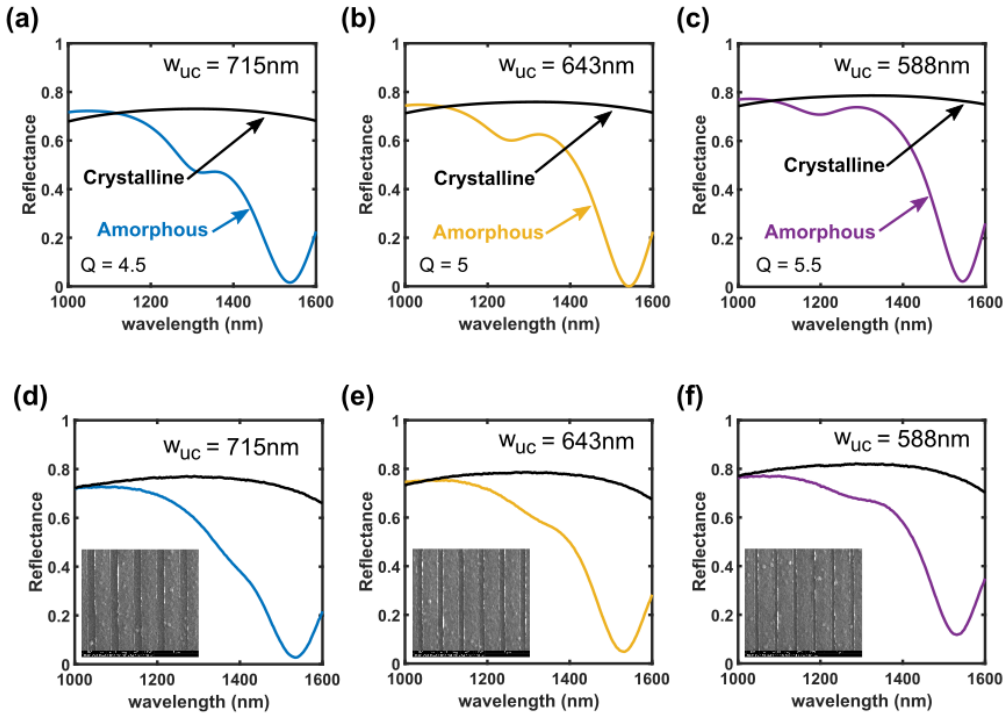

Figure 5.3. (a), **(b)**, **(c)** Simulated reflectance spectra for designs with fixed values of w_p and t_{gst} and with Q = 4.5, 5, 5.5 and with the GST layer in the amorphous (coloured lines) and crystalline (black lines) states. **(d)**, **(e)**, **(f)** Experimental reflectance spectra for fabricated devices with the same designs as in top panels (and again with the GST in amorphous and crystalline phases).

The dimensions of the fabricated devices were checked using scanning electron microscopy (SEM), with the results presented in **Figure 5.4**. One can see that the achieved periodicity and width of nanostrip resonators hardly deviates from the target values of w_{uc}

and w_p. The fabrication of the devices was carried out using the processes described in the previous chapter (section 4.5).

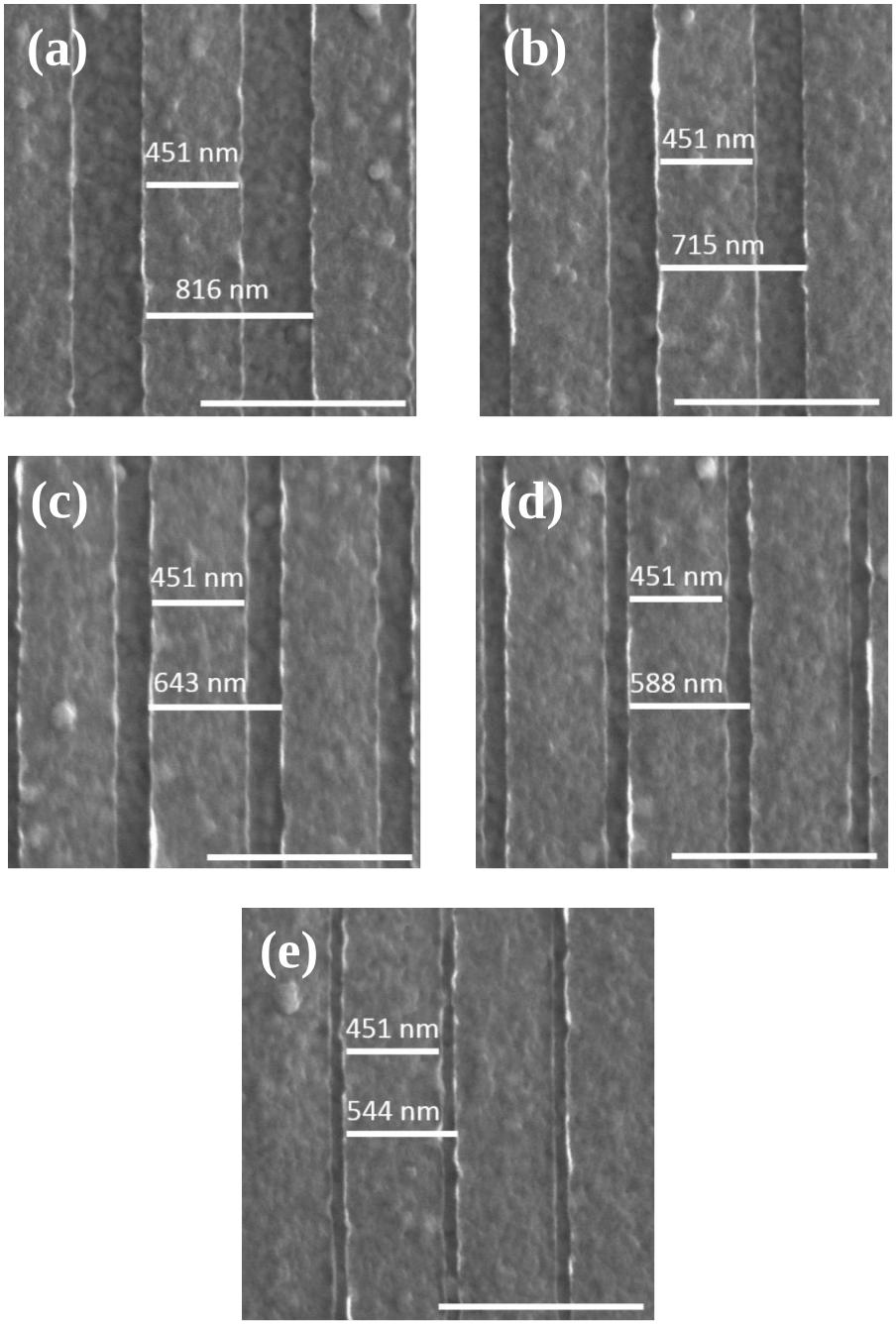

Figure 5.4. SEM images of the fabricated phase-change absorber devices. Values in the scale bars correspond to the target values obtained by modelling. **(a)** w_{uc} = 816 nm, **(b)** w_{uc} = 715 nm, **(c)** w_{uc} = 643 nm, **(d)** w_{uc} = 588 nm and **(e)** w_{uc} = 544 nm. Bottom scale bar in all figures is 1 μm.

5.5. Critically coupled absorbers

The eigenmode and reflectance calculations presented in the previous section allow for accurate extraction of the external and internal decay rates - important characteristics of a practical perfect absorber. The quality factor of a resonating structure, such as perfect absorber, can be expressed through its total decay rate as $Q = \omega_0\tau/2$, where ω_0 is the resonance frequency and $1/\tau$ is the total decay rate. In turn, the total decay rate $1/\tau$ is defined by the internal and external decay rates of the structure, according to the relation [158]

$$\frac{1}{\tau} = \frac{1}{\tau_0} + \frac{1}{\tau_e} \tag{5.9}$$

Here $1/\tau_0$ is the internal decay rate, i.e. the time measure of the internal losses of the resonator through electron scattering, and $1/\tau_e$ is the external decay rate, i.e. the time measure of the external losses of the resonator through the emission of radiation. The reflection coefficient $\Gamma(\omega)$ can be expressed in terms of the decay rates as [158]

$$\Gamma(\omega) = \frac{{}^{1}\!/_{\tau_e} - {}^{1}\!/_{\tau_0} - i(\omega - \omega_0)}{{}^{1}\!/_{\tau_e} + {}^{1}\!/_{\tau_0} + i(\omega - \omega_0)} \tag{5.10}$$

Thus, once the resonant frequency has been identified via eigenmode calculations, and the reflectance coefficient at resonance evaluated (via FEM simulations of the type used to generate Figure 5.3(a)-(c), but carried out only at ω_0), then Equation (5.9) and (5.10) can be solved simultaneously to obtain the values of $1/\tau_0$ and $1/\tau_e$ at ω_0.

The decay rates thus calculated for a set of perfect absorbers with fixed values of t_{gst} and w_p but with differing values of Q are plotted in **Figure 5.5(a)**. The interplay between internal and external decay rates determines the onset of critical coupling of the absorber to the incident radiation [99]. As is well known, the device is critically coupled when $1/\tau_0 = 1/\tau_e$ and in such a case all of the incoming radiation is perfectly absorbed at resonance. This condition implies matching of the free-space impedance to the impedance of the resonating structure. It can also be interpreted as the moment at which the absorption

cross-section is equal to the unit cell area [100]. According to the results shown in Figure 5.5(a), critical coupling should occur in the devices when Q = 5 (when w_{uc} = 643 nm). This is confirmed in **Figure 5.5(b)**, where the reflectance at resonance is shown for all Q values examined here; the reflectance is zero (perfect absorption) only for the case when Q = 5. Thus, although it is possible to easily obtain (i.e. to design) absorbers with a range of Q factors, this comes at a price of higher reflection at resonance (but the reflectance is still below 10 % at resonance for all the devices studied here).

It is also convenient to introduce another measure of the performance of the perfect absorber, namely the coupling coefficient $CC = \tau_0/\tau_e$, which is plotted in **Figure 5.5(c)**. Absorbers with $CC > 1$ ($\tau_0 > \tau_e$) are overcoupled, those with $CC < 1$ ($\tau_0 < \tau_e$) are undercoupled, while those with $CC = 1$ are critically coupled. The results of Figure 5.5(c) also demonstrate a clear correspondence between the degree of coupling and the quality factor, reiterating the point that it is not possible to design-in an arbitrary value of Q for any given degree of coupling (for fixed t_{gst} and w_p values, as used here).

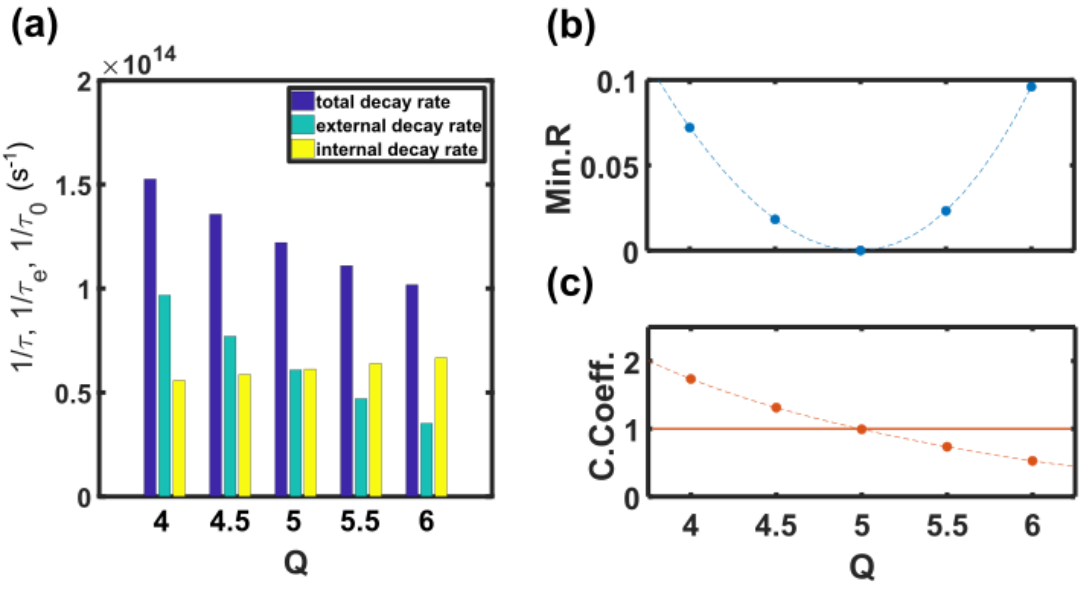

Figure 5.5. (a) Total, internal, and external decay rates as a function of Q. **(b)** Minimum reflectance and **(c)** coupling coefficient as a function of Q.

To explore in a little more detail the occurrence of critical coupling in the phase-change absorbers, five sets of devices are compared in **Figure 5.6** where FEM simulated and experimentally measured reflectance spectra are shown, having nanostrip periodicities

ranging from 544 to 816 nm. There is generally good agreement between the simulated (**Figure 5.6(a)**) and experimental (**Figure 5.6(b)**) results, apart from a mismatch in the minimum reflectance values.

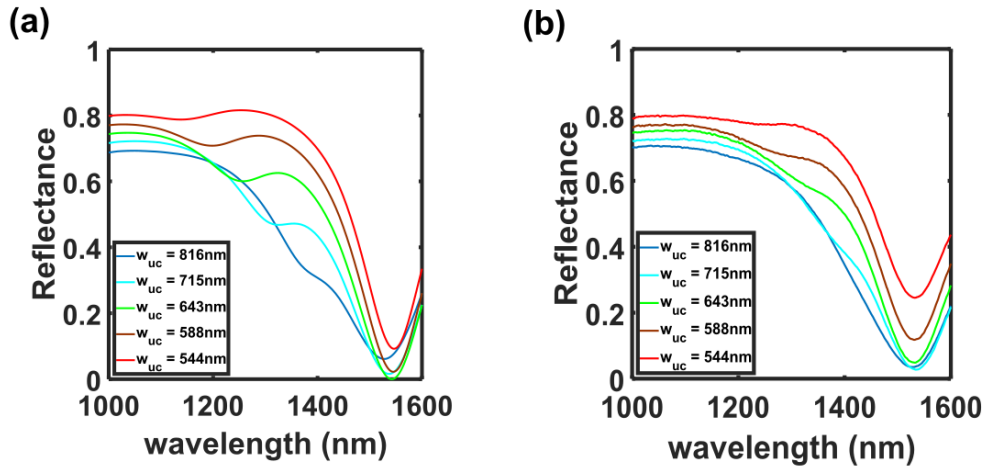

Figure 5.6. (a) Modelled reflectance spectra for a family of phase-change metamaterial absorbers (GST layer in the amorphous state) obtained by varying only the periodicity of the metasurface (the Al nanostrips). **(b)** Experimental reflectance spectra for fabricated devices having the same geometries as in (a).

In particular, it is noted that, according to the simulations, the absorber with a nanostrip periodicity of 643 nm (w_{uc} = 643 nm) should be the one which is critically coupled, while in the experimental results it is the device with w_{uc} = 715 nm which is closest to being critically coupled. This discrepancy can be explained by an internal decay rate that is larger in the fabricated devices as compared to that in the simulations. This most likely arises due to fabrication imperfections, in particular a non-negligible roughness of the surface of the Al film used to make the periodic nanostrips. The roughness of Al films is known to increase electronic scattering, so affecting their effective optical properties (n and k) and increasing losses and decreasing the quality factor [163,164]. Indeed, from Figure 5.5(a) it can be seen that if the internal losses were increased slightly (increased internal decay rate) then the absorber with Q = 4.5 (w_{uc} = 715 nm) would be (closest to being) at the critical coupling condition, while devices with higher Q values (w_{uc} < 715 nm) would possess a monotonically increasing reflectance at resonance. This is precisely

the behaviour seen in the experimental results of Figure 5.6(b). Thus, although the underestimation of the internal losses of our devices resulted in the mismatch between simulated and measured values of the minimum absorber reflectance, this does not affect general findings of this chapter.

5.6. "On-demand" quality factors

The above findings clearly show that by fixing two main design parameters of the proposed perfect absorbers – the GST layer thickness, t_{gst}, and width of the plasmonic strip resonators, w_p, - it is possible to control the quality factor and coupling coefficient of the device by changing only the resonator periodicity, w_{uc}. Thus, once optimal values of t_{gst} and w_p are found, the need to run conventional FEM simulations (that can be both time and computer power consuming) can be avoided. In fact, as it is shown below, it is possible to go further and produce simple guidelines that allow the design of perfect absorbers with specific 'on-demand' Q factors.

These simple guidelines are summarized and tested in **Figure 5.7**, specifically, the internal decay rate $1/\tau_0$ is observed to vary approximately linearly with the inverse of the width of the unit cell, w_{uc}, as shown in **Figure 5.7(a)**. In contrast, the external decay rate, $1/\tau_e$, increases linearly with w_{uc}, as can be seen from **Figure 5.7(b)**. Therefore, using Equation (5.9) and (5.10), it is possible to obtain a simple and quick way to calculate the Q value, for a given value of w_{uc}, via the relationship

$$\frac{1}{Q} = \frac{2}{\omega_0}\left(\frac{1}{\tau_0} + \frac{1}{\tau_e}\right) \tag{5.11}$$

where $1/\tau_0 = k_0/w_{uc} + C_0$ and k_0 $(= 1.761 \times 10^{16}\ nm\ s^{-1})$ and $C_0 (= 3.409 \times 10^{13}\ s^{-1})$ are the regression coefficients of the linear fitting in Figure 5.7(a), and $1/\tau_e = k_e w_{uc} + C_e$ where k_e $(= 2.261 \times 10^{11}\ nm\ s^{-1})$ and $C_e (= -8.612 \times 10^{13}\ s^{-1})$ are the regression coefficients of the linear fitting shown in Figure 5.7(b).

The results of applying Equation (5.11) to find Q for the cases with w_{uc} = 560, 600, 675, 775 nm are shown in Figure 5.7(c), where they are compared to Q values calculated via eigenmode simulations. It is clear that that there is excellent agreement between both

techniques. Thus, using eigenmode calculations and critical coupling concepts, it has been shown that it is possible to design perfect absorbers having a particular desired quality factor (at least over the range of Q values studied here), simply by changing the periodicity of the top plasmonic metasurface.

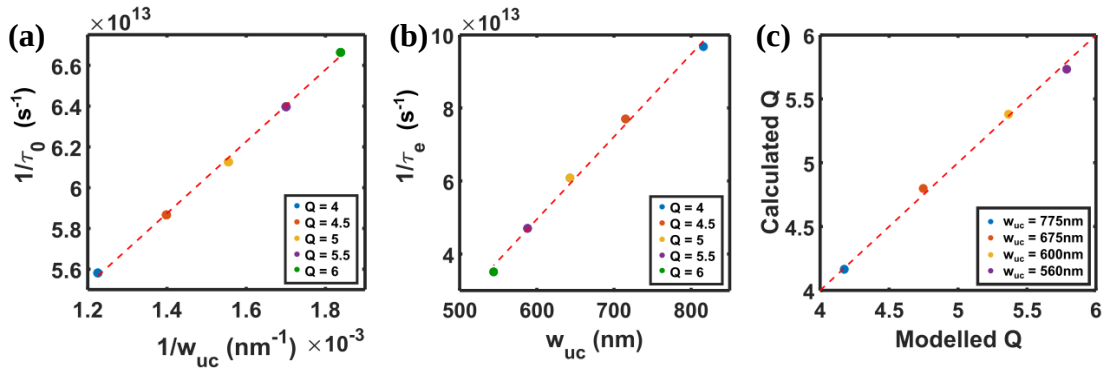

Figure 5.7. (a) Internal decay rate as a function of the inverse of the plasmonic metasurface periodicity w_{uc} (dashed line is a linear best-fit). **(b)** External decay rate as a function of the inverse of the plasmonic metasurface periodicity w_{uc} (dashed line is a linear best-fit). **(c)** Calculated values of Q using the data in (a) and (b) against the values for Q obtained from FEM modelling for the same structures (the dashed "45° line" is shown for visual guidance only).

5.7. Summary

In conclusion, a design method to control the main aspects that define the performance of perfect absorbers, i.e. the resonant frequency, bandwidth and reflection coefficient at resonance, has been presented. To validate the method, a family of reconfigurable phase-change perfect absorbers having desired quality factors was designed and fabricated, obtaining very good agreement between theory and experiment. Moreover, analysis based on a critical coupling approach allowed us to establish simple relationships between device geometry and performance. In particular, it has been shown how the width of the unit cell is (for fixed values of other device geometric parameters) linked directly to the value of Q. As a result, the design and fabrication process of the absorber devices was greatly simplified. This was demonstrated by producing a family of devices with a range of 'on-demand' quality factors, all operating at the same resonant frequency and able to

be fabricated simultaneously on the same chip (i.e., all with the same layer thicknesses and all with the same width of the top optical metasurface nanostrips). Furthermore, by changing the phase-change (GST) layer in the absorber structure between its amorphous and crystalline states, it was shown that the designed devices can be switched on and off, thus allowing for the design of active and reconfigurable components. The design approach is likely to find use wherever precise control over the resonant frequency and quality factor of plasmonic metasurface resonant absorbers type structures is desired.

Chapter 6 Electrically reconfigurable phase-change metadevices

6.1. Introduction

While it has been shown in this thesis (see Chapter 4) and by others [57,147] that ex-situ laser switching of the phase-change layer in reconfigurable metasurfaces is possible, a much more attractive approach for real-world applications is to use some form of in-situ, electrically-driven switching. By such means phase-change metasurfaces could be integrated with CMOS driving circuity, so providing a simple and effective route to true dynamic and reconfigurable operation. Of course the electrical switching of phase-change materials in non-volatile phase-change electrical memories is carried out without any notable difficulties [135,165], but in such cases the volumes (and areas) of phase-change material that has to be switched are small (of the order of thousands or tens of thousands of nm^3 in modern devices [165]), whereas in optical metasurfaces the volumes/areas that are required to be switched are very much larger (tens of millions of nm^3 for 'pixel' areas of the order of a square micron). Thus, it may be necessary/desirable to use alternative (to that used for phase-change memories) electrical switching approaches in the case of metasurfaces.

In this chapter therefore, with regards to the change of the optical response of the metasurfaces by electrical means, two approaches are discussed. The first is the 'direct' electrical switching approach that is utilised in phase-change memories. In this case, a voltage is applied across the two electrodes that sandwich a phase-change material layer, and the resulting current flow results in Joule heating. By applying voltage pulses of appropriate amplitude and duration (and fall-time), crystallisation and amorphisation of the phase-change layer can be induced. A particular attraction of this approach is that it allows structures such as crossbars to be built (see **Figure 6.1(a)**) which are much more convenient from the point of view of device integration and have already been

implemented for commercial electrical phase-change memories [15]. The direct electrical switching of large areas/volumes using a crossbar configuration is however problematic (as already mentioned above) but it may possible, as shown in section 4.3.2 to circumvent such limitations by appropriate design strategies.

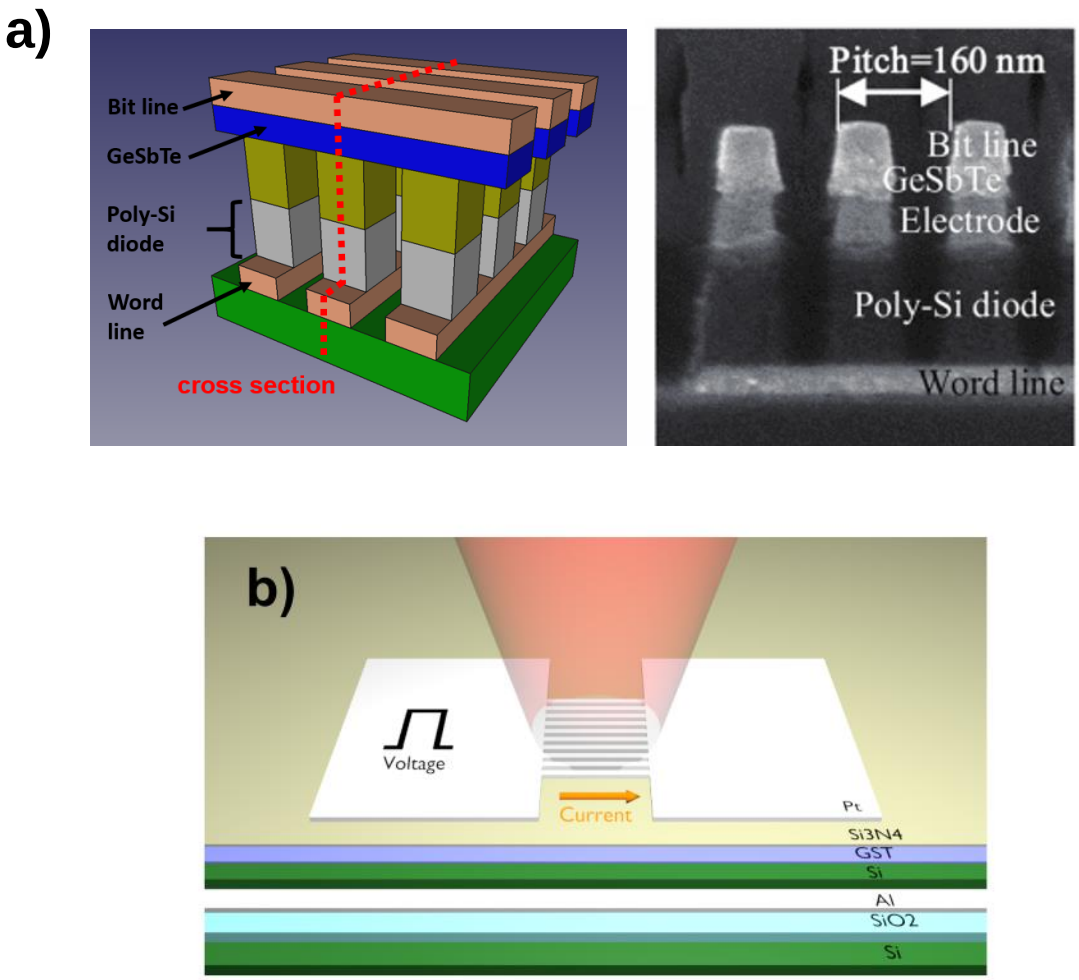

Figure 6.1. a) Schematic representation of a typical crossbar memory architecture (left) and device SEM micrograph of the cross section red dotted line (right) (Figure from [168]). **b)** Schematic of the structure used in this chapter for in-situ switching and in which the top patterned metal layer serves a dual role as (part of) the optical metasurface and electrically-driven microheater.

The second possible electrical switching approach is that using electrically-driven microheaters that are embedded/integrated into the phase-change metasurface in some

way. The use of embedded microheaters for the switching of relatively large areas/volumes of phase-change material has been demonstrated for phase-change RF switches [166,167] and for phase-change displays [25]. In such cases the microheater was invariably integrated into/beneath the bottom plane of the relevant devices. In this chapter, however, an alternative approach is used in which the top patterned metal layer plays the dual role of optical metasurface and microheater.

Figure 6.1(b), shows the configuration studied in this chapter for the combined metasurface/microheaters device approach. In this structure a difference in electric potential is applied along the strips in the top patterned metal layer. The current flowing through the strips will raise their temperature due to Joule heating, with subsequent heat conduction to the active (phase-change) layer, allowing the phase-change process (crystallisation and reamorphisation) to take place. One of the advantages of this approach is that heat is very uniformly delivered to the phase-change layer and, as a consequence, it is more suited to the switching of large areas/volumes than the direct vertical switching approach. Moreover, the basic metal-insulator-metal resonator structure used in the previous chapter is preserved, albeit with some modifications required to the materials used (for reasons that will become clear in the next section).

In summary, the main aims and outcomes of this chapter are to:

- Devise and discuss materials and methods suitable for in-situ electrically-driven switching of phase-change modulators in which the top patterned metal layer provides a form of integrated microheater.
- Experimentally fabricate and test the in-situ switching capabilities of such devices.
- Explore alternative structures for direct electrical switching in metasurface devices.
- Discuss how the crystallisation kinetics and thermal properties of the phase-change material itself can influence the in-situ switching capability of the devices.

6.2. Materials and methods for microheater switching of phase-change metasurface absorber/modulators

To utilise the top patterned metal layer in the metasurface absorber/modulator type device as a microheater, as depicted in Figure 6.1(b), requires correct simultaneous operation in the electromagnetic, thermal and electrical aspects of the device performance. There will thus most likely be tight constrains in the selection of materials that exhibit suitable properties in all these aspects of the operation of the device.

As well as the properties of the materials, there are other restrictions that come from the electrical driving system. For instance, many electrical power transfer systems (and indeed the measurement systems in research laboratories) are optimised for a 50 Ω load, so it is beneficial if the total microheater resistance is close to this value. In more in detail, the resistance of a strip of metal is:

$$R_{strip} = \rho \frac{L}{w \cdot t} \tag{6.1}$$

where ρ is the resistivity of the material used for the heaters, L is the length of the strips, w is the width of the strips and t is the thickness of the strip. Thus, if a number of strips N are connected in parallel as in Figure 6.1(b), the total resistance of the array would be:

$$R_{array} = \rho \frac{L}{N \cdot w \cdot t} \tag{6.2}$$

Since values of w and t are usually fixed to obtain a good optical performance, for R_{array} of 50 Ω, there will be a fixed aspect ratio for the active area (L/N), once the material, and hence ρ for the top metal layer is chosen. Therefore, even if Equation (6.2) apparently has a lot of degrees of freedom to design the structure, once R_{array}, w, t and ρ are fixed the aspect ratio L/N is fixed as well.

Another issue related to the structure shown in Figure 6.1(b) is the electrical insulation requirements between parts that act as resistors (heaters) and other metallic parts of the structure, so as to prevent electrical leakage. Any such leakage would cause the device to change its input impedance. Under these circumstances, the device will also be unmatched from the RF circuit used to deliver the switching pulse, resulting in poor coupling of the applied voltage pulses to the device.

Fortunately, it is possible to make use of previously obtained results to simplify the design of the structures. In section 4.3.3, it was found that the material for the top patterned metal layer could be fabricated from a different material to the bottom metal layer. In that way, it was possible to reach high levels of absorption and at the same time have freedom of choice for the material of the top patterned metal layer. This is going to greatly reduce the complexity in the design process when choosing an appropriate material for the heater.

The following materials were thus identified as good candidates to be used in the design of devices that use the top patterned metal layer to also provide in-situ switching via a microheater approach:

- **Platinum** is a good material for the top microheater implementation due to its chemical stability. The lack of oxidation is very convenient to have good electrical contacts with the probes. Another good property of platinum is its relatively high melting point (1768 ^{o}C, for the bulk, as compared to the aluminium used for example in Chapter 4 whose melting temperature is 660^{o}C). As well as this, Pt displays resistivity values that allow reasonable aspect ratios for the active areas of the devices. Moreover, the use of Pt for the top patterned metal layer does not adversely affect the optical performance of the metasurface, **Figure 6.2(a)**.
- **Silicon** is introduced into the dielectric space between the top and bottom metal layers (in addition to the GST layer) in order to allow for the reduction of the thickness of the GST layer, so facilitating switching. Silicon has a negligible extinction coefficient at the targeted frequencies of operation (C-band) and hence it behaves optically as a dielectric. Its refractive index is quite high and close to that of amorphous GST at the same frequencies. This makes the dielectric spacer very homogeneous in terms of optical properties. The high value of the refractive index is also advantageous because the electromagnetic mode is reduced in size and the resultant device will be more compact.
- **Silicon nitride** is introduced between the top patterned metal layer and the GST layer (replacing the ITO used in the structures of Chapter 4 and 5). This layer protects GST from oxidation and also acts as an electrical insulating layer to prevent current leakage to the bottom metal plane. There are two potential reasons of the leakage, first is dielectric breakdown of the silicon layer whose dielectric

strength is very small, the other reason is the increase of silicon electrical conductivity as it is heated up by the resistors.

- **Aluminium** is placed in the bottom metal plane to support the resonant mode when the phase-change material is in the amorphous state. Despite the melting point of aluminium being relatively low, it is placed at a safe distance from the heaters and it is well encapsulated.

Once the materials are chosen, the next step is to simulate the structure electromagnetically (see section 4.3.1 for details about electromagnetic modelling of reflection). In this simulation it is convenient to fix the thickness of the phase-change layer to values around 15 nm. This value for the thickness is a good compromise to observe an appreciable optical response while at the same time allowing for the rapid cooling of the GST layer that is required for successful amorphisation. A reduced amount of GST will lower the thermal resistance that the generated heat will 'see' when the structure is cooling down. It is expected that GST contributes strongly to this thermal resistance due to its relatively low thermal conductivity (the lowest of all materials in this particular structure).

For GST there is a variety of values reported in the literature of the cooling rate that allow the phase-change layer to quench from the melted phase. These values are typically at least 10 K/ns [69], although re-amorphisation in unexpected situations has been reported, such as when using 50 ns fall time pulses [169]. The geometry plays an important role in determining how fast the phase-change material cools down. In electrical phase-change memories the heat dissipation can be approximately considered to have spherical symmetry [77]. The heat being generated and dissipated in this geometry is extremely efficient in creating a hot spot and cooling it very fast. In the configuration for the metasurface devices under study here, the heat source has a large spatial extension and it is 2D (the heat source is approximately a surface). Furthermore, the heat is restricted to escaping towards the substrate in a hemisphere. These two geometrical factors reduce the rate at which heat can escape from the phase-change layer, hence making the geometry a most important to be considered.

Cooling rates will not only depend on the materials used and their position within the structure, but also on the shape and duration of the applied voltage pulse. The pulse used

for re-amorphisation has in general a short fall time, and the duration of the pulse is also important. A short pulse will heat mostly the phase-change material and will leave other areas of the device relatively cool, improving the cooling rates in the structure. This is because, for short pulses, heat has not enough time to diffuse to the surrounding parts of the device. This in turn will create a larger temperature gradient from the phase-change material to the surrounding volume of the device at the end of the applied pulse. As a consequence of that, the heat flow will be larger and the cooling rates will be faster for short pulses as compared to longer pulses (where the volume around the phase-change material will be at a higher temperature by the end of the pulse).

Simulation of the electrical aspects of the proposed structure is relatively straightforward using Equations (6.1) and (6.2). The electrical simulation in turn provides the volumetric heat source for the heat transfer simulation. Having the electrical conductivity of the material that forms the electrode, it is possible to calculate the geometry of the top patterned layer to have an active area suitable for measurement and also calculate the dissipated power that results from the combination of all the strips in the top patterned metal layer. Phase-change simulations using a Master Rate equation approach (see section 3.1.5) provide the final part of the overall model used to design microheater based devices and gain insights in their performance.

A sample of the information that can be extracted using the above simulation approach is presented in **Figure 6.2**. The simulation corresponds to a device with materials and structure shown in Figure 6.1(b). The thicknesses of the different layers starting from the substrate are 90 nm SiO_2, 80 nm Al, 76 nm Si, 15 nm GST and 15 nm Si_3N_4, see **Figure 2.1(a)**. An additional layer of Si_3N_4 of 15 nm was also introduced between the Al bottom plane and the Si layer (in the dielectric spacer), since this significantly improved the electrical robustness in terms of electrical insulation of the heaters (a single layer of Si_3N_4 between the phase-change material layer and the top electrode did not always prevent dielectric breakdown of the Si layer and subsequent change in impedance of the device). On top of the deposited stack of layers the top patterned metal layers comprise 5 nm of Ti adhesion layer and 25 nm of Pt.

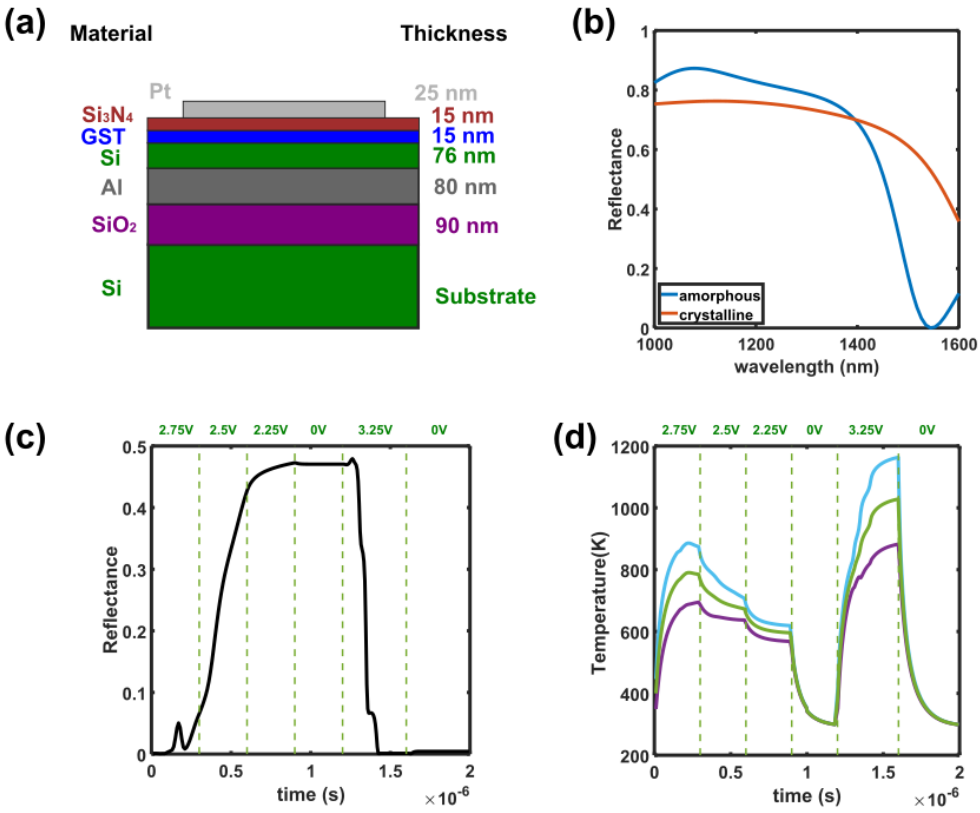

Figure 6.2. (a) Cross section of the unit cell of the simulated device showing thicknesses of the different layers and materials (the 5nm Ti adhesion layer between the top platinum layer and the Si3N4 layer is not represented). **(b)** Simulated reflectance of the absorber/modulator device (of the type shown in Figure 6.1(b)) for a fully amorphous and fully crystalline GST layer. **(c)** Reflectance of the device as a function of time for several applied voltage pulses. **(d)** Maximum (cyan line), minimum (green line) and average (purple line) temperature in the GST layer as a function of time for the set of applied pulses.

The first step in the design process is obtaining a 2D unit cell geometry that provides a good optical performance. The method employed in section 4.3 is used here again to obtain the optimum geometry. **Figure 6.2(b)**, shows a plot of the electromagnetic (optical) response of the resulting structure for the phase-change layer in the amorphous and crystalline states. **Figure 6.2(c)** shows a plot of the reflectance of the device at 1550 nm during the application of a sequence of voltage pulses having different amplitudes (shown in figure). Initially three consecutive pulses of 300 ns duration and reducing amplitudes are applied, and upon the application of each pulse the reflectance increases, indicating a progressive crystallisation of the device. After the application of the third pulse the voltage is set to zero for a period of 300 ns, then a high-amplitude (3.25 V),

short-duration (400 ns) pulse is applied, leading to a decrease in reflectance due to melting and re-amorphisation of the phase-change layer. Finally, **Figure 6.2(d)** shows a plot of the maximum, minimum and average temperatures in the phase-change layer for the same excitation sequence used in Figure 6.2(b).

6.3. Fabrication and characterisation of microheaters-type phase-change metasurface absorbers/modulators

Having designed and simulated structures suitable for the incorporation of microheaters into the top patterned layer of the phase-change metasurface absorber/modulator type device, it is possible to start the fabrication process. The fabrication of the structures starts with the selection of a Si/SiO_2 substrate with appropriate thickness of the SiO_2 top layer. SiO_2 has a very low thermal conductivity (1.3 $Wm^{-1}K^{-1}$) and one may think that reducing this layer to a minimum thickness is always convenient. However, reducing this layer too much (less than 50 nm) may result in a very large temperature gradient across the dielectric spacer and subsequently the phase-change material layer. This situation causes problems, such as very uneven crystallisation process, partial melting of the phase-change material layer, and temperature 'overshoot' of the top portion of the device. For this reason, it is advisable, in principle, to choose the SiO_2 layer to be between 50 and 90 nm thick.

After the selection of the substrate, a deposition of the designed stack of layers is carried out. The deposited stack of layers was, from bottom to top layer, $Al/Si/GST/Si_3N_4$. As already pointed out above, in some devices an additional electrical insulating thin layer was deposited between the Al and the Si layers to increase the robustness against electrical breakdown of the Si layer, leading to the following layer stack $Al/Si_3N_4/Si/GST/Si_3N_4$.

The top patterned metal layer is then fabricated on top of the deposited stack. A similar lithography process to that explained in section 3.3 is used here to obtain the PMMA mask before metallisation. In this case, the last step is the deposition of a 5 nm of Ti adhesion layer followed by the deposition of 25 nm of Pt. The device at this point is be ready to be measured.

Concerning intermediate measurement steps related to fabrication, a deposition of a platinum film of a similar thickness to the one employed for the microheater is carried out and the electrical conductivity was measured using a four point probe measurements technique. The device's active area was designed according to the measured value of the conductivity to produce a device of approximately 50 Ω total resistance. SEM measurements of the geometry of the microheater were also carried out to ensure sizes that match the design target, with an example image shown in **Figure 6.3(a)**.

Several devices were fabricated where the thickness of the phase-change layer was varied to explore the compromise between optical performance and switchability. The best performance experimentally was found for devices with a GST layer thickness of 25 nm, for which the measured optical response in the as-deposited amorphous state and in the electrically-switched crystalline state is shown in **Figure 6.3(b)**.

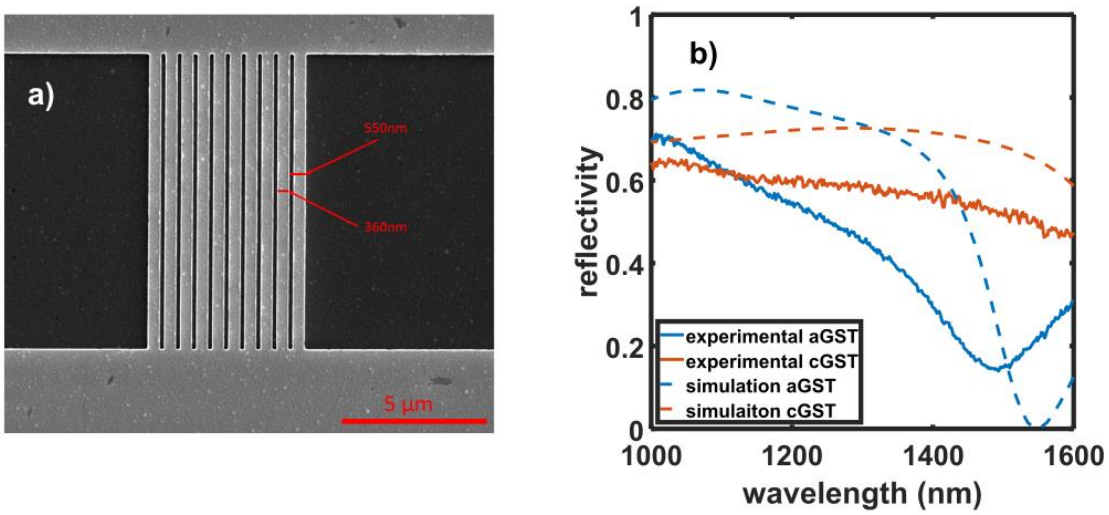

Figure 6.3. a) SEM image of the fabricated devices for in-situ switching. It is possible to appreciate the vertical strips in the centre that provide both the top patterned layer of the metasurface and provide the dual role of an integrated microheater. **b)** Measured reflectance spectra of a device of the type in a) with 25 nm of GST thickness. The reflectance spectrum is plotted for amorphous (as-deposited) GST (blue solid line) and after crystallisation (orange solid line). Simulated results are plotted along with the experimental results for comparison. The dashed blue and dashed orange lines correspond to the reflectance calculations for the phase-change material in the amorphous phase and crystalline phase respectively. Switching here used a trapezoidal pulse of 3V maximum held for 2 s and with a rise and fall time of 6 s.

It is clear from Figure 6.3(b) that successful crystallisation of the device (inferred from the change in optical response matching reasonably well that expected from electromagnetic simulations) using the in-situ microheater switching approach has been achieved. The measurement process used here started with a relatively long duration pulse of very low voltage, gradually increasing the voltage until an increase in reflectance was observed. When the reflectance value showed signs of saturation, the device was considered to be fully crystallised.

Although in-situ crystallisation of the absorber/modulator device is demonstrated by the results of Figure 6.3(b), a much more demanding task is re-amorphisation. To induce re-amorphisation, short duration pulses ranging from 50 ns to 100 ns (in some cases reaching 200 ns) with fall-times of 1 ns were delivered to a device in the fully crystallised state. The power of the pulses was gradually increased until changes in the optical reflectance (corresponding to signs of re-amorphisation) were observed.

Once the pulse conditions for both crystallisation re-amorphisation had been determined, devices were switched through multiple crystallisation/re-amorphisation cycles, demonstrating the potential of using the top patterned metal layer of the metasurface as a form of integrated microheater for in-situ switching. Example results are shown in **Figure 6.4**. In the top panel of this figure it is possible to see the voltage and duration of a sequence of electrical pulses applied to the device. Two classes of pulses can be observed: the amorphisation pulses, which are represented by a stem feature, and the crystallisation pulses, which are represented by a trapezoidal shape. The amorphisation pulses have 200 ns duration and an amplitude of 16 V, whereas the crystallisation pulses have 10 s rise/fall time and stay 2 s at maximum voltage level (which corresponds to 5.5 V in this case). In the bottom panel, the effect of the voltage pulses on the reflectance of the device at 1550 nm wavelength is represented as a function of time. A number of regular cycles between reflectance states is observed to take place in the device. In this case, the observed modulation depth is lower than seen in Figure 6.3, due possibly to only partial reamorphisation taking place in the device. Higher voltages were gradually employed in an attempt to increase the modulation depth, but this resulted in permanent damage to the device (such that it stopped working).

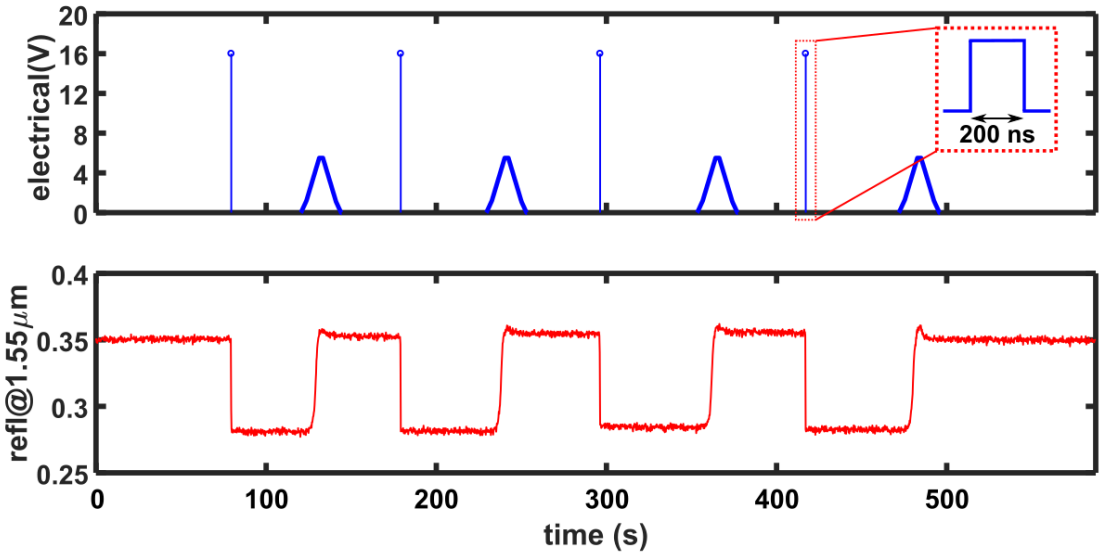

Figure 6.4. (top) Electrical excitation sequence applied to the microheater array for repeated switching cycles (crystallisation pulses have an amplitude of 5.5 V with 10 s rise/fall time and 2 s at maximum amplitude; whereas re-amorphisation pulses have an amplitude of 16 V and a duration of 200 ns with rise/fall time of 1 ns). (bottom) Variation in reflectance (at 1550 nm) of the device in response to the applied electrical excitations. The device tested in this experiment had a GST thickness of 23 nm.

6.4. Alternative approaches for electrically switchable phase-change absorber/modulators

In this section, a number of possible alternatives to improve the microheater approach for in-situ switching are studied. Two potential alternatives are considered, one based around the use of direct electrical switching, the other based around the use of phase-change material compositions more readily suited to in-situ switching.

6.4.1. Structures suited to direct electrical switching

Although successful in-situ switching using the microheater approach was demonstrated in the previous section, there are some potential drawbacks of this approach. The position of the microheaters, right on the top of the structure, may cause a temperature overshoot in the top layers of the structure, and in the heaters themselves. This will cause the temperature of the heaters to be substantially greater than in the phase-change material layer when it is melting. The consequence of this situation is a very small window for the employed voltages that would enable a reversible switching operation, bearing in mind

that the structure also has to cool at a very fast rate (to allow for amorphisation of the phase-change layer)

As has been pointed out, part of this problem comes from the fact the heat is restricted to escaping (approximately) in one direction (towards the substrate). As a result of this, heat is very efficiently accumulated, but cooling rates in the phase-change layer are as a result slower. The other problem is that the heater is external to the phase-change material, and so will always be at a higher temperature than it.

To solve these problems a structure with the following properties is proposed:

- The volume of phase-change material is changed from a layer of material to a confined cell of dimensions that are closer to the switched volume in a phase-change memory cell (0.1 μm^3 approximately for the designed device). This would increase the cooling rates to appropriate values to ensure reamorphisation of the cell. It also opens up the possibility for using a crossbar type structure (see Figure 6.1(a)).
- The structure will generate the heat necessary to switch the phase-change cell by passing an electrical pulse through the phase-change material volume (i.e. direct electrical switching). In that way, the heat source will be internal to the phase-change material, thereby avoiding overheating of other parts of the device.

More specifically, the structure proposed is schematically described in **Figure 6.5(a)**. The structure is a metal-insulator-metal structure. In this case, the structure is designed to maximise the optical absorption cross-section. Doing so, the electromagnetic fields are 'funnelled' into the metal-insulator-metal cavity [100]. If a phase-change material cluster is introduced in the cavity in a place where the resonant mode has a maximum of intensity, then the interaction of the phase-change material relative to its volume would be greatly increased. At the same time, the phase-change material volume can be shaped in a way to allow the current passing through it from the top electrode to the low electrode that would be the bottom metal plane.

As pointed out above, another aspect of interest is that since the structure is based on a vertical switching approach it is better suited for the integration as an array of pixels. The bottom metal plane is patterned in wide strips as the word line and a strip of ITO is placed on top of the metallic resonators as the bit line. This structure can be regarded as a more

advanced and developed version of the resonator designed in section 4.3.2, taking into account all the acquired experimental and modelling knowledge at the end of the thesis. The electromagnetic performance of the device is shown in **Figure 6.5(b)**, with strong absorption (at 1550 nm) with the GST in the amorphous phase and good reflection when crystalline.

Simple electrothermal simulations were carried out for the device. It was assumed that the GST cell was initially completely crystallised. A voltage pulse of 0.7 V and 20 ns was applied to the device. The estimated dissipated energy in the device was 4 pJ/μm^2 versus the 845 pJ/μm^2 estimated in the case of the microheater approach to reamorphise – a very significant reduction. As well as this, the obtained cooling rates are approximately 388 K/ns, which is well above the limit for the reamorphisation of the GST layer [69], see **Figure 6.5(c)** and **(d)**.

6.4.2. Alternative phase-change materials

So far in this thesis, the phase-change material employed has been $Ge_2Sb_2Te_5$. This material was chosen due to its extensive use in storage applications and hence a well reported set of properties (refractive index, electrical conductivity specific heat, thermal conductivity and density) in the literature. $Ge_2Sb_2Te_5$ is a material developed after an intensive search for materials with very high crystallisation rates. This property was of capital importance to compete in speed with other data storage technologies [2,3].

$Ge_2Sb_2Te_5$ is a nucleation dominated material which means that the part of the crystallisation process related to the crystal nuclei formation plays a dominant role in the crystallisation (or is relatively higher than in other phase-change materials). Higher rates for nucleation are located at approximately $0.6T_m$ (being T_m the melting point of the phase-change material) [170]. That means that at temperatures around 300 ºC the crystallisation process is quite active in $Ge_2Sb_2Te_5$. The consequence of these properties is a material that can crystallise fast enough at relatively low temperatures but has to be cooled very fast to reach temperatures below the interval where nucleation takes place to avoid recrystallization (i.e. enable re-amorphisation). As it has been said, this behaviour is very advantageous in applications where an extremely fast operation is needed, but

introduces very tight restrictions from the thermal point of view when used in other structures such as metasurfaces where high cooling rates are difficult to achieve.

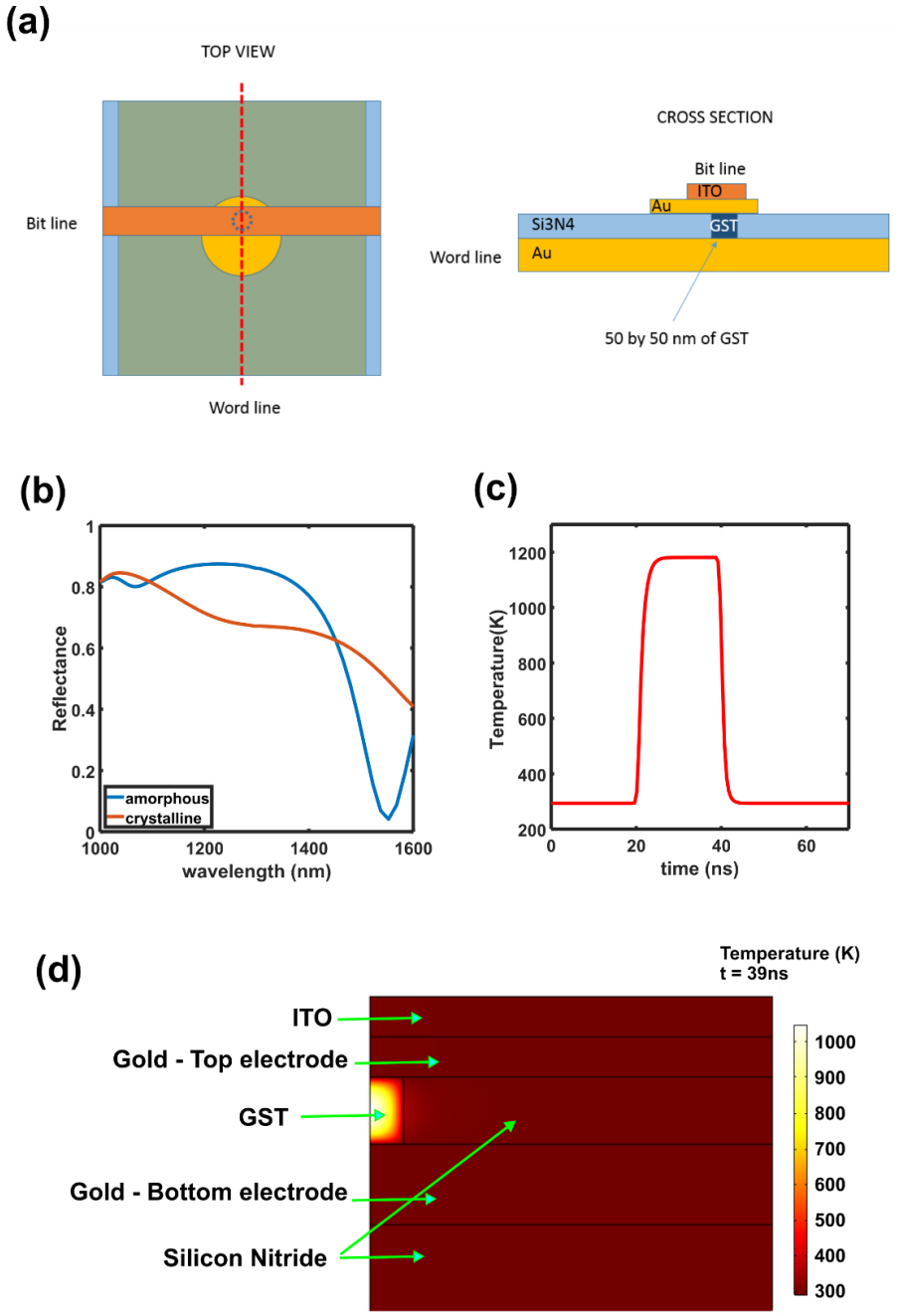

Figure 6.5. (a) Schematic view of the new structure proposed for a vertical direct electrical switching approach. (Left) top view of the device where the word and bit lines are visible. The dotted blue circle shows the position of the phase-change material cluster. (Right) Cross section of the device along the red dotted line in the figure on the left. **(b)** Reflectance spectra of the structure for fully amorphous and fully crystalline GST cluster. **(c)** Temperature evolution as a function of time for a rectangular pulse starting at t = 20 ns and finishing at t = 70 ns. **(d)** Temperature distribution in an axisymmetric simulation at the end of the applied pulse.

A possible solution to this problem would be to use a phase-change material whose crystallisation kinetics is different, so providing an advantageous solution for our thermal landscape. Of course there are numerous phase-change material compositions that might offer more suitable properties than GST, some explored and some not [171,172]. One obvious possibility is a growth-dominated phase-change material, such as $Ag_{5.5}In_{6.5}Sb_{59}Te_{29}$ (AIST) [173]. In growth dominated phase-change materials the nucleation process is not what dominates the crystallisation of the material, instead it is the rapid growth of the fewer formed nuclei at (typically) higher temperatures. AIST is a material that displays the described properties and hence it is considered to be a growth dominated phase-change material.

In the case of undercooled AIST, it was found that the majority of the activity of the material during crystallisation was concentrated at very high temperatures closer to the melting point as can be seen in **Figure 6.6**.

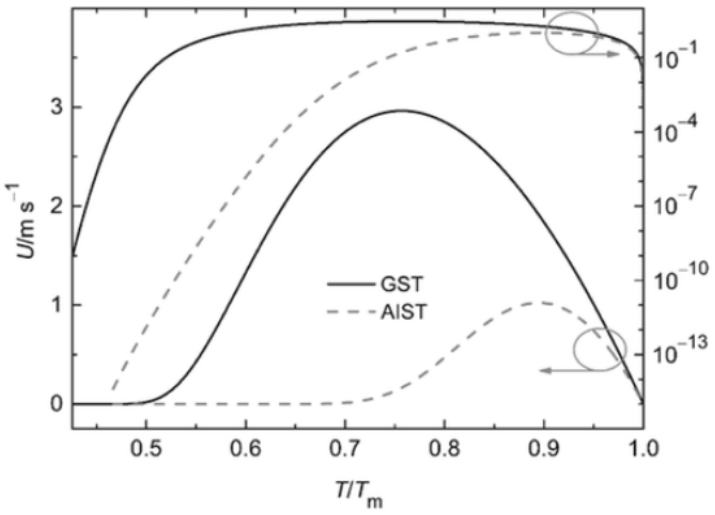

Figure 6.6. Figure showing the growth rate (U) of undercooled GST and AIST between the melting temperature T_m and the glass transition temperature T_g. The same growth rate U is represented in the right axis in a logarithmic scale. From this plot it is possible to observe that both peak values for growth are rather similar in value for GST and AIST, however the rate for GST is much higher than for AIST at lower temperatures. This, according to ref. [170], is due to a different dependence of viscosity with temperature for both alloys, with the viscosity of GST lower than the viscosity of AIST at temperatures below $0.7T_m$. This difference in viscosity also has an impact on the homogenous nucleation rate which has its maximum in both materials at $0.6T_m$ approximately, such that the nucleation rate for AIST is significantly lower (growth dominated) than for GST (nucleation dominated). Figure from extracted from ref. [170].

That means that the cooling rate necessary for quenching AIST into the glass state is potentially significantly lower than in the case of $Ge_2Sb_2Te_5$. Another parameter that is considered to give a good picture on how good a glass former is, i.e. how easy is for the material to form a glass after being melted, is the reduced glass transition temperature [174]. The reduced glass transition temperature is defined as the glass transition temperature divided by the melting temperature. The higher this parameter, the easier it is for the material to form a glass. On the contrary, the lower this parameter is the easier it is for the material to re-crystallise. This parameter by itself is not enough to completely characterise the process, but it is a good indication of the overall behaviour discussed here. For $Ge_2Sb_2Te_5$ the reduced glass transition temperature has been reported to be 0.42, while for AIST is 0.46 [175].

Moreover, the melting point of AIST (~810 K) is significantly lower than in the case of $Ge_2Sb_2Te_5$ (~900 K) [175]. This will have consequences not only from the point of view of energy consumption but also from the point of view of robustness of the device and the range of suitable metals that can be used for the top and bottom metal layers.

6.5. Summary

This chapter has been dedicated to the study of different methods and strategies to make possible the in-situ electrical switching of the phase-change metasurface absorber/modulator devices. Two main strategies have been presented, namely switching by means of microheaters and direct electrical switching.

The majority of the study has been dedicated to the electrical switching of the device using microheaters. First of all, a model was developed to have an understanding of what sort of response is to be expected from the designed devices in broad terms. The designed devices were fabricated, and successful repeated cycling between states was demonstrated. Moreover, the approach used in this chapter was quite novel in so much as the top patterned layer of the metal-insulator-metal structure was used for the microheaters, so providing a dual optical and in-situ switching functionality.

Finally, two alternative approaches have been suggested to continue the development of in-situ switching approaches suited to phase-change metasufaces. One is based in the use

of a vertical structure suited to direct electrical switching and that maximises the interaction of the phase-change element with the absorbed electromagnetic field. This approach allows a great reduction of the volume of the phase-change layer with a subsequent reduction of the consumed energy, along with huge increase of the cooling rates. On the other hand, the alternative approach based in the use of growth dominated phase-change materials (or materials with lower crystallisation rates) with low melting points would allow the design of structures that are not as demanding from the point of view of thermal operation and would facilitate a reliable operation.

Chapter 7 Metamaterial concepts applied to phase-change displays

7.1. Introduction

In this chapter, the capabilities of phase-change materials in combination with metamaterial structures for operation in the visible part of the electromagnetic spectrum are explored. The application towards which the work in this chapter is primarily oriented is non-volatile reflective display technology.

The idea of using phase-change materials to provide a form of non-volatile colour display was first put forward in 2014 by Hosseini et al. [23]. In that original work, colours were generated by a Fabry-Perot type cavity comprising a metal bottom layer, an ITO spacer layer, a phase-change material layer (GST) and a top ITO layer. By varying the thickness of the ITO spacer layer, and by switching the GST layer between its amorphous and crystalline phases, interference effects were used to produce a variety of colours. Later works by the same authors [25] showed how red, green and blue pixels could be produced using the same approach, so allowing for the generation of arbitrary colours via additive approach (i.e adding R, G, B colours).

In the present chapter, an alternative colour generation scheme is developed that uses absorption of incident light to generate colours via a subtractive approach. To accomplish this purpose, a structure very similar to the one presented in the previous chapter is used to generate cyan, magenta and yellow (CMY) pixels (thus forming the basis for subtractive colour production).

The main outcomes of this chapter are:

- The presentation of a new subtractive colour generation approach combining phase-change materials and metamaterials absorbers.

- The successful fabrication and characterization of designed devices.
- The creation of colour images in simulations and experiments.

7.2. Phase-change metamaterial display

7.2.1. Structure, materials and operation

As explained in section 2.3, optical metasurfaces have great potential to generate colour, and several different structures suited to this task have been suggested in the literature [100,108–115]. A common approach is to utilize metallic (or metal-dielectric) nanorods [100,111,112,115] or other lithographically patterned metal-dielectric nanostructures [109,113,114] that generate structural (i.e. non-colorant) colour using plasmonic effects. Such approaches are in general though 'fixed-by-design', meaning that colours and images are essentially written permanently into the metasurface by the specific nanostructure used. For display and electronic signage applications, however, the ability to change the displayed image or information in real time is required. Here, such a capability is provided by combining a metal-insulator-metal resonant absorber type optical metasurface [84,160] with a thin layer of chalcogenide phase-change material (PCM), so providing the key attributes of non-volatile colour generation and dynamic reconfigurability, the latter achieved by turning the metal-insulator-metal resonance 'on' and 'off' by switching the PCM-layer between its crystalline and amorphous states. Non-volatility is a particularly attractive feature of phase-change based displays, since no power is needed to retain an image once it is written into the phase-change layer/pixels [23–25,116]. As well as this, phase-change displays make use of ambient light (natural or artificial). This will have an impact in the energy consumption of the device as no power is necessary to retain the state of the device once it has been changed. Additionally, the images generated by the display would be brighter the higher the intensity of the incident light, instead of darker as is the case of active backlit displays. Many important applications such as mobiles, smart labelling, in-window displays, IoT devices, wearables, near-eye displays and even artificial retinas [23,116] could potentially benefit from the use of the described phase-change display.

The basic structure of our proposed phase-change material-based metal-insulator-metal metamaterial absorber is shown in **Figure 7.1(a)**. The absorber stack is composed of an aluminium bottom plane, a layer of GeTe, a layer of indium tin oxide (ITO) and a top aluminium layer patterned into circles. Aluminium is chosen for the metal layers due to its good plasmonic behaviour that extends down to visible wavelengths, as well as its ease of incorporation into standard semiconductor manufacturing processes [58,104,147] (though a potential drawback of Al is its relatively low melting point – see section 7.4 for a detailed discussion on this). The ITO layer provides environmental protection for the PCM layer (since chalcogenides readily oxidize in air [134]), while of course being transparent (necessary to sustain the absorber's resonant mode) due to its low absorption coefficient at visible wavelengths. GeTe is used here for the PCM (rather than GST) layer since it presents very interesting properties in the visible spectrum, properties that can be used to tune the response of metal-insulator-metal absorbers. Specifically, the negative value of the real part of the permittivity of GeTe in the crystalline phase indicates an optically metallic-like behaviour [72,73]. Such behaviour is used here to support and confine a resonant mode primarily in the ITO layer for a specific (user-defined) spectral band. As a result, the energy that corresponds to the wavelengths that fulfil the resonant condition will be absorbed. On the other hand, the optical constants of GeTe in the amorphous phase are more similar to those of a lossy dielectric; thus, when the GeTe layer is switched to the amorphous state, the absorber's resonant condition cannot be fulfilled, resulting in an essentially flat reflectance spectrum.

The structure of Figure 7.1(a) is thus ideally suited to the generation of subtractive colour: with the GeTe layer in the crystalline phase, the structure is designed (by proper choice of the resonator geometric parameters – see later) to absorb in the red, green and blue wavebands, so generating cyan, magenta and yellow pixels respectively; with the GeTe layer amorphous, the resonant absorption is switched off and a white-like reflectance should be obtained. By such means a full colour palette should be attainable using standard subtractive colour techniques [100,176,177].

The response of the metal-insulator-metal absorber of Figure 7.1(a) is controlled (designed) by the thickness of the ITO layer (t_{ito}), the width (diameter) of the top metallic resonator (w_p) and the width (w_{uc}) of the unit cell (i.e. the periodicity of the structure), see **Figure 7.1(b)**. The thickness of the aluminium bottom plane, the GeTe layer and the top

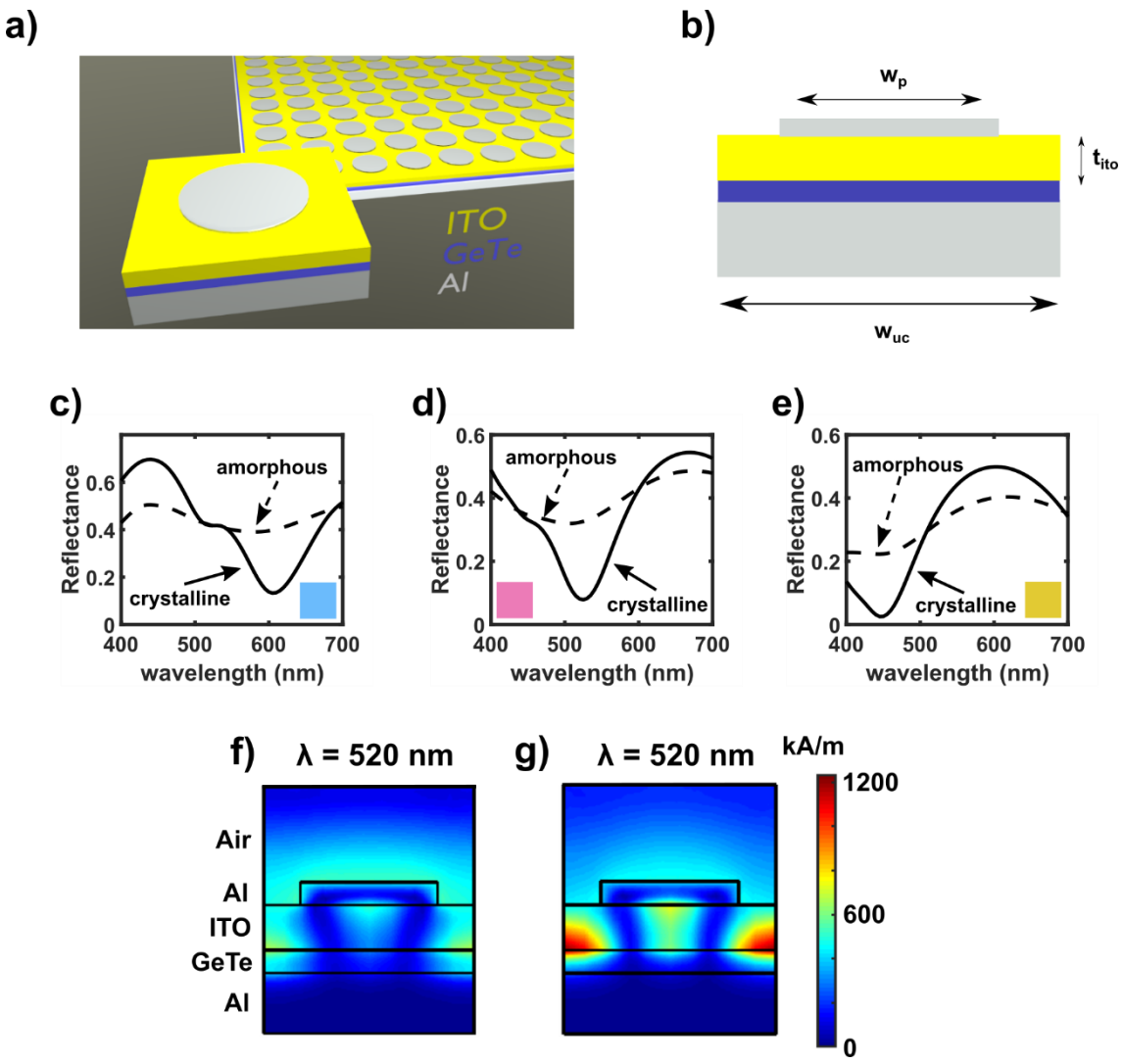

Figure 7.1. (a) 3D schematic of the phase-change metal-insulator-metal absorber structure and the materials used. **(b)** Cross sectional view of the structure with labelling of the geometrical parameters varied in the optimization of the devices. **(c)–(e)** Optimized reflectance spectra of the **(c)** cyan, **(d)** magenta and **(e)** yellow pixels, as obtained by FEM simulation. **(f)**, **(g)** Magnitude of the magnetic field (in the direction perpendicular to the plane) in the metal-insulator-metal absorber with the GeTe layer in the amorphous **(f)** and crystalline **(g)** phase.

metal layer are fixed in the presented approach, at 80 nm, 30 nm and 30 nm respectively: the bottom aluminium layer being chosen to be thick enough to prevent any radiation passing through the structure; the GeTe thickness being chosen thin enough to facilitate effective (electrical, thermal or optical) switching of the phase state, while being thick enough to present sufficient optical contrast between states; the top aluminium layer is thick enough to prevent significant deviation of the optical constants from those of the

bulk while at the same time is thin enough to provide a good lithographic process facilitating lift-off.

At resonance, a gap plasmon [160] is excited in the metal-insulator-metal absorber and currents in the top metal resonator are mirrored in the bottom metal plane, resulting in the excitation of a transversal magnetic resonant mode. This mode is, in this case, essentially a magnetic dipole below the top resonator and transversal to the polarization direction of the incident electric field (see section 2.2.1.1). If the structure is properly designed, the incident radiation can be perfectly coupled to the resonant mode, resulting in near-zero reflectance at the resonant wavelength/frequency, which is here is chosen to coincide with the centre of the RGB wavebands, so generating, at resonance, CMY pixels.

7.2.2. Design and optimisation

The workflow for designing the different pixels starts with a parametrization of the geometric distances that mainly determine the performance of the metal-insulator-metal device, i.e. t_{ITO}, w_p and w_{uc} (see Figure 7.1(b)). The reflectance spectra of the designed metal-insulator-metal structures are then calculated at visible wavelengths using finite element modelling (FEM) (as explained in section 3.1.2). An equal energy illuminant (E illuminant) is used, although any other illuminant profile could have been used (and the choice will depend on illumination conditions for which an optimal performance of the device is desired). Once an appropriate reflectance spectrum is achieved, colorimetric calculations are carried out to quantify the performance of the device in terms of colour production.

In particular, the tristimulus values *X*, *Y* and *Z* are calculated using the following formulae [178]:

$$X = \frac{K}{N}\int_{380}^{780} I(\lambda)R(\lambda)\bar{x}(\lambda)d\lambda \tag{7.1}$$

$$Y = \frac{K}{N}\int_{380}^{780} I(\lambda)R(\lambda)\bar{y}(\lambda)d\lambda \tag{7.2}$$

$$Z = \frac{K}{N}\int_{380}^{780} I(\lambda)R(\lambda)\bar{z}(\lambda)d\lambda \tag{7.3}$$

where $R(\lambda)$ is the reflectance of the device as a function of the wavelength, $I(\lambda)$ is the illuminant, K is a scaling factor (unity in this case), $\bar{x}(\lambda)$, $\bar{y}(\lambda)$and $\bar{z}(\lambda)$ are the CIE (Commission Internationale de l'Eclairage) standard observer colour matching functions and N is given by

$$N = \int_{380}^{780} I(\lambda)\bar{y}(\lambda)d\lambda \tag{7.4}$$

Finally, to obtain the x and y coordinates in the CIE 1931 chromaticity diagram [179] it is necessary to perform the following normalization:

$$x = \frac{X}{X+Y+Z} \tag{7.5}$$

$$y = \frac{Y}{X+Y+Z} \tag{7.6}$$

Once a geometrical representation of the reflectance spectra (with the GeTe layer both crystalline and amorphous) has been obtained (as points on the standard CIE 1931 chromaticity diagram), a further optimization algorithm is run on the structure that minimizes the distance between these points and those for 'ideal' CMY pixels (the latter chosen according to the "Specifications for Web Offset Publications" [180]. A pattern search algorithm is used for this, in the Global Optimization Toolbox in Matlab®, to find the optimum geometry that makes the points corresponding to the calculated spectra to be as close as possible to their respective chosen objectives.

The values for the permittivity used in the electromagnetic calculations for aluminium are extracted from the work of Rakic et al. [181] where a Brendel-Bormann model is used to extract the optical constants of several metals. The optical constants of ITO have been obtained through ellipsometry measurements carried out by ourselves. And finally, the optical constants for GeTe have been extracted from the work of Shportko et al. [141] where the optical constants of several chalcogenide phase-change materials have been compiled.

Following the above approach, the calculated reflectance spectra corresponding to the optimal phase-change metal-insulator-metal absorber structure for cyan, magenta and yellow pixels are shown in **Figure 7.1(c)**, **(d)** and **(e)** respectively. It can be seen that these reflectances are indeed characterized by a strong absorption in the red, green and blue when the GeTe layer is crystalline, and a nearly flat response when the GeTe layer is amorphous. Earlier, this resonant behaviour and the subsequent absorption (with the GeTe in the crystalline state) was attributed to a better confinement of the resonant mode in the ITO layer. This is indeed the case, as can be seen in **Figure 7.1(f)** and **(g)** where the distribution of the modulus of the magnetic field (perpendicular to the plane of the paper) is shown for the magenta pixel at 520 nm excitation wavelength and with the GeTe layer amorphous (Figure 7.1(f)) and crystalline (Figure 7.1(g)). The field amplitudes are much higher when GeTe is crystalline, and the effective confinement of the field to the ITO layer is clear. This is precisely what it is expected following the discussion in the previous sections on the operation of the metal-insulator-metal structure and the optical constants of GeTe. Note that the device dimensions yielding the CMY responses of Figure 7.1 are given in **Table 7.1**.

Table 7.1. Geometrical parameters for the optimized phase-change metal-insulator-metal type cyan, magenta and yellow pixels (obtained from the colorimetric optimisation).

Pixel type	**w_{uc} (nm)**	**w_p (nm)**	**t_{ito} (nm)**
Cyan	329	214	84
Magenta	278	181	60
Yellow	240	156	37

7.2.3. Fabrication and characterization of the CMY pixels

Having successfully designed and simulated suitable CMY pixels using the phase-change metal-insulator-metal absorber approach, their experimental realization is now reported. The requisite structures for each pixel colour were fabricated using magnetron sputtering to deposit the stack of layers (i.e. the Al, GeTe and ITO layers) on a Si/SiO_2 substrate, followed by electron beam lithography to define the top resonator pattern (carried out using a PMMA mask followed by sputter deposition of the top Al layer and lift-off). The fabrication process is essentially the same as that followed to fabricate the previous metal-insulator-metal structures reported in section 3.3.

Scanning electron microscope (SEM) images of the as-fabricated structures are shown for each pixel colour in **Figure 7.2(a)-(c)** along with the actual colours generated by the experimental pixels with the GeTe layer in the amorphous and crystalline phases (inset). Figure 7.2(a)-(c) reveals that the target dimensions of the top resonator pattern (as in Table 7.1) match very closely those actually achieved. Moreover, with GeTe in the crystalline phase the desired CMY colours are produced and, with the GeTe amorphous, a more white-like response is obtained. A more quantitative evaluation of the colours produced can however be obtained by measurement of the reflectance spectra and by mapping to the standard CIE colour diagram, both of which are reported below.

The reflectance spectra of the as-fabricated phase-change metal-insulator-metal structures were measured according to the procedures explained in sections 3.2.4 and 3.2.5. Once the data corresponding to the as-deposited amorphous phase of the GeTe was obtained, the GeTe was crystallized by heating to 250 ^{o}C for 15 minutes and the spectra re-measured. The results are shown in **Figure 7.2(d)-(f)** and show the expected preferential absorption (with GeTe crystalline) in the RGB wavebands for the CMY pixels respectively. These measured spectra were then mapped to the CIE 1931 chromaticity diagram, as shown in **Figure 7.2(g)** (where, for comparison purposes, it is also shown, inset, the mapping of the colours simulated via FEM). A good performance for the experimental cyan and magenta pixels when compared with the simulated behaviour is observed. However, when the metal-insulator-metal absorption peak moves to blue wavelengths (~420 nm), so producing a yellow colour, the agreement between the experimental and simulated pixels is not so strong. This is most likely due to the fact that the blue metal-insulator-metal absorber has the smallest feature sizes and so

imperfections in the fabrication process (e.g. film roughness) have a greater influence on performance.

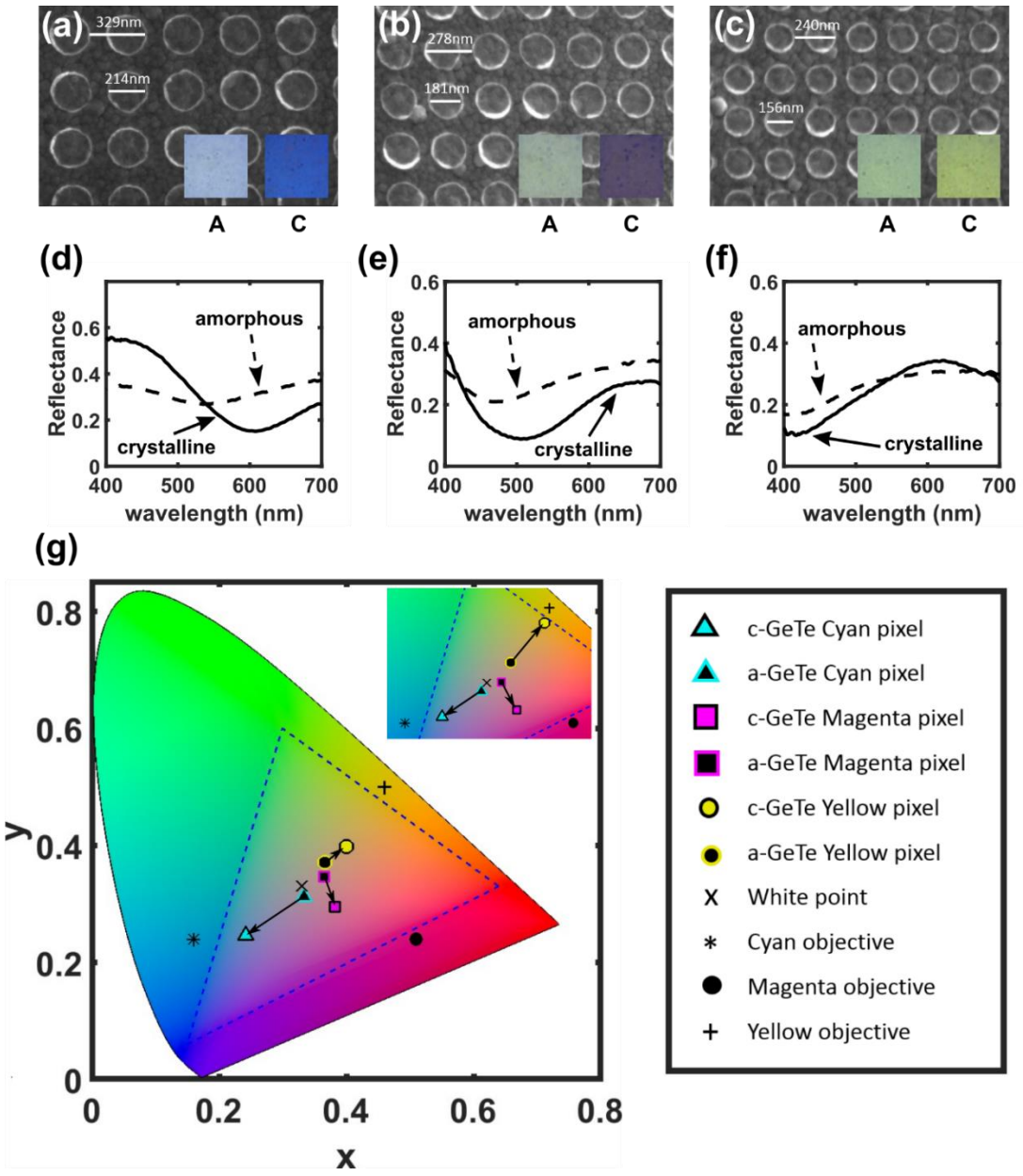

Figure 7.2. SEM images of the as-fabricated phase-change metal-insulator-metal **(a)** cyan, **(b)** magenta and **(c)** yellow pixel structures. The insets are optical microscope images that clearly show the colours generated with the GeTe layer in both the amorphous (left) and crystalline (right) states. **(d)**, **(e)** and **(f)** show experimental reflectance spectra for the cyan, magenta and yellow pixels respectively. **(g)** Representation of the spectra in **(d)**, **(e)** and **(f)** in the CIE 1931 chromaticity space (inset shows the mapping of the FEM simulated pixel responses of Fig. 3). Also shown are additional aspects of interest, such as colour objective points, with the relevant legend adjacent to the CIE 1931 diagram.

Such imperfections, as well as uncertainties in the optical constants of the various layers used in the devices, are most likely the cause of differences seen in the simulated (Figure 7.1) and experimental (Figure 7.2) reflectance spectra. A closer correlation between the simulated (i.e. designed) performance and that achieved experimentally is thus expected for tightly-characterized films and optimized deposition conditions (e.g. to reduce roughness).

7.3. Creation of images

In this section, the ability of the designed structures to display image information is studied. The section is divided in two main parts. The first part explains the procedure followed in order to simulate colour appearance from reflectance spectra. The second part is dedicated to the simulation of selected images (using calculated and experimentally measured spectra) and the experimental creation of images using a scanning laser to crystallise selected parts of the device.

7.3.1. Photometric and colorimetric calculations (colour appearance)

To translate simulated and measured reflectance spectra of devices into perceived colour the following steps were carried out:

1- Obtain tristimulus information from the spectral information using equations (7.1), (7.2), (7.3) and (7.4) in section 7.2.2.

2- Convert tristimulus XYZ to sRGB colour space coordinates values using the function *xyz2rgb*() in Matlab (this transformation is done for the E illuminant).

3- Set the correct illumination levels (which are here assumed to correspond to illumination levels lying between those in a normal office and outside on an overcast day).

For cases in which the GeTe layer is assumed to be partially crystallized, the first step towards having a multilevel representation is to determine the tristimulus values XYZ for the spectra of the GeTe layer in the fully crystalline and fully amorphous states. These XYZ values are then transformed to sRGB coordinates using the function *xyz2rgb()* in Matlab. If $RGBcr$ are the coordinates of the reflectance spectra for the crystalline state and $RGBam$ are the coordinates for the reflectance in the amorphous state, a vector is formed using the expression $RGBcr - RGBam$. A scale of desired intermediate values for colours is then formed following the formula $RGBam + f * (RGBcr - RGBam)$ where f is contained in the interval [0,1].

The CMY pixels developed here can be combined in various ways to extend the range of colours obtainable (i.e. extend the colour palette). One simple approach is to place the pixels side-by-side such that the perceived colour is a type of average of that of the individual pixels. For example, **Figure 7.3** shows such a side-by-side arrangement of C and M pixels. Colour information for fully crystalline cyan and magenta pixels was taken and the pixels were arranged as in a chessboard type pattern. A close-up image (**Figure 7.3(a)**) can distinguish the individual pixels. **Figure 7.3(b)** is zoomed out until the individual pixels are barely distinguishable. Finally, in **Figure 7.3(c)**, the perceived colour of the side-by-side chessboard arrangement of the C and M pixels is shown, as calculated using the methods described in at the beginning of this section.

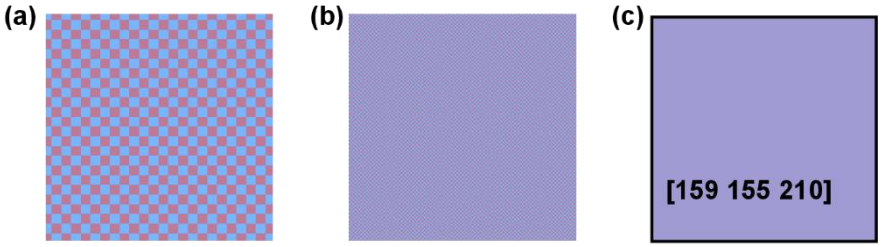

Figure 7.3. **(a)** Close-up of a side-by-side arrangement of crystalline C and M pixels (colours extracted from measured spectra). **(b)** Zoomed out image of the pixels in (a) where colours from individual pixels start to merge. **(c)** Colour resulting from side-by-side chessboard arrangement of C and M pixels, as calculated using the procedure outlined in this section (inset: calculated sRGB coordinates of the final colour).

7.3.2. Simulated and experimentally produced images

The attention is now turned to the generation of display information and images using the phase-change metal-insulator-metal pixels designed and fabricated above. For fixed displays, such as permanent or semi-permanent signage/advertising/notifications, the vivid colour differences obtained using the CMY pixels (i.e. with the GeTe layer fixed in the crystalline state) could be used to very good effect. This is illustrated in **Figure 7.4 (a)** and **(b)** where a simple warning display is generated using combinations of cyan/magenta pixels (Figure 7.4(a)) and cyan/yellow pixels (Figure 7.4(b)); images were generated from simulated and experimental reflectance spectra (i.e. the spectra shown in Figure 7.1(c)-(d) and Figure 7.2(d)-(f)) (Note, Figure 7.4(a)(left) uses FEM calculated spectra to render the picture and Figure 7.4(a)(right) uses experimentally measured spectra to render the figure; the same applies to Figure 7.4(b)). The advantage of using the phase-change metal-insulator-metal approach for such fixed displays is that the colour is essentially structurally generated and so, unlike colorant-based displays, is not subject to any fading with age or extended exposure to sunlight. Moreover, the stronger the ambient illumination, the stronger the resulting image contrast, unlike the case for many conventional electronic displays.

Of course, since the GeTe layer can be switched between phases, by for example using electrical or thermal excitation [23,182], this approach is not limited to the generation of fixed displays. By way of an example in **Figure 7.4(c)-(e)** the same image as that of Figure 7.4(a) and Figure 7.4(b) but in this case rendered into a single pixel type (cyan, magenta and yellow) and with the warning triangle displayed using the GeTe layer in its amorphous state and the background and exclamation mark by the GeTe in the crystalline state. For each pixel type in Figure 7.4(c)-(e) the images were generated using the simulated spectra from Figure 7.1 (left column), the experimental spectra from the fabricated devices (middle column) and actual experimental images written using a scanning laser to switch the phase of the GeTe layer in the pixel devices (right column).

While switching of phase-change metamaterial type structures using ex-situ laser excitation is possible (and also successfully demonstrated by other authors [57,60,61,147]), an in-situ approach (such as the electrical or thermal switching described in Chapter 6) obviously provides a more practicable approach for real-world applications.

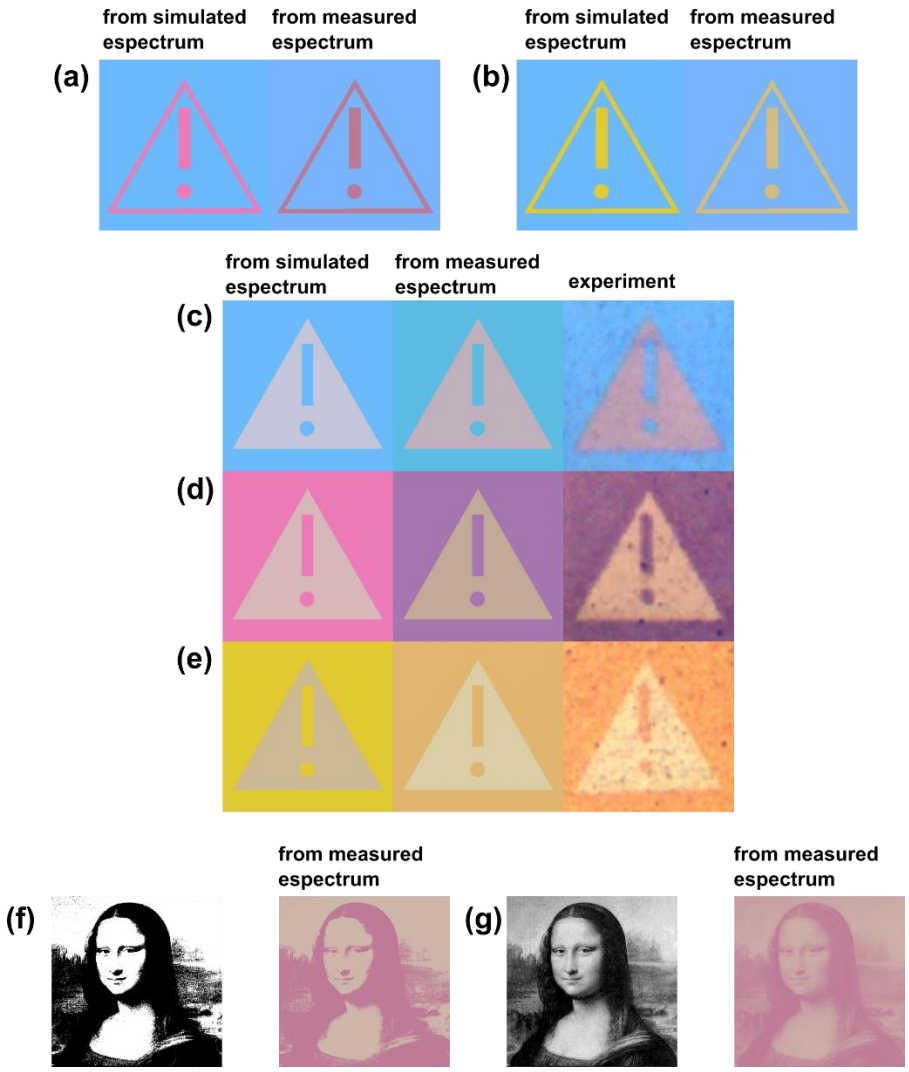

Figure 7.4. Phase-change metal-insulator-metal image generation. **(a)**, **(b)** Images produced by a fixed arrangement of two differently coloured phase-change metal-insulator-metal pixels with the GeTe layer in the crystalline phase; **(a)** uses cyan and magenta pixels, **(b)** cyan and yellow pixels. Shown in each case are (left) images produced using spectral data from FEM simulations and (right) images generated using experimental spectral data. **(c)**, **(d)**, **(e)** Images in CMY pixels and with the warning triangle being produced by GeTe in its amorphous phase and the background and exclamation mark by crystalline GeTe. In each of **(c)**, **(d)** and **(e)** the image generated using simulated spectra (left), experimental spectra (middle) and the image experimentally written in the pixel (right), for the C, M and Y cases respectively are shown (the side of the triangle is 15 μm long). **(f)** Shows a binary (black and white) image of the Mona Lisa (left), rendered (simulated using experimentally measured spectral data of Figure 7.2(e)) in into a binary image using magenta pixels (right) with the GeTe layer in both crystalline (for the black regions) and amorphous (for the white) phases. **(g)** Shows an 8-level gray-scale version of the Mona Lisa (left), rendered (simulated using experimentally measured data of Figure 7.2(e)) to an 8-level image in magenta pixels (right), using fractional crystallization of the GeTe layer.

For the purposes of demonstration, however, ex-situ laser excitation was used here to write the experimental images into the cyan, magenta and yellow pixels, shown in Figure 7.4(c)-(e) (right column). Specifically the crystalline regions in the images were written using a scanning laser with a wavelength of 405 nm, a spot size of approximately 0.5 μm and a power between approximately 9 and 14 mW. Each pulse in the train of pulses had 200 ns duration, 10 μs period, with 2000 pulses used per μm of linear scan. The distance between adjacent lines is 0.5 um. It can be seen that, in general, the agreement between simulated and experimentally obtained colour is quite good, and that the experimentally written images are bright and vivid in colour.

Next, some of the potentialities for a phase-change metal-insulator-metal type pixels for the display of more complex image information are demonstrated. Thus, in **Figure 7.4(f)** a binary (black and white) image of the Mona Lisa is shown, rendered into a binary image in a phase-change metal-insulator-metal display, here using magenta pixels with the GeTe layer in either crystalline or amorphous states. In **Figure 7.4(g)** an 8-level grey-scale version of the Mona Lisa is shown, rendered into an 8-level image in the phase-change metal-insulator-metal display, again in this case using magenta pixels. Both phase-change display images, Figure 7.4(f) and Figure 7.4(g), have been simulated using experimentally measured spectral data of Figure 7.2(e). Note that the 8-levels of contrast are here attained by assuming the GeTe layer can be switched into 8 different fractionally-crystallized states; since chalcogenide phase-change memories have been shown capable of being switched to multiple levels [165,183], such an assumption is reasonable. Such a grey-scale display could find utility in emerging applications such as wearable electronics, where there is a need to display basic information in a cheap and simple way and under a wide variety of ambient light conditions. However, it should be noted that, as demonstrated via the colour map of Figure 7.2(g), the phase-change metal-insulator-metal displays are not limited to simple binary or grey-scale colour generation. Indeed, pixels could be combined in various arrangements to form new palettes richer in colour.

Confirmation that regions shown in the images of Figure 7.4(c)-(e) were indeed amorphous (for the triangle) and crystalline (for the background and exclamation mark) was obtained using Raman analysis. **Figure 7.5(a)** shows a map of the intensity of the 82 cm^{-1} Raman spectral peak for the warning type image writing into the magenta type pixel sample, as shown in Figure 7.4(d) (and repeated here in **Figure 7.5(b)**). The intensity of

the 82 cm^{-1} peak is expected to be significantly higher for crystalline GeTe as compared to amorphous GeTe [184–187], and indeed this is what is observed. In Figure 7.5(a), it is possible to see a clear distinction between amorphous (dark) and crystalline (bright) GeTe regions (note that the red colour here is just false colour mapping of the Raman peak intensity to position) (See the Appendix section for more detailed information regarding the Raman measurements of Figure 7.5).

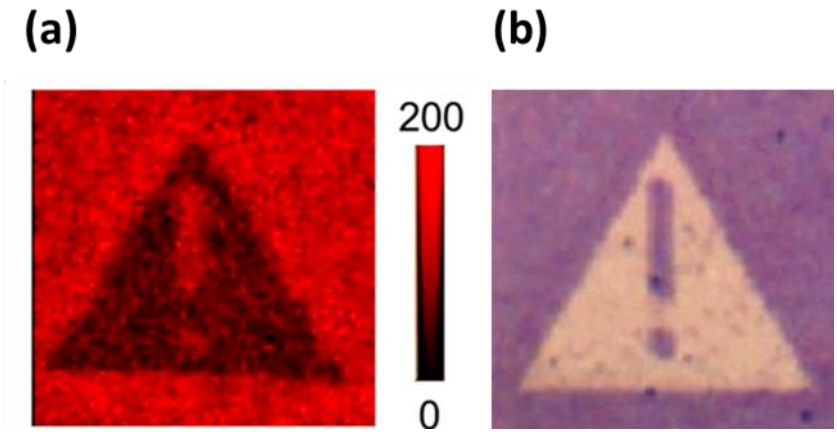

Figure 7.5. (a) Map of the intensity of the 82 cm^{-1} Raman peak for the warning triangle image written into the magenta pixel sample (shown in b), showing that the background and exclamation mark in the image are both crystalline, while the triangle itself is amorphous.

Finally, it should be pointed out that the phase-change metal-insulator-metal absorber structures of the form developed in this work may also find applications in other interesting fields. In particular, if the operation of the devices is considered not from the reflection point of view, but instead from the absorption point of view, then, as pointed out in the previous sections, the devices have the ability to modulate light absorption in the red, green and blue spectral bands. This type of behaviour is intimately related to human visual perception, specifically with the cone cells located in the retina and responsible for colour perception. Thus, it may well be that devices of the type presented here can offer new and interesting possibilities in biologically-inspired artificial vision systems or visual prostheses [188,189].

7.4. Thermal considerations

Although the previous sections have shown good colour production using a phase-change metal-insulator-metal absorber type structure in which aluminium is used for the top and bottom metal layers, there is, potentially, a drawback of using Al in so much as it has a relatively low melting temperature which is only slightly higher than that of many phase-change materials. Thus, during amorphisation of the phase-change layer, it is possible that the bottom, top, or even both Al layers in structures of the type shown in Figure 7.1 could melt and distort (or even mix with the phase-change layer itself). Thus, it is important to take into account thermal considerations when also selecting the optimum choice of metal layers.

Two aspects of the thermal behaviour have been identified to play a key role in the correct functioning of the phase-change metasurface absorber device, namely the achievement of fast enough cooling rates in the phase-change material layer, and the temperature reached in areas of the device susceptible to be melted. Thermal simulations were therefore run in order to quantify these two aspects of the operation. The simulations were carried out for the case of an embedded bottom microheater, as depicted in **Figure 7.6**. In this case, a volumetric heat source domain condition is applied to the bottom metal plane region in the simulation, emulating in this way the Joule heating produced after an electrical pulse is applied to the heater.

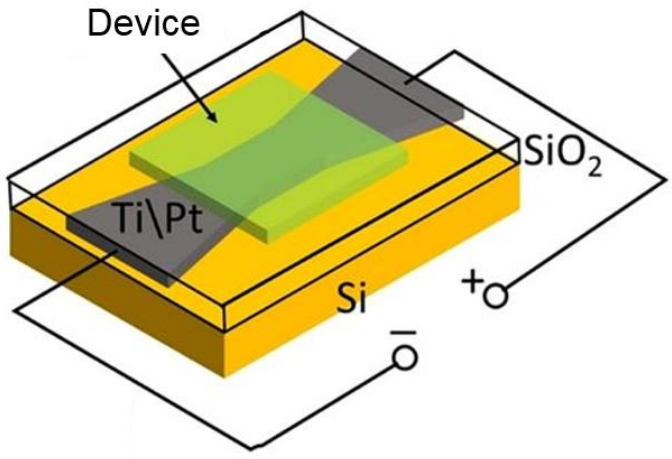

Figure 7.6. Schematic representation of the microheater approach used in the thermal simulations of this section. Figure adapted from ref. [182].

It is possible to do some preliminary considerations regarding the temperature distribution expected. For instance, the temperature reached by the heater (bottom metal plane) has to be greater or equal than the melting point of GeTe in order to be able to melt it. Having into account that the melting point of GeTe (~998 K) is bigger than the melting point of Al (~933 K), that means the bottom metal plane would be melted during the switching process. A solution to this situation would be the employment of a different metal with a higher melting point as bottom metal heater to avoid melting. However, doing so could raise a question on how the replacement of the material in the bottom metal layer would influence the optical response of the device. In order to answer this question, electromagnetic simulations were carried out and it was found that substituting Al by Pt in the bottom metal layer does not carry with it any significant variation in the achieved optical performance. This is due to the low interaction of the resonant mode with the bottom metal plane, in turn due to the high extinction coefficient of GeTe in the visible part of the spectrum (especially in the crystalline phase). **Figure 7.7** shows the optical performance of the CMY pixels using Al compared to Pt as bottom metal plane.

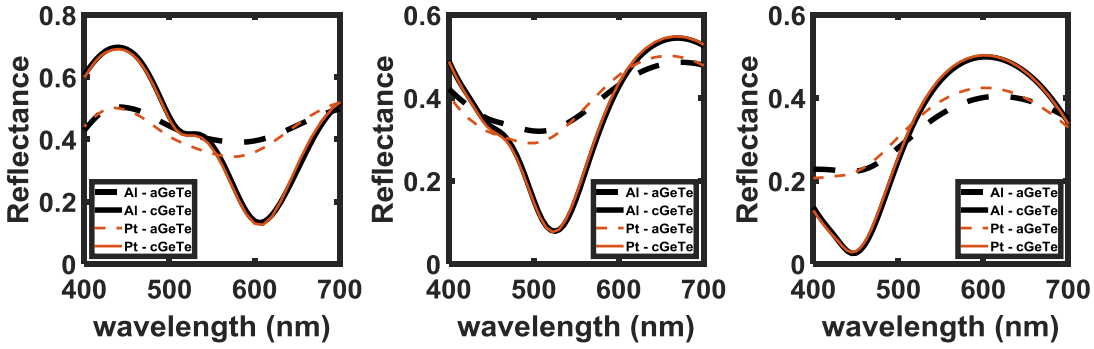

Figure 7.7. Calculated reflectance of the device for the GeTe layer in the amorphous and crystalline state and for devices incorporating aluminium and platinum as bottom metal plane. Optical constants used for Pt are extracted from ref. [137].

Now that an appropriate material to form the bottom metal heater has been identified, the thermal simulations are carried out using this computational domain as a heat source. The temperature in four different points of the structure is monitored in order to assess the correct thermal performance of the designed devices. These four points are the centre of

the Al top disk, the GeTe/ITO interface, the centre of the GeTe layer and the Pt/GeTe interface. The temperature in the top Al top disk indicates if melting point of Al is reached during switching (specifically during re-amorphisation of the GeTe), whereas the temperatures referred to the centre of the GeTe layer and its interfaces indicate if the GeTe layer is completely melted and if the necessary cooling rates are achieved after a re-amorphisation pulse is sent. The temperature curves obtained are plotted in **Figure 7.8**, **Figure 7.9** and **Figure 7.10**. For each individual case, it is possible to see how sufficiently high cooling rates are obtained that enable the successful re-amorphisation of the phase-change layer. As well as this, the materials that comprise the structure are all below their melting temperature during the re-amorphisation pulse, with the exception of GeTe.

One factor in the structure that avoids overheating of the top part of the devices is the low thermal conductivity of the layer in between GeTe and the aluminium top resonator. This layer is composed of ITO in this case, however it can be changed to any other optically transparent material with suitable thermal conductivity when using an embedded microheater approach (Figure 7.6) to enable a correct thermal performance.

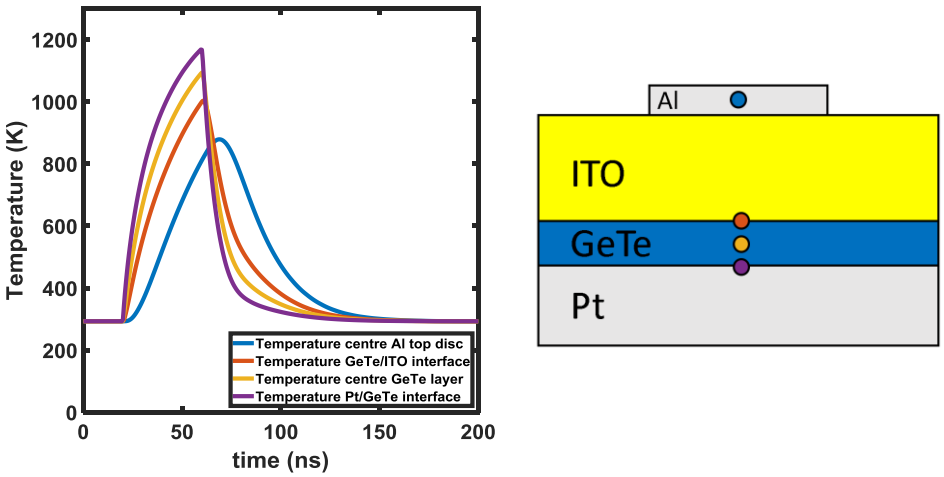

Figure 7.8. (Left) Temperature evolution in the cyan pixel. The temperature plotted corresponds to the centre of the Al top disc, the centre of the GeTe layer, the GeTe/ITO interface and the Pt/GeTe interface for a rectangular pulse of 40 ns duration. The bottom Pt plane was set as a heat source of 0.95e18 Wm^{-3}. The maximum temperature reached in the centre of the top Al resonator is 878 K and the maximum temperature reached in the GeTe/ITO interface is 1003 K. The minimum cooling rate in the GeTe layer is 34 Kns^{-1}. (Right) Schematic showing the points in which the temperature was probed (colour of the circles that mark the position correspond to the colour of the lines in the temperature plot).

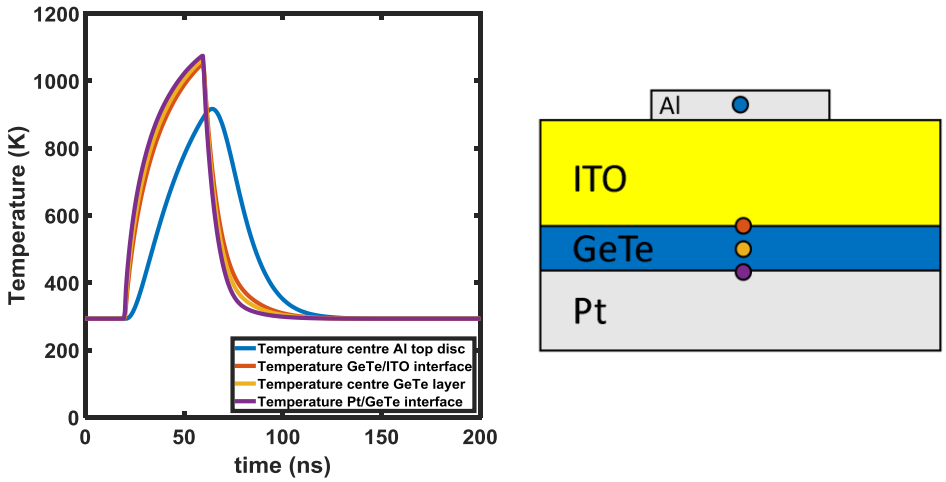

Figure 7.9. (Left) Temperature evolution in the magenta pixel. The temperature plotted corresponds to the centre of the Al top disc, the centre of the GeTe layer, the GeTe/ITO interface and the Pt/GeTe interface for a rectangular pulse of 40 ns duration. The bottom Pt plane was set as a heat source of 0.85e18 Wm^{-3}. The maximum temperature reached in the centre of the top Al resonator is 917 K and the maximum temperature reached in the GeTe/ITO interface is 1052 K. The minimum cooling rate in the GeTe layer is 45 Kns^{-1}. (Right) Schematic showing the points in which the temperature was probed (colour of the circles that mark the position correspond to the colour of the lines in the temperature plot).

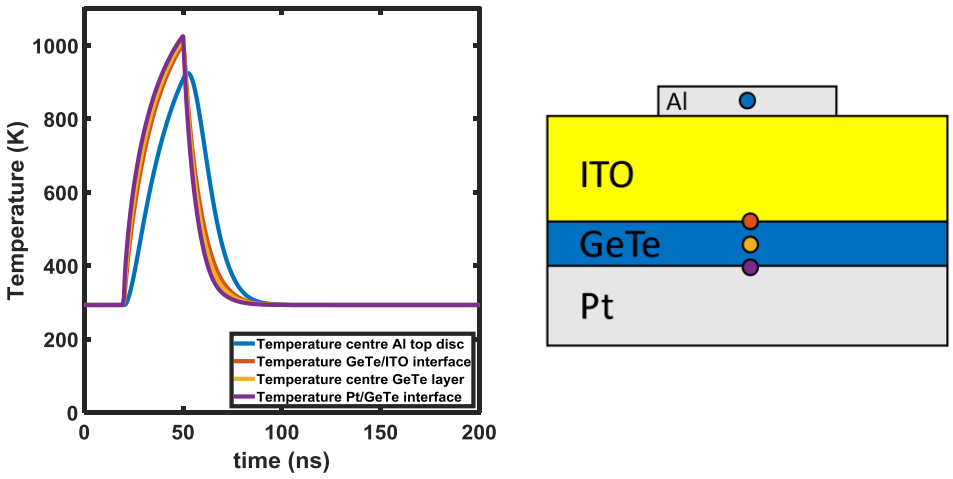

Figure 7.10. (Left) Temperature evolution in the yellow pixel. The temperature plotted corresponds to the centre of the Al top disc, the centre of the GeTe layer, the GeTe/ITO interface and the Pt/GeTe interface for a rectangular pulse of 30 ns duration. The bottom Pt plane was set as a heat source of 0.825e18 Wm^{-3}. The maximum temperature reached in the centre of the top Al resonator is 925 K and the maximum temperature reached in the GeTe/ITO interface is 1004 K. The minimum cooling rate in the GeTe layer is 42 Kns^{-1}. (Right) Schematic showing the points in which the temperature was probed (colour of the circles that mark the position correspond to the colour of the lines in the temperature plot).

In particular, an ultra-low thermal conductivity ITO from [190] has been chosen, although other low thermal conductivity dielectrics could have been chosen as well [191,192]. Thermal properties of GeTe (density, heat capacity and thermal conductivity) for the simulations has been extracted from [193–195].

The structure could be further optimised by considering strategies to enhance robustness in the performance such as encapsulation of the top Al resonator or the use of lower melting point phase-change materials such as AIST, see section 6.4.2.

7.5. Summary

In this chapter, the use of metamaterial absorbers combined with phase-change materials for display applications has been explored. By paying attention to the optical constants displayed by phase-change materials in the visible part of the electromagnetic spectrum and use of metasurface concepts, it was possible to design a structure that generates colours by subtraction (absorbed bands).

The structures were optimised using colorimetric calculations in order to achieve the desired performance in terms of colour production. Individual pixels were then fabricated and their performances measured, finding all expected features of the designed behaviour in the devices' experimental response.

The potential of the fabricated devices in terms of formation of images was assessed by rendering images experimentally using a scanning diode laser, and by means of colorimetric simulations. The designed functionalities allow the formation of high contrast binary images and colour palettes by combination of pixels. All produced results provide a useful insight in the potential performance that these devices would have in applications such as non-volatile display technology and others such as signage or security marking.

Chapter 8 Conclusion and Further Work

8.1. Conclusions

This thesis has presented a detailed study of ways in which phase-change materials can be combined with plasmonic optical metasurfaces to deliver dynamic reconfigurability, and hence additional/new functionality. A particular focus of the work was on metal-insulator-metal absorber type structures and devices, with potential applications ranging from 'perfect' absorbers, amplitude modulators and metasurface-based colour displays. An emphasis throughout has been on the design and development of practicable structures and devices, i.e. ones that (i) can be readily fabricated using conventional manufacturing techniques, (ii) could, eventually, be used in real-world applications and (iii) are amenable to some form of in-situ switching (of the phase-change material embedded in the metasurface). Such an emphasis on practicability has a knock-on effect on the design process, for example in regard to the choice of materials and the geometry of device structures so as to allow for the achievement of the desired optical response, to enable proper environmental protection (since the phase-change layer oxidises easily) and, at the same time, to ensure the necessary thermal and electrical properties for proper switching (crystallisation and, more importantly amorphisation) of the phase-change layer integrated into the metasurface.

In terms of material considerations, a good choice for the suitable encapsulation of the phase-change material was found to be ITO. This brings environmental protection from oxidation while at the same time provides good optical performance (not so strong absorption at the near-infrared wavelength ranges explored in this thesis) and offers the possibility to be used as a top electrode (or at least a conductive layer) for some form of in-situ electrical or thermal (via microheaters) switching of the phase-change layer.

With regards to the materials that are placed in the dielectric spacer, it was found that the materials that comprise this part of the device can be dielectrics or semiconductors (that have a low extinction coefficient at the working frequency). As well as this, these dielectrics should have appropriate thermal conductivity in order to facilitate the correct

thermal operation of the devices (in particular the fast cooling rates, typically > 10 Kns^{-1}, required for successful amorphisation of the phase-change layer).

Turning to the choice of the top and bottom metal layers in the metal-insulator-metal absorber structure, while gold and silver are very commonly used 'plasmonic' metals, they are not necessarily the most suitable for their use in phase-change based metasurfaces, primarily due to their high diffusivity in chalcogenides which can lead to unwanted alloying (e.g. with Au to form $AuTe_2$) and subsequent disruption of the phase-change process [196]. In the work of this thesis, therefore, alternative metals were explored including Al, W, TiN and Pt. A particular interesting result was that there exists a relatively high degree of freedom in the choice for the top metal layer while still having a good optical performance. The bottom metal layer should, however, always exhibit good plasmonic behaviour. A further consideration in the choice of metals for practicable devices is their melting point, which, ideally, should be noticeably higher than that of the phase-change material, so as to avoid unwanted melting of metal layers during amorphisation of the phase-change layer.

In relation to the fabrication process, it was found that the typical tolerances that appear using standard fabrication techniques, such as thin-film deposition by sputtering or evaporation and nanoscale patterning by electron beam or optical lithography, did not have in principle a detrimental impact on the optical performance of the basic metal-insulator-metal absorber device. This is a result that permeates from Chapter 4 to all other chapters in the thesis, since the structures studied in all chapters are essentially similar in nature.

Having successfully addressed the materials and geometric design requirements for the implementation of practicable metal-insulator-metal absorbers, in Chapter 5 a method was developed that allowed for the design, in a fast and efficient way, of the essential aspects of absorber performance, specifically the bandwidth (Q factor) and the resonance frequency. Interestingly, it was found that by fixing two main design parameters of the absorber structure, namely the phase-change layer thickness and width/size of the plasmonic resonators on the top surface, it is possible to control the quality factor and coupling coefficient of the device by changing only the resonator periodicity whilst leaving the operating resonance frequency unaltered. This approach to 'quality factor

engineering' might find useful application wherever precise control over the resonant frequency and quality factor of plasmonic metasurface resonant absorbers type structures is desired.

Turning now attention to the operation of the metal-insulator-metal type absorber devices in a reversible manner, the study in Chapter 6 showed that electrically-driven in-situ switching of the phase-change layer (between its crystalline and amorphous states) is indeed possible using microheaters appropriately embedded into the structure. Indeed, it was shown that, for appropriately patterned plasmonic resonators in the top metal layer (such as the strip-like pattern), it should be possible to employ the resonators as the microheaters themselves.

Finally, in Chapter 7 the basic metal-insulator-metal absorber type structure was adapted for use in the visible, in particular with a view to the generation of reflective colour displays. More specifically, by using the well-known chalcogenide alloy GeTe and an appropriately designed metal-insulator-metal structure it was shown possible to design 'pixels' that, when the GeTe layer is in the crystalline phase, selectively absorb the red, green and blue parts of the spectrum, so generating cyan, magenta and yellow colours. When the GeTe layer is switched to the amorphous phase however, the resonant absorption was suppressed and a white-like reflective response was generated. This functionality can serve to form palettes of different colours, or high contrast images very useful in a variety of display applications such as wearables or signage.

8.2. Further Work

It is interesting to highlight four potentially rewarding routes for further technological development of the concepts put forward in this thesis. Two of them are related to the improvement of the performance and robustness of the reconfigurable phase-change metal-insulator-metal absorber type devices. The other two are related to the improvement of the devices that work in the visible part of the electromagnetic spectrum.

As it has been pointed out, the performance in terms of switchability and energy efficiency is expected to be improved by the employment of the crossbar-like, direct electrical switching structure outlined in Section **6.4.1**. However, in this thesis only

preliminary modelling results have been obtained. Having an experimental demonstration of the correct operation of this structure is something that would have a high value due to its novelty and its potentially superior performance (e.g. in terms of switching speeds and energies). As well as this, a detailed study of alternative (to GST and GeTe) phase-change materials is an area that could potentially be of great benefit, paying particular attention to not only optical properties (n and k), but also to the ease of amorphisation (e.g. via reduced glass transition temperature) and melting temperatures, which also play a key role in determining the effectiveness of electrically-driven in-situ switching capabilities and switching energy.

Another aspect of interest to be further explored is the multilevel operation of the designed devices and the improvement of the performance upon switching. Having a multilevel operation implies that the designed devices would be potentially able to carry out more complex tasks (such as multilevel non-volatile amplitude modulation of light) in both the near-infrared and the visible part of the electromagnetic spectrum.

Furthermore, as it has been said, there is room for improvement on the operation of the display type devices working in the visible part of the electromagnetic spectrum. The first task that would undoubtedly improve the value of the present work is to apply all the results related to electrical switching (the ones mentioned in Chapter 6 and the potential ones referred to the application of different phase-change alloys mentioned in the previous paragraph) to the display type structures.

Finally, turning our attention to the fabrication process for the structures in the visible part of the electromagnetic spectrum, it would be interesting to find a method that replaces the electron beam lithography used here with another kind of fabrication process better suited for relatively large surfaces. It has been seen that the size of the individual features that comprises the pattern for the operation in the visible part of the electromagnetic structure is between 300 nm and 100 nm in diameter. In this situation, it may be worth to explore the deposition of metal nanoparticles. The development of a process that can reliably deposit metal nanoparticles of the right size over large areas would make unnecessary the lithography step with the subsequent improvement of the fabrication process. All this provided that the electromagnetic and thermal behaviour are not substantially affected.

Appendix

A.Colorimetry and photometry concepts

Colorimetry and photometry are very wide and transversal fields. They incorporate knowledge from mathematics, biology, metrology, electronic engineering and computer science. In this section of the appendix the concepts that have been used to calculate the different quantities in Chapter 7 are going to be listed and explained in more detail:

Irradiance and Illuminance: Irradiance is the power per unit area impinging in a surface. Illuminance, on the other hand, is defined according to human perception. Illumination makes reference to the power per unit area but weighted with a function that measures the responsivity of the human vision to light. Illuminance can therefore be considered as a measurement of the perceived amount of light per unit area.

Tristimulus values and chromaticity coordinates: If red, green and blue reference stimuli are used to match all colours perceived in the different wavelengths in the visible part of the spectrum, it will be found that the amount of the different stimulus necessary to match each colour will produce three different wavelength dependent functions called matching functions ($\bar{r}(\lambda)$, $\bar{g}(\lambda)$, $\bar{b}(\lambda)$). If we consider that the generated matching functions forms a basis in algebraic sense to generate all perceived colours, then the tristimulus values will be the scalar product of the colour stimulus studied with each one of the matching functions. The matching functions ($\bar{r}(\lambda)$, $\bar{g}(\lambda)$, $\bar{b}(\lambda)$) are transformed to a more mathematical convenient representation ($\bar{x}(\lambda)$, $\bar{y}(\lambda)$, $\bar{z}(\lambda)$) that does not contain negative values. From this conversion it is possible to define the scalar products previously mentioned that will produce the XYZ tristimulus in the reflective case as it is shown in section 7.2.2.

It is always convenient to start from a conversion of the spectral power distribution under study to the CIE 1931 representation and then convert to another representation from there if necessary. This is because all matrix transformations are usually defined from CIE 1931 to another colour space (sRGB for instance).

B.Parameters for Sputtering Deposition

Material	Chapter	Ar Pressure	Power (W)	RF/DC	Machine
Al	4, 5, 7	1×10^{-3} Torr	170	DC	PB
ITO	4, 5	1×10^{-3} Torr	25	DC	PB
GST	4, 5	1×10^{-3} Torr	25	DC	PB
Al	6, 7	10.5×10^{-3} mbar	170	DC	NPVD
Si	6	5×10^{-3} mbar	55	RF	NPVD
Si_3N_4	6	5×10^{-3} mbar	57	RF	NPVD
GST	6	18.8×10^{-3} mbar	35	DC	NPVD
GST	6	5×10^{-3} mbar	14	RF	NPVD
Ti	6	6.4×10^{-3} Torr	35	DC	N
Pt	6	6.4×10^{-3} Torr	50	DC	N
SiO_2	6	5×10^{-3} mbar	71	RF	NPVD
ITO	7	5×10^{-3} mbar	38	RF	NPVD
GeTe	7	10.5×10^{-3} mbar	15	DC	NPVD

PB: Purpose built sputtering machine; NPVD: Moorfield NanoPVD system; N: Nordiko 2000.

C. Raman measurements in Section 7.3.2

Raman measurements were acquired in a backscattering configuration using a Horiba confocal Raman microscope equipped with an air-cooled charge coupled device (CCD) detector. The GeTe samples were excited with linearly polarized solid-state laser of 532 nm wavelength via a 100× objective. In order to avoid unintentional laser-induced modification to the GeTe lattice structure, all Raman spectra were acquired at a low laser power density of ~ 0.02 mW/μm^2, with the acquisition time set at 30 s, providing optimum signal-to-noise ratio. Raman mapping images (18 μm ×18 μm) were acquired using a motorized xyz stage with a step size of 300 nm and an acquisition time of 2 s at each point. The Si Raman peak at 520.7 cm^{-1} from a control sample was used as reference for the GeTe peak frequency calibration.

Figure A1(a) shows the Raman mapping image of a structurally modified region of the magenta sample, exhibiting clear distinction between amorphous (dark regions) and crystalline (bright regions) GeTe. **Figure A1(b)** shows the corresponding single point Raman spectra taken from the marked regions (see inset of Figure A1). It is evident from the data, crystalline GeTe exhibits significantly higher peak intensity, as well as relatively narrow spectrum (i.e. full-width at half maximum) in comparison to the amorphous phase.

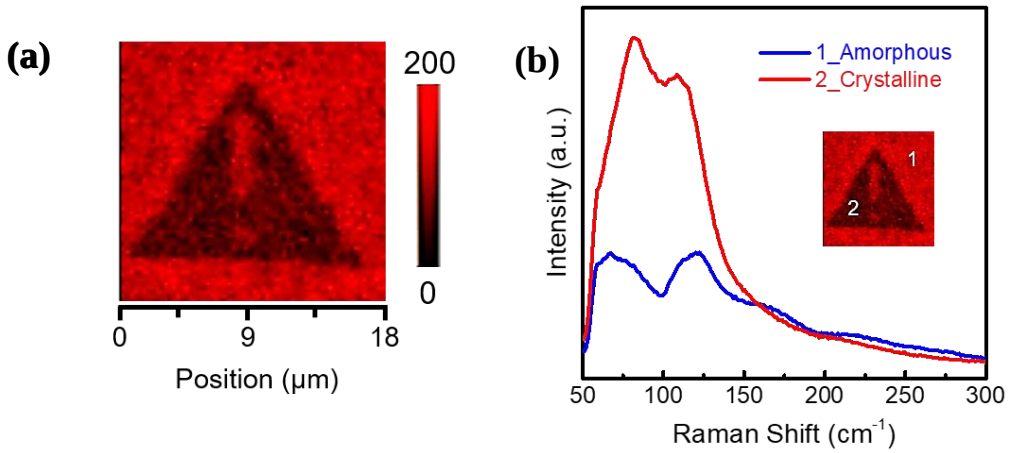

Figure A1. **(a)** Raman mapping of structurally modified GeTe region on Magenta sample. **(b)** Raman spectra of amorphous and crystalline GeTe taken from the marked regions of the Raman map (inset).

References

1. Y. Liu and X. Zhang, "Metamaterials: a new frontier of science and technology," Chem. Soc. Rev. **40**(5), 2494 (2011).

2. S. Raoux and M. Wuttig, *Phase Change Materials: Science and Applications* (Springer, 2009).

3. M. Wuttig and N. Yamada, "Phase-change materials for rewriteable data storage," Nat. Mater. **6**(11), 824–832 (2007).

4. S. R. Ovshinsky, "Reversible Electrical Switching Phenomena in Disordered Structures," Phys. Rev. Lett. **21**(20), 1450–1453 (1968).

5. J. F. Dewald, W. R. Northover, and A. D. Pearson, "Multiple resistance semiconductor elements," (1966).

6. R. Shanks and C. Davis, "A 1024-bit nonvolatile 15ns bipolar read-write memory," in *1978 IEEE International Solid-State Circuits Conference. Digest of Technical Papers* (IEEE, 1978), pp. 112–113.

7. "Special issue in amorphous semiconductors," IEEE Trans. Electron Devices **20**(2), (1973).

8. S. Raoux, F. Xiong, M. Wuttig, and E. Pop, "Phase change materials and phase change memory," MRS Bull. **39**(08), 703–710 (2014).

9. G. E. Moore, "Cramming more components onto integrated circuits," Electronics **38**(8), (1965).

10. T. Storey, K. K. Hunt, M. Graziano, Bin Li, A. Bumgarner, J. Rodgers, and L. Burcin, "Characterization of the 4Mb chalcogenide-random access memory," in *Symposium Non-Volatile Memory Technology 2005.* (IEEE, n.d.), pp. 97–104.

11. M. Chen, K. A. Rubin, and R. W. Barton, "Compound materials for reversible, phase-change optical data storage," Appl. Phys. Lett. **49**(9), 502–504 (1986).

12. N. Yamada, M. Takao, and M. Takenaga, "Te-Ge-Sn-Au Phase Change Recording Film For Optical Disk," in R. P. Freese, A. A. Jamberdino, and M. R. de Haan, eds. (1987), p. 79.

13. N. Yamada, E. Ohno, K. Nishiuchi, N. Akahira, and M. Takao, "Rapid-phase transitions of GeTe-Sb_2Te_3 pseudobinary amorphous thin films for an optical disk memory," J. Appl. Phys. **69**(5), 2849–2856 (1991).

14. H. Iwasaki, Y. Ide, M. Harigaya, Y. Kageyama, and I. Fujimura, "Completely Erasable Phase Change Optical Disk," Jpn. J. Appl. Phys. **31**(Part 1, No. 2B), 461–465 (1992).

15. F. T. Hady, A. Foong, B. Veal, and D. Williams, "Platform Storage Performance With 3D XPoint Technology," Proc. IEEE **105**(9), 1822–1833 (2017).

16. M. Stanisavljevic, H. Pozidis, A. Athmanathan, N. Papandreou, T. Mittelholzer, and E. Eleftheriou, "Demonstration of Reliable Triple-Level-Cell (TLC) Phase-Change Memory," in *2016 IEEE 8th International Memory Workshop (IMW)* (IEEE, 2016), pp. 1–4.

17. T. Tuma, A. Pantazi, M. Le Gallo, A. Sebastian, and E. Eleftheriou, "Stochastic phase-change neurons," Nat. Nanotechnol. **11**(8), 693–699 (2016).

18. D. Kuzum, R. G. D. Jeyasingh, B. Lee, and H. P. Wong, "Nanoelectronic Programable Synapses Based on Phase-Change Materials for Brain-Inspired Computing," Nano Lett. **12**, 2179–2186 (2012).

19. C. Ríos, M. Stegmaier, P. Hosseini, D. Wang, T. Scherer, C. D. Wright, H. Bhaskaran, and W. H. P. Pernice, "Integrated all-photonic non-volatile multi-level memory," Nat. Photonics **9**(11), 725–732 (2015).

20. M. Stegmaier, C. Ríos, H. Bhaskaran, and W. H. P. Pernice, "Thermo-optical Effect in Phase-Change Nanophotonics," ACS Photonics **3**(5), 828–835 (2016).

21. Z. Cheng, C. Ríos, N. Youngblood, C. D. Wright, W. H. P. Pernice, and H. Bhaskaran, "Device-Level Photonic Memories and Logic Applications Using Phase-Change Materials," Adv. Mater. 1802435 (2018).

22. Z. Cheng, C. Ríos, W. H. P. Pernice, C. D. Wright, and H. Bhaskaran, "On-chip photonic synapse," Sci. Adv. **3**(9), e1700160 (2017).

23. P. Hosseini, C. D. Wright, and H. Bhaskaran, "An optoelectronic framework enabled by low-dimensional phase-change films," Nature **511**(7508), 206–211

(2014).

24. C. Ríos, P. Hosseini, R. A. Taylor, and H. Bhaskaran, "Color Depth Modulation and Resolution in Phase-Change Material Nanodisplays," Adv. Mater. **28**(23), 4720–4726 (2016).

25. B. Broughton, L. Bandhu, C. Talagrand, S. Garcia-Castillo, M. Yang, H. Bhaskaran, and P. Hosseini, "Solid-State Reflective Displays (SRD ®) Utilizing Ultrathin Phase-Change Materials," SID Symp. Dig. Tech. Pap. **48**(1), 546–549 (2017).

26. S. Tretyakov, A. Urbas, and N. Zheludev, "The century of metamaterials," J. Opt. **19**(8), 080404 (2017).

27. T. Koschny, C. M. Soukoulis, and M. Wegener, "Metamaterials in microwaves, optics, mechanics, thermodynamics, and transport," J. Opt. **19**(8), 084005 (2017).

28. "http://congress2017.metamorphose-vi.org/," .

29. "http://metamorphose-vi.org/index.php/metamaterials," .

30. N. Yu, P. Genevet, M. A. Kats, F. Aieta, J.-P. Tetienne, F. Capasso, and Z. Gaburro, "Light propagation with phase discontinuities: generalized laws of reflection and refraction," Science **334**(6054), 333–337 (2011).

31. J. B. Pendry, "Negative Refraction Makes a Perfect Lens," Phys. Rev. Lett. **85**(18), 3966–3969 (2000).

32. K. Yao and Y. Liu, "Plasmonic metamaterials," Nanotechnol. Rev. **3**(2), 177 (2014).

33. G. Eleftheriades and M. Selvanayagam, "Transforming Electromagnetics Using Metamaterials," IEEE Microw. Mag. **13**(2), 26–38 (2012).

34. J. C. Bose, "On the Rotation of Plane of Polarisation of Electric Waves by a Twisted Structure," Proc. R. Soc. London **63**(1), 146–152 (1898).

35. H. Lamb, "On the Reflection and Transmission of Electric Waves by a Metallic Grating," Proc. London Math. Soc. **s1-29**(1), 523–546 (1897).

36. S. A. Tretyakov, "A personal view on the origins and developments of the

metamaterial concept," J. Opt. **19**(1), 013002 (2017).

37. V. Veselago, "The electrodynamics of substances with simultaneous negative values of episilon and mu," Sov. Phys. Uspekhi **10**(4), 6 (1968).

38. S. A. Schelkunoff and H. T. Friis, *Antennas: Theory and Practice* (Wiley New York, 1952).

39. D. L. Jaggard and N. Engheta, "Chirosorb^{TM} as an invisible medium," Electron. Lett. **25**(3), 173 (1989).

40. A. Mackay, B. Sanz-Izquierdo, and E. A. Parker, "Evolution of Frequency Selective Surfaces," FERMAT **2**(008), 1–7 (2014).

41. C. L. Holloway, E. F. Kuester, J. a. Gordon, J. O'Hara, J. Booth, and D. R. Smith, "An overview of the theory and applications of metasurfaces: The two-dimensional equivalents of metamaterials," IEEE Antennas Propag. Mag. **54**(2), 10–35 (2012).

42. D. R. Smith, W. J. Padilla, D. C. Vier, S. C. Nemat-Nasser, and S. Schultz, "Composite Medium with Simultaneously Negative Permeability and Permittivity," Phys. Rev. Lett. **84**(18), 4184–4187 (2000).

43. R. A. Shelby, D. R. Smith, and S. Schultz, "Experimental verification of a negative index of refraction.," Science **292**(5514), 77–9 (2001).

44. D. Schurig, J. J. Mock, B. J. Justice, S. A. Cummer, J. B. Pendry, A. F. Starr, and D. R. Smith, "Metamaterial electromagnetic cloak at microwave frequencies.," Science **314**(5801), 977–80 (2006).

45. A. V Kildishev, A. Boltasseva, and V. M. Shalaev, "Planar photonics with metasurfaces.," Science **339**(6125), 1232009 (2013).

46. S. Jahani and Z. Jacob, "All-dielectric metamaterials," Nat. Nanotechnol. **11**(1), 23–36 (2016).

47. N. I. Zheludev and Y. S. Kivshar, "From metamaterials to metadevices," Nat. Mater. **11**(11), 917–924 (2012).

48. J. P. Turpin, J. a. Bossard, K. L. Morgan, D. H. Werner, and P. L. Werner, "Reconfigurable and Tunable Metamaterials: A Review of the Theory and

Applications," Int. J. Antennas Propag. **2014**, 1–18 (2014).

49. Y. H. Fu, A. Q. Liu, W. M. Zhu, X. M. Zhang, D. P. Tsai, J. B. Zhang, T. Mei, J. F. Tao, H. C. Guo, X. H. Zhang, J. H. Teng, N. I. Zheludev, G. Q. Lo, and D. L. Kwong, "A Micromachined Reconfigurable Metamaterial via Reconfiguration of Asymmetric Split-Ring Resonators," Adv. Funct. Mater. **21**(18), 3589–3594 (2011).

50. J.-Y. Ou, E. Plum, and N. I. Zheludev, "MHz bandwidth electro-optical modulator based on a reconfigurable photonic metamaterial," in *CLEO: Applications and Technology* (2012), p. JW4A--11.

51. I. M. Pryce, K. Aydin, Y. A. Kelaita, R. M. Briggs, and H. A. Atwater, "Highly Strained Compliant Optical Metamaterials with Large Frequency Tunability," Nano Lett. **10**(10), 4222–4227 (2010).

52. H. Tao, A. C. Strikwerda, K. Fan, W. J. Padilla, X. Zhang, and R. D. Averitt, "Reconfigurable Terahertz Metamaterials," Phys. Rev. Lett. **103**(14), 147401 (2009).

53. F. Yi, E. Shim, A. Y. Zhu, H. Zhu, J. C. Reed, and E. Cubukcu, "Voltage tuning of plasmonic absorbers by indium tin oxide," Appl. Phys. Lett. **102**(22), 221102 (2013).

54. S. H. Lee, M. Choi, T.-T. Kim, S. Lee, M. Liu, X. Yin, H. K. Choi, S. S. Lee, C.-G. Choi, S.-Y. Choi, X. Zhang, and B. Min, "Switching terahertz waves with gate-controlled active graphene metamaterials," Nat. Mater. **11**(11), 936–941 (2012).

55. D. Shrekenhamer, W.-C. Chen, and W. J. Padilla, "Liquid Crystal Tunable Metamaterial Absorber," Phys. Rev. Lett. **110**(17), 177403 (2013).

56. Z. Zhu, P. G. Evans, R. F. Haglund Jr, and J. G. Valentine, "Dynamically reconfigurable metadevice employing nanostructured phase-change materials," Nano Lett. **17**(8), 4881–4885 (2017).

57. B. Gholipour, J. Zhang, K. F. MacDonald, D. W. Hewak, and N. I. Zheludev, "An all-optical, non-volatile, bidirectional, phase-change meta-switch," Adv. Mater. **25**(22), 3050–4 (2013).

58. A. Tittl, A.-K. U. Michel, M. Schäferling, X. Yin, B. Gholipour, L. Cui, M. Wuttig, T. Taubner, F. Neubrech, and H. Giessen, "A switchable mid-infrared plasmonic perfect absorber with multispectral thermal imaging capability," Adv. Mater. **27**(31), 4579–4603 (2015).

59. S. G.-C. Carrillo, G. R. Nash, H. Hayat, M. J. Cryan, M. Klemm, H. Bhaskaran, and C. D. Wright, "Design of practicable phase-change metadevices for near-infrared absorber and modulator applications," Opt. Express **24**(12), 13563 (2016).

60. C. de Galarreta, A. M. Alexeev, A. Yat-Yin, M. Lopez-Garcia, M. Klemm, M. Cryan, J. Bertolotti, and C. D. Wright, "Non-Volatile Reconfigurable Phase-change Metadevices for Beam Steering in the Near-Infrared," Adv. Funct. Mater. **28**(10), 1704993 (2018).

61. Q. Wang, E. T. F. Rogers, B. Gholipour, C.-M. Wang, G. Yuan, J. Teng, and N. I. Zheludev, "Optically reconfigurable metasurfaces and photonic devices based on phase change materials," Nat. Photonics **10**(1), 60–65 (2016).

62. T. Cao, L. Zhang, R. E. Simpson, and M. J. Cryan, "Mid-infrared tunable polarization-independent perfect absorber using a phase-change metamaterial," J. Opt. Soc. Am. B **30**(6), 1580 (2013).

63. I. S. Kim, S. L. Cho, D. H. Im, E. H. Cho, D. H. Kim, G. H. Oh, D. H. Ahn, S. O. Park, S. W. Nam, J. T. Moon, and others, "High performance PRAM cell scalable to sub-20nm technology with below 4F2 cell size, extendable to DRAM applications," in *2010 Symposium on VLSI Technology* (2010), pp. 203–204.

64. S. Senkader and C. D. Wright, "Models for phase-change of $Ge_2Sb_2Te_5$ in optical and electrical memory devices," J. Appl. Phys. **95**(2), 504–511 (2004).

65. S. Raoux, W. Wełnic, and D. Ielmini, "Phase Change Materials and Their Application to Nonvolatile Memories," Chem. Rev. **110**(1), 240–267 (2010).

66. B. H-S Philip Wong, F. Ieee, S. Raoux, S. Member IEEE, S. Kim, J. Liang, S. Member IEEE, J. P. Reifenberg, B. Rajendran, M. Ieee, M. Asheghi, and K. E. Goodson, "Phase Change Memory," Proc. IEEE **98**(12), 2201–2227 (2010).

67. J. a. Kalb, M. Wuttig, and F. Spaepen, "Calorimetric measurements of structural

relaxation and glass transition temperatures in sputtered films of amorphous Te alloys used for phase change recording," J. Mater. Res. **22**(03), 748–754 (2007).

68. P. G. Debenedetti and F. H. Stillinger, "Supercooled liquids and the glass transition," Nature **410**, 259 (2001).

69. C. Peng, L. Cheng, and M. Mansuripur, "Experimental and theoretical investigations of laser-induced crystallization and amorphization in phase-change optical recording media," J. Appl. Phys. **82**(9), 4183 (1998).

70. T. P. L. Pedersen, J. Kalb, W. K. Njoroge, D. Wamwangi, M. Wuttig, and F. Spaepen, "Mechanical stresses upon crystallization in phase change materials," Appl. Phys. Lett. **79**(22), 3597–3599 (2001).

71. S.-Y. Kim, S. J. Kim, H. Seo, and M. R. Kim, "Variation of the complex refractive indices with Sb-addition in Ge-Sb-Te alloy and their wavelength dependence," in S. R. Kubota, T. D. Milster, and P. J. Wehrenberg, eds. (International Society for Optics and Photonics, 1998), **3401**, pp. 112–115.

72. K. Shportko, S. Kremers, M. Woda, D. Lencer, J. Robertson, and M. Wuttig, "Resonant bonding in crystalline phase-change materials," Nat. Mater. **7**(8), 653–658 (2008).

73. B. Gholipour, A. Karvounis, J. Yin, C. Soci, K. F. MacDonald, and N. I. Zheludev, "Phase-change-driven dielectric-plasmonic transitions in chalcogenide metasurfaces," NPG Asia Mater. **10**(6), 533–539 (2018).

74. B.-S. Lee, J. R. Abelson, S. G. Bishop, D.-H. Kang, B. Cheong, and K.-B. Kim, "Investigation of the optical and electronic properties of $Ge_2Sb_2Te_5$ phase change material in its amorphous, cubic, and hexagonal phases," J. Appl. Phys. **97**(9), 093509 (2005).

75. A. Redaelli, A. Pirovano, F. Pellizzer, A. L. Lacaita, D. Ielmini, and R. Bez, "Electronic Switching Effect and Phase-Change Transition in Chalcogenide Materials," IEEE Electron Device Lett. **25**(10), 684–686 (2004).

76. S. Raoux, F. Xiong, M. Wuttig, and E. Pop, "Phase change materials and phase change memory," MRS Bull. **39**(08), 703–710 (2014).

77. A. Sebastian, M. Le Gallo, and D. Krebs, "Crystal growth within a phase change memory cell," Nat. Commun. **5**(1), 4314 (2014).

78. L. E. Shelimova, O. G. Karpinskii, P. P. Konstantinov, M. A. Kretova, E. S. Avilov, and V. S. Zemskov, "Composition and Properties of Layered Compounds in the GeTe–Sb_2Te_3 System," Inorg. Mater. **37**(4), 342–348 (2001).

79. I. Friedrich, V. Weidenhof, W. Njoroge, P. Franz, and M. Wuttig, "Structural transformations of $Ge_2Sb_2Te_5$ films studied by electrical resistance measurements," J. Appl. Phys. **87**(9), 4130 (2000).

80. S. Yamanaka, S. Ogawa, I. Morimoto, and Y. Ueshima, "Electronic Structures and Optical Properties of GeTe and $Ge_2Sb_2Te_5$," Jpn. J. Appl. Phys. **37**(Part 1, No. 6A), 3327–3333 (1998).

81. P. Hosseini, C. D. Wright, and H. Bhaskaran, "An optoelectronic framework enabled by low-dimensional phase-change films," Nature **511**(7508), 206–211 (2014).

82. S. A. Maier, *Plasmonics: Fundamentals and Applications* (Spriger, 2007).

83. J. Hao, L. Zhou, and M. Qiu, "Nearly total absorption of light and heat generation by plasmonic metamaterials," Phys. Rev. B **83**(16), 165107 (2011).

84. Y. Cui, Y. He, Y. Jin, F. Ding, L. Yang, Y. Ye, S. Zhong, Y. Lin, and S. He, "Plasmonic and metamaterial structures as electromagnetic absorbers," Laser Photon. Rev. **8**(4), 495–520 (2014).

85. W. L. Barnes, A. Dereux, and T. W. Ebbesen, "Surface plamons subwavelength optics," Nature **424**(August), 824–830 (2003).

86. S. Ogawa and M. Kimata, "Metal-Insulator-Metal-Based Plasmonic Metamaterial Absorbers at Visible and Infrared Wavelengths: A Review," Materials (Basel). **11**(3), 458 (2018).

87. N. I. Landy, S. Sajuyigbe, J. J. Mock, D. R. Smith, and W. J. Padilla, "Perfect metamaterial absorber," Phys. Rev. Lett. **100**(20), 207402 (2008).

88. P. Zhu and L. Jay Guo, "High performance broadband absorber in the visible band

by engineered dispersion and geometry of a metal-dielectric-metal stack," Appl. Phys. Lett. **101**(24), 241116 (2012).

89. H. Tao, C. M. Bingham, A. C. Strikwerda, D. Pilon, D. Shrekenhamer, N. I. Landy, K. Fan, X. Zhang, W. J. Padilla, and R. D. Averitt, "Highly flexible wide angle of incidence terahertz metamaterial absorber: Design, fabrication, and characterization," Phys. Rev. B **78**(24), 241103 (2008).

90. C. Wu, B. Neuner, G. Shvets, J. John, A. Milder, B. Zollars, and S. Savoy, "Large-area wide-angle spectrally selective plasmonic absorber," Phys. Rev. B **84**(7), 075102 (2011).

91. X. Liu, T. Starr, A. F. Starr, and W. J. Padilla, "Infrared Spatial and Frequency Selective Metamaterial with Near-Unity Absorbance," Phys. Rev. Lett. **104**(20), 207403 (2010).

92. J. Hao, J. Wang, X. Liu, W. J. Padilla, L. Zhou, and M. Qiu, "High performance optical absorber based on a plasmonic metamaterial," Appl. Phys. Lett. **96**(25), 251104 (2010).

93. H. H. Solak, C. Dais, and F. Clube, "Displacement Talbot lithography: a new method for high-resolution patterning of large areas," Opt. Express **19**(11), 10686 (2011).

94. X. Shen, Y. Yang, Y. Zang, J. Gu, J. Han, W. Zhang, and T. Jun Cui, "Triple-band terahertz metamaterial absorber: Design, experiment, and physical interpretation," Appl. Phys. Lett. **101**(15), 154102 (2012).

95. T. Cao, L. Zhang, R. E. Simpson, and M. J. Cryan, "Mid-infrared tunable polarization-independent perfect absorber using a phase-change metamaterial," J. Opt. Soc. Am. B **30**(6), 1580 (2013).

96. T. Cao, C. Wei, R. E. Simpson, L. Zhang, and M. J. Cryan, "Rapid phase transition of a phase-change metamaterial perfect absorber," Opt. Mater. Express **3**(8), 1101 (2013).

97. A. Tittl, M. G. Harats, R. Walter, X. Yin, M. Schäferling, N. Liu, R. Rapaport, and H. Giessen, "Quantitative Angle-Resolved Small-Spot Reflectance Measurements

on Plasmonic Perfect Absorbers: Impedance Matching and Disorder Effects," ACS Nano **8**(10), 10885–10892 (2014).

98. R. Alaee, M. Albooyeh, S. Tretyakov, and C. Rockstuhl, "Phase-change material-based nanoantennas with tunable radiation patterns," Opt. Lett. **41**(17), 4099 (2016).

99. C. Qu, S. Ma, J. Hao, M. Qiu, X. Li, S. Xiao, Z. Miao, N. Dai, Q. He, S. Sun, and others, "Tailor the functionalities of metasurfaces based on a complete phase diagram," Phys. Rev. Lett. **115**(23), 235503 (2015).

100. S. D. Rezaei, J. Ho, R. J. H. Ng, S. Ramakrishna, and J. K. W. Yang, "On the correlation of absorption cross-section with plasmonic color generation," Opt. Express **25**(22), 27652–27664 (2017).

101. X. Yin, M. Schäferling, A.-K. U. Michel, A. Tittl, M. Wuttig, T. Taubner, and H. Giessen, "Active Chiral Plasmonics," Nano Lett. **15**(7), 4255–4260 (2015).

102. S. García-Cuevas Carrillo, G. R. Nash, H. Hayat, M. J. Cryan, M. Klemm, H. Bhaskaran, and C. David Wright, "Design of practicable phase-change metadevices for near-infrared absorber and modulator applications," Opt. Express **24**(12), 13563–13573 (2016).

103. T. Cao, C. Wei, R. E. Simpson, L. Zhang, and M. J. Cryan, "Rapid phase transition of a phase-change metamaterial perfect absorber," Opt. Mater. Express **3**(8), 1101 (2013).

104. A. K. U. Michel, D. N. Chigrin, T. W. W. Maß, K. Schönauer, M. Salinga, M. Wuttig, and T. Taubner, "Using low-loss phase-change materials for mid-infrared antenna resonance tuning," Nano Lett. **13**(8), 3470–3475 (2013).

105. W. Dong, Y. Qiu, J. Yang, R. E. Simpson, and T. Cao, "Wideband Absorbers in the Visible with Ultrathin Plasmonic-Phase Change Material Nanogratings," J. Phys. Chem. C **120**(23), 12713–12722 (2016).

106. T. Cao, C. Wei, R. E. Simpson, L. Zhang, and M. J. Cryan, "Broadband polarization-independent perfect absorber using a phase-change metamaterial at visible frequencies.," Sci. Rep. **4**, 3955 (2014).

107. A. R. Parker, "515 Million Years of Structural Colour," J. Opt. A Pure Appl. Opt. **2**(6), R15–R28 (2000).

108. Y.-K. R. Wu, A. E. Hollowell, C. Zhang, and L. J. Guo, "Angle-insensitive structural colours based on metallic nanocavities and coloured pixels beyond the diffraction limit," Sci. Rep. **3**, 1194 (2013).

109. F. Cheng, J. Gao, T. S. Luk, and X. Yang, "Structural color printing based on plasmonic metasurfaces of perfect light absorption," Sci. Rep. **5**, 11045 (2015).

110. Y. Yu, L. Wen, S. Song, and Q. Chen, "Transmissive/Reflective Structural Color Filters: Theory and Applications," J. Nanomater. **2014**(8), 1–17 (2014).

111. K. Kumar, H. Duan, R. S. Hegde, S. C. W. Koh, J. N. Wei, and J. K. W. Yang, "Printing colour at the optical diffraction limit," Nat. Nanotechnol. **7**(9), 557–561 (2012).

112. G. Si, Y. Zhao, J. Lv, M. Lu, F. Wang, H. Liu, N. Xiang, T. J. Huang, A. J. Danner, J. Teng, and Y. J. Liu, "Reflective plasmonic color filters based on lithographically patterned silver nanorod arrays.," Nanoscale **5**(14), 6243–8 (2013).

113. T. Xu, Y.-K. Wu, X. Luo, and L. J. Guo, "Plasmonic nanoresonators for high-resolution colour filtering and spectral imaging," Nat. Commun. **1**(5), 1–5 (2010).

114. A. S. Roberts, A. Pors, O. Albrektsen, and S. I. Bozhevolnyi, "Subwavelength plasmonic color printing protected for ambient use," Nano Lett. **14**(2), 783–787 (2014).

115. J. K. W. Tan, S. J., Zhang, L., Zhu, D., Goh, X. M., Qiu, C-W., Yang, "Wide-range Plasmonic Palette for Photorealistic Color Printing with Aluminum Nanostructures," Nano Lett. **14**(7), 4023–4029 (2014).

116. S. Yoo, T. Gwon, T. Eom, S. Kim, and C. S. Hwang, "Multicolor Changeable Optical Coating by Adopting Multiple Layers of Ultrathin Phase Change Material Film," ACS Photonics **3**(7), 1265–1270 (2016).

117. COMSOL Multiphysics documentation, "RF Module User's Guide," Version 5.3a (2018).

118. COMSOL Multiphysics documentation, "Heat Transfer Module User's Guide," Version 5.3a (2018).

119. COMSOL Multiphysics documentation, "AC/DC Module User's Guide," Version 5.3a (2018).

120. C. D. Wright, M. Armand, and M. M. Aziz, "Terabit-per-square-inch data storage using phase-change media and scanning electrical nanoprobes," IEEE Trans. Nanotechnol. **5**(1), 50–61 (2006).

121. C. D. Wright, K. Blyuss, and P. Ashwin, "Master-equation approach to understanding multistate phase-change memories and processors," Appl. Phys. Lett. **90**(2007), 1–3 (2007).

122. A. Aladool, M. M. Aziz, and C. D. Wright, "Understanding the importance of the temperature dependence of viscosity on the crystallization dynamics in the $Ge_2Sb_2Te_5$ phase-change material," J. Appl. Phys. **121**(22), 224504 (2017).

123. P. Ashwin, B. S. V. Patnaik, and C. D. Wright, "Fast simulation of phase-change processes in chalcogenide alloys using a Gillespie-type cellular automata approach," J. Appl. Phys. **104**(8), 084901 (2008).

124. C. D. Wright, Y. Liu, K. I. Kohary, M. M. Aziz, and R. J. Hicken, "Arithmetic and Biologically-Inspired Computing Using Phase-Change Materials," Adv. Mater. **23**(30), 3408–3413 (2011).

125. S. C. Chapra, *Applied Numerical Methods with MATLAB for Engineers and Scientists*, Fourth Edi (McGraw-Hill Education, 2018).

126. J. Vazquez, P. Ashwin, K. I. Kohary, and C. D. Wright, "Phase-change RAM modelling and design via a Gillespie-type cellular automata approach," in *2010 17th IEEE International Conference on Electronics, Circuits and Systems* (IEEE, 2010), pp. 1013–1016.

127. URL:https://uk.mathworks.com/help/gads/direct-search.html, "MathWorks®. Global Optimisation Toolbox Documentation (2017)," (2017).

128. J. A. Thornton, "Influence of apparatus geometry and deposition conditions on the structure and topography of thick sputtered coatings," J. Vac. Sci. Technol. **11**(4),

666–670 (1974).

129. P. Pokorný, J. Musil, P. Fitl, M. Novotný, J. Lančok, and J. Bulíř, "Contamination of Magnetron Sputtered Metallic Films by Oxygen From Residual Atmosphere in Deposition Chamber," Plasma Process. Polym. **12**(5), 416–421 (2015).

130. Y. Chen, "Nanofabrication by electron beam lithography and its applications: A review," Microelectron. Eng. **135**, 57–72 (2015).

131. L. Reimer, *Image Formation in Low Voltage Scanning Electron Microscopy* (SPIE Optical Engineering Press, 1993).

132. Y. G. Chen, T. S. Kao, B. Ng, X. Li, X. G. Luo, B. Luk'yanchuk, S. A. Maier, and M. H. Hong, "Hybrid phase-change plasmonic crystals for active tuning of lattice resonances," Opt. Express **21**(11), 13691–8 (2013).

133. A. Karvounis, B. Gholipour, K. F. MacDonald, and N. I. Zheludev, "All-dielectric phase-change reconfigurable metasurface," Appl. Phys. Lett. **109**(5), 051103 (2016).

134. E. Gourvest, B. Pelissier, C. Vallée, A. Roule, S. Lhostis, and S. Maitrejean, "Impact of Oxidation on $Ge_2Sb_2Te_5$ and GeTe Phase-Change Properties," J. Electrochem. Soc. **159**(4), H373–H377 (2012).

135. G. W. Burr, M. J. Breitwisch, M. Franceschini, D. Garetto, K. Gopalakrishnan, B. Jackson, B. Kurdi, C. Lam, L. A. Lastras, A. Padilla, B. Rajendran, S. Raoux, and R. S. Shenoy, "Phase change memory technology," J. Vac. Sci. Technol. B Microelectron. Nanom. Struct. **28**(2), 223–262 (2010).

136. P. B. Johnson and R. W. Christy, "Optical Constants of the Noble Metals," Phys. Rev. B **6**(12), 4370–4379 (1972).

137. A. D. Rakic, A. B. Djurišic, J. M. Elazar, and M. L. Majewski, "Optical Properties of Metallic Films for Vertical-Cavity Optoelectronic Devices," Appl. Opt. **37**(22), 5271 (1998).

138. G. V. Naik, J. Kim, and A. Boltasseva, "Oxides and nitrides as alternative plasmonic materials in the optical range [Invited]," Opt. Mater. Express **1**(6), 1090 (2011).

139. F. Lai, L. Lin, R. Gai, Y. Lin, and Z. Huang, "Determination of optical constants and thicknesses of In_2O_3:Sn films from transmittance data," Thin Solid Films **515**, 7387–7392 (2007).

140. L. Lin, F. Lai, Y. Qu, R. Gai, and Z. Huang, "Influence of annealing in N_2 on the properties of In2O3:Sn thin films prepared by direct current magnetron sputtering," Mater. Sci. Eng. B Solid-State Mater. Adv. Technol. **138**, 166–171 (2007).

141. K. Shportko, S. Kremers, M. Woda, D. Lencer, J. Robertson, and M. Wuttig, "Resonant bonding in crystalline phase-change materials.," Nat. Mater. **7**(8), 653–8 (2008).

142. T. G. Kolda, R. M. Lewis, and V. Torczon, "Optimization by Direct Search: New Perspectives on Some Classical and Modern Methods," Soc. Ind. Appl. Math. **45**(3), 385–482 (2003).

143. L. Y. Mario, S. Darmawan, and M. K. Chin, "Asymmetric Fano resonance and bistability for high extinction ratio, large modulation depth, and low power switching.," Opt. Express **14**(26), 12770–12781 (2006).

144. G. T. Reed, G. Mashanovich, F. Y. Gardes, and D. J. Thomson, "Silicon optical modulators," Nat. Photonics **4**(8), 518–526 (2010).

145. C. D. Wright, P. Hosseini, and J. a V. Diosdado, "Beyond von-neumann computing with nanoscale phase-change memory devices," Adv. Funct. Mater. **23**(18), 2248–2254 (2013).

146. J. A. Vázquez Diosdado, P. Ashwin, K. I. Kohary, and C. D. Wright, "Threshold switching via electric field induced crystallization in phase-change memory devices," Appl. Phys. Lett. **100**(25), 253105 (2012).

147. A.-K. U. Michel, P. Zalden, D. N. Chigrin, M. Wuttig, A. M. Lindenberg, and T. Taubner, "Reversible Optical Switching of Infrared Antenna Resonances with Ultrathin Phase-Change Layers Using Femtosecond Laser Pulses," ACS Photonics **1**(9), 833–839 (2014).

148. P. Li, X. Yang, T. W. W. Maß, J. Hanss, M. Lewin, A.-K. U. Michel, M. Wuttig, and T. Taubner, "Reversible optical switching of highly confined phonon–

polaritons with an ultrathin phase-change material," Nat. Mater. **15**(8), 870–875 (2016).

149. T. Maier and H. Brueckl, "Multispectral microbolometers for the midinfrared," Opt. Lett. **35**(22), 3766–3768 (2010).

150. F. B. P. Niesler, J. K. Gansel, S. Fischbach, and M. Wegener, "Metamaterial metal-based bolometers," Appl. Phys. Lett. **100**(20), 203508 (2012).

151. C. Wu, B. Neuner III, J. John, A. Milder, B. Zollars, S. Savoy, and G. Shvets, "Metamaterial-based integrated plasmonic absorber/emitter for solar thermo-photovoltaic systems," J. Opt. **14**(2), 024005 (2012).

152. S. Ogawa and M. Kimata, "Wavelength-or Polarization-Selective Thermal Infrared Detectors for Multi-Color or Polarimetric Imaging Using Plasmonics and Metamaterials," Materials (Basel). **10**(5), 493 (2017).

153. K. Fan, J. Y. Suen, and W. J. Padilla, "Graphene metamaterial spatial light modulator for infrared single pixel imaging," Opt. Express **25**(21), 25318–25325 (2017).

154. T. G. Mayerhofer, R. Knipper, U. Hübner, D. Cialla-May, K. Weber, H.-G. Meyer, and J. Popp, "Ultra sensing by combining extraordinary optical transmission with perfect absorption," ACS Photonics **2**(11), 1567–1575 (2015).

155. K. Chen, R. Adato, and H. Altug, "Dual-band perfect absorber for multispectral plasmon-enhanced infrared spectroscopy," ACS Nano **6**(9), 7998–8006 (2012).

156. C. Huck, J. Vogt, M. Sendner, D. Hengstler, F. Neubrech, and A. Pucci, "Plasmonic enhancement of infrared vibrational signals: nanoslits versus nanorods," ACS Photonics **2**(10), 1489–1497 (2015).

157. T. G. Mayerhöfer and J. Popp, "Periodic array-based substrates for surface-enhanced infrared spectroscopy," Nanophotonics **7**(1), 39–79 (2018).

158. H. a Haus, "Waves and Fields in Optoelectronics," (1984).

159. A. Pors and S. I. Bozhevolnyi, "Plasmonic metasurfaces for efficient phase control in reflection," Opt. Express **21**(22), 27438 (2013).

160. T. Søndergaard, J. Jung, S. I. Bozhevolnyi, and G. Della Valle, "Theoretical analysis of gold nano-strip gap plasmon resonators," New J. Phys. **10**(10), 105008 (2008).

161. Q. Bai, M. Perrin, C. Sauvan, J.-P. Hugonin, and P. Lalanne, "Efficient and intuitive method for the analysis of light scattering by a resonant nanostructure," Opt. Express **21**(22), 27371–27382 (2013).

162. P. Lalanne, W. Yan, K. Vynck, C. Sauvan, and J.-P. Hugonin, "Light Interaction with Photonic and Plasmonic Resonances," Laser Photon. Rev. **12**(5), 1700113 (2018).

163. Y.-C. Chung, P.-J. Cheng, Y.-H. Chou, B.-T. Chou, K.-B. Hong, J.-H. Shih, S.-D. Lin, T.-C. Lu, and T.-R. Lin, "Surface roughness effects on aluminium-based ultraviolet plasmonic nanolasers," Sci. Rep. **7**, 39813 (2017).

164. N. Liu, M. Mesch, T. Weiss, M. Hentschel, and H. Giessen, "Infrared perfect absorber and its application as plasmonic sensor.," Nano Lett. **10**(7), 2342–8 (2010).

165. G. W. Burr, M. J. BrightSky, A. Sebastian, H.-Y. Cheng, J.-Y. Wu, S. Kim, N. E. Sosa, N. Papandreou, H.-L. Lung, H. Pozidis, E. Eleftheriou, and C. H. Lam, "Recent Progress in Phase-Change Memory Technology," IEEE J. Emerg. Sel. Top. Circuits Syst. **6**(2), 146–162 (2016).

166. A. Mennai, A. Bessaudou, F. Cosset, C. Guines, P. Blondy, and A. Crunteanu, "Bistable RF switches using $Ge_2Sb_2Te_5$ phase change material," in *2015 European Microwave Conference (EuMC)* (IEEE, 2015), pp. 945–947.

167. Y. Shim, G. Hummel, and M. Rais-Zadeh, "RF switches using phase change materials," in *2013 IEEE 26th International Conference on Micro Electro Mechanical Systems (MEMS)* (IEEE, 2013), pp. 237–240.

168. Sasago Y. et al., "Cross-point phase change memory with 4F2 cell size driven by low-contact-resistivity poly-Si diode," in *Symposium on VLSI Technology* (I E E E, 2009).

169. C. Rios, M. Stegmaier, Z. Cheng, N. Youngblood, C. D. Wright, W. H. P. Pernice,

and H. Bhaskaran, "Controlled switching of phase-change materials by evanescent-field coupling in integrated photonics [Invited]," Opt. Mater. Express **8**(9), 2455 (2018).

170. J. Orava, D. W. Hewak, and A. L. Greer, "Fragile-to-Strong Crossover in Supercooled Liquid Ag-In-Sb-Te Studied by Ultrafast Calorimetry," Adv. Funct. Mater. **25**(30), 4851–4858 (2015).

171. D. Lencer, M. Salinga, and M. Wuttig, "Design rules for phase-change materials in data storage applications," Adv. Mater. **23**(18), 2030–2058 (2011).

172. S. Guerin, B. Hayden, D. W. Hewak, and C. Vian, "Synthesis and Screening of Phase Change Chalcogenide Thin Film Materials for Data Storage," ACS Comb. Sci. **19**(7), 478–491 (2017).

173. J. Kalb, F. Spaepen, and M. Wuttig, "Atomic force microscopy measurements of crystal nucleation and growth rates in thin films of amorphous Te alloys," Appl. Phys. Lett. **84**(25), 5240–5242 (2004).

174. D. Turnbull, "Under what conditions can a glass be formed?," Contemp. Phys. **10**(5), 473–488 (1969).

175. J. Orava and A. L. Greer, "Classical-nucleation-theory analysis of priming in chalcogenide phase-change memory," Acta Mater. **139**, 226–235 (2017).

176. S. Mukherjee, N. Smith, M. Goulding, C. Topping, S. Norman, Q. Liu, L. Kramer, S. Kularatne, and J. Heikenfeld, "A first demonstration and analysis of the biprimary color system for reflective displays," J. Soc. Inf. Disp. **22**(2), 106–114 (2014).

177. J. Heikenfeld, P. Drzaic, J.-S. Yeo, and T. Koch, "Review Paper: A critical review of the present and future prospects for electronic paper," J. Soc. Inf. Disp. **19**(2), 129–156 (2011).

178. International Commission on Illumination, *CIE 15: Technical Report: Colorimetry, 3rd Edition* (2004).

179. H. S. Fairman, M. H. Brill, and H. Hemmendinger, "How the CIE 1931 color-matching functions were derived from Wright-Guild data," Color Res. Appl. **22**(1),

11–23 (1997).

180. "https://www.idealliance.org/specifications," .

181. A. D. Rakić, A. B. Djurišić, J. M. Elazar, and M. L. Majewski, "Optical properties of metallic films for vertical-cavity optoelectronic devices," Appl. Opt. **37**(22), 5271–5283 (1998).

182. Y.-Y. Au, H. Bhaskaran, and C. D. Wright, "Phase-change devices for simultaneous optical-electrical applications," Sci. Rep. **7**(1), 9688 (2017).

183. A. Athmanathan, M. Stanisavljevic, N. Papandreou, H. Pozidis, and E. Eleftheriou, "Multilevel-Cell Phase-Change Memory: A Viable Technology," IEEE J. Emerg. Sel. Top. Circuits Syst. **6**(1), 87–100 (2016).

184. S. J. Park, H. Park, M. H. Jang, M. Ahn, W. J. Yang, J. H. Han, H.-S. Jeong, C.-W. Kim, Y.-K. Kwon, and M.-H. Cho, "Laser irradiation-induced modification of the amorphous phase in GeTe films: the role of intermediate Ge–Te bonding in the crystallization mechanism," J. Mater. Chem. C **3**(36), 9393–9402 (2015).

185. R. De Bastiani, E. Carria, S. Gibilisco, M. G. Grimaldi, A. R. Pennisi, A. Gotti, A. Pirovano, R. Bez, and E. Rimini, "Ion-irradiation-induced selective bond rearrangements in amorphous GeTe thin films," Phys. Rev. B **80**(24), 245205 (2009).

186. M. Upadhyay, S. Murugavel, M. Anbarasu, and T. R. Ravindran, "Structural study on amorphous and crystalline state of phase change material," J. Appl. Phys. **110**(8), 083711 (2011).

187. N. N. Yu, H. Tong, and X. S. Miao, "Structure and phonon behavior of crystalline GeTe ultrathin film," Appl. Phys. Lett. **105**(12), 121902 (2014).

188. G. J. Lee, C. Choi, D.-H. Kim, and Y. M. Song, "Bioinspired Artificial Eyes: Optic Components, Digital Cameras, and Visual Prostheses," Adv. Funct. Mater. 1705202 (2017).

189. A. T. Chuang, C. E. Margo, and P. B. Greenberg, "Retinal implants: a systematic review.," Br. J. Ophthalmol. **98**(7), 852–6 (2014).

190. V. I. Brinzari, A. I. Cocemasov, D. L. Nika, and G. S. Korotcenkov, "Ultra-low thermal conductivity of nanogranular indium tin oxide films deposited by spray pyrolysis," Appl. Phys. Lett. **110**(7), 071904 (2017).

191. M. R. Saleem, S. Honkanen, and J. Turunen, "Thermal properties of TiO_2 films fabricated by atomic layer deposition," IOP Conf. Ser. Mater. Sci. Eng. **60**(1), 012008 (2014).

192. K. E. Goodson, M. I. Flik, L. T. Su, and D. A. Antoniadis, "Annealing-temperature dependence of the thermal conductivity of LPCVD silicon-dioxide layers," IEEE Electron Device Lett. **14**(10), 490–492 (1993).

193. K. S. Andrikopoulos, S. N. Yannopoulos, G. A. Voyiatzis, A. V Kolobov, M. Ribes, and J. Tominaga, "Raman scattering study of the a-GeTe structure and possible mechanism for the amorphous to crystal transition," J. Phys. Condens. Matter **18**(3), 965–979 (2006).

194. C. A. and editors of the volumes III/17E-17F-41C, "Germanium telluride (GeTe) heat capacity, density, melting point," in *Non-Tetrahedrally Bonded Elements and Binary Compounds I* (Springer-Verlag, n.d.), pp. 1–3.

195. P. Zalden, K. S. Siegert, S. Rols, H. E. Fischer, F. Schlich, T. Hu, and M. Wuttig, "Specific Heat of $(GeTe)_x(Sb_2Te_3)_{1-x}$ Phase-Change Materials: The Impact of Disorder and Anharmonicity," Chem. Mater. **26**(7), 2307–2312 (2014).

196. L. Lu, W. Dong, J. K. Behera, L. Chew, and R. E. Simpson, "Inter-diffusion of plasmonic metals and phase change materials," J. Mater. Sci. **54**(4), 2814–2823 (2019).

197. Y. V. Pershin and M. Di Ventra, "Memory effects in complex materials and nanoscale systems," Adv. Phys. **60**(2), 145–227 (2011).

198. P. W. Anderson, "Through the Glass Lightly," Science **267**(5204), (1995).

199. D. M. Pozar, *Microwave Engineering*, Fourth Edi (Wiley, 2011).

200. G. F. Naterer, *Advanced Heat Transfer*, Second Edi (CRC Press, Taylor & Francis Group, 2018).